Interfacial and Nanoscale Science Facility

The Interfacial & Nanoscale Science Facility (INSF) is a world-class resource for scientific expertise and instrumentation focused on the study of interfacial phenomena and nanoscience and technology. This section summarizes the capabilities available in the INSF, along with research programs associated with facility users. Activities in the facility address national needs in environmental restoration, waste management, pollution prevention, energy production and storage, and national and homeland security through research that specializes in preparation, characterization, and reactivity of surfaces and interfaces. The range of scientific expertise and instrumentation within the facility provides a unique environment for research in areas such as nanoscience and nanotechnology; interfacial catalytic chemistry; designed oxide interfaces, including environmental aerosol and mineral interfaces; materials and chemoselective interfaces; and areas within microanalytical science, such as chemical sensing and nanobiotechnology.

The INSF and its scientific staff provide a broad range of instrumentation, laboratory capabilities, and expertise. Instrumentation is available for chemical synthesis, analytical chemistry, separations, electrochemistry, thin-film deposition, catalytic reactors, ion-beam processing, and microfabrication. Capabilities include an accelerator facility for material modification and analysis using ion beams along with interface characterization; scanning probe microscopies; electron microscopy and x-ray analysis; spectroelectrochemistry; high-spatial/energy resolution surface analysis; catalyst preparation, characterization, and reaction engineering; a fully equipped clean room for microfabrication, microanalytical systems development, and testing laboratories; inorganic, organic, polymer, and biochemical synthesis and characterization facilities; a full complement of thin-film deposition and characterization facilities; and fully equipped analytical support laboratories. The combination of surface and interface characterization techniques that provide high spatial, depth, and energy resolution for a broad array of methods is unmatched anywhere in the world. Many systems are coupled directly to film growth chambers, and samples can be moved among 16 different systems under controlled environments without exposure to air.

Instrumentation & Capabilities

- Thin-film deposition
- Surface analysis suite
- Electron microscopy suite
- Scanning probe microscopy
- Ion-beam processing and analysis
- Nanobiotechnology capabilities
- Surface Science and Catalysis Laboratory
- Catalytic reactors
- X-ray diffraction laboratory
- Microfabrication
- Chemical and biological sensing
- Other analytical and characterization laboratories

Staff assigned to the INSF perform innovative research in the areas of surface and interfacial chemistry, advanced materials synthesis and characterization, and microanalytical science. Our activities emphasize research relevant to the four U.S. Department of Energy (DOE) mission areas—science, energy resources, environmental quality, and national security—and to operation of a world-class user facility that supports the DOE science mission. Our staff also plays a major role in the continued success of the W.R. Wiley Environmental Molecular Sciences Laboratory (EMSL) by providing support, training, and collaboration to onsite users. Over the past seven years, research activities in the INSF have focused on four major

thrust areas: 1) films and interphases, 2) surface chemistry and catalysis, 3) material interfaces, and 4) microsensors, microfluidics, and new biotechnologies. Staff assigned to the INSF continue to focus their efforts in these four areas with research on the following topics:

- *Oxide and Mineral Films and Surfaces*. Structural and chemical properties of model single-crystal oxide and complex mineral surfaces.
- *Electronic and Catalytic Materials*. High dielectric materials, magnetic oxide semiconductors, and oxide catalysts.
- *Nanoscale Materials*. Oxide quantum dots and nanofilms of magnetic and oxygen ion-conducting oxides, buried nanoclusters in oxides.
- *Interfacial Properties and Reactivity*. Reactions at oxide and mineral interfaces and the structural and chemical properties.
- *Microanalytical Separations and Sensing*. Development of new microanalytical and sensing principles, tools, and testing.
- *Nanobiotechnology*. Single-enzyme nanoparticles, enzymes in nanostructured matrices; understanding the dynamics of these materials.
- *Environmental Studies*. Waste separations, structural and chemical stability of waste forms under different radiation and chemical environment, atmospheric aerosols.
- *Analysis and Characterization*. Fully equipped analytical laboratories and characterization facilities.

Films and Interphases. The physical and chemical properties of the region between single phases of a material (i.e., the interphase) have a major influence on many characteristics of the material, including stability, electronic properties, atomic and ionic transport, and chemical reactivity. Research programs include the synthesis of thin films and nanostructured materials, both of which contain a high concentration of interphase regions. Research activities also involve studies of solid/solid, solid/liquid, and solid/gas (or vacuum) interphase regions. Although most studies are focused on inorganic materials and interphases, organic and biological systems are becoming an increasingly large part of our work.

Surface Chemistry and Catalysis. Basic research is carried out with the most simple, well-defined, environmentally relevant crystallographic structures (e.g., mineral carbonates, metal oxides) for which molecular theory and spectroscopy are immediately applicable. The work then progresses to materials with more complex structures, such as iron and titanium oxides with substitutional impurities. For example, fundamental studies of the oxygen storage and release properties of pure and zirconium-doped ceria single-crystal thin films are aimed at understanding how these "oxygen storage materials" perform in an automobile exhaust system catalytic converter. In addition to fundamental surface chemistry research, we are developing materials and reactor designs for a number of heterogeneous catalytic processes. One study involves synthesizing, characterizing, and testing a group of novel, mesoporous, silica-supported, solid-acid catalysts for use in petroleum-refining processes.

Material Interfaces. Studies are being conducted in several areas: solid/solid interfaces in a wide variety of materials, radiation effects in materials, fundamental defect properties and interactions, atomic and ionic transport, and aerosol characterization. Many of the studies

on solid/solid interfaces involve 1) characterization of interfaces between thin films and substrates, between ion-beam-modified surfaces and the original substrate, or between nanoclusters and host matrices; 2) segregation or diffusion of point defects, impurities, dopants, or gas atoms to or from such interfaces; 3) transport of hydrogen, oxygen, or other gases across such interfaces; 4) formation or destruction of such interfaces from radiation damage processes; and 5) stability of interfaces under a wide range of environmental conditions. Studies on radiation effects include experimental research on materials for immobilization of nuclear waste and plutonium, as well as materials for next-generation nuclear power production, wide-band-gap semiconductors, and multiscale computer simulations of damage production processes, defect diffusion, and microstructure evolution. Studies on atomic and ionic transport include ion exchange processes in nuclear waste glasses, hydrogen storage and transport in materials, and oxygen transport in fast ion conductors.

Microsensors, Microfluids, and Nanobiotechnology. This research includes four primary thrust areas: 1) array-based vapor sensors, 2) nanoscience, 3) bioanalytical microfluidics, and 4) radioanalytical microfluidics. Key areas of science in array-based vapor-sensing include rational design, development, and synthesis of polymeric-sensing materials, linear free-energy models for vapor/polymer interactions, organic thin films, photo-patterning methods for sensor materials, integrated sensor systems, and multivariate data analyses. The nanoscience area includes development of monolayer-protected gold nanoparticles for use on sorptive sensing films, single-enzyme nanoparticles as a new nanostructure for enzyme stabilization, and multi-functional nanoparticle assemblies for biodetection. The latter two areas represent a new thrust in nanobiotechnology, and a laboratory within EMSL has been established for synthesizing enzyme nanostructures and studying enzyme kinetics and enzymes in nanostructured matrices. Experimental research in bioanalytical microfluidics and radioanalytical microfluidics is now located primarily in other facilities, but close scientific ties with EMSL are maintained.

Capabilities

Thin-Film Deposition. Thin-film deposition capabilities include oxygen plasma-assisted molecular beam epitaxy (MBE) systems (Figure 1), a metal organic chemical vapor deposition system (MOCVD), and a sputter deposition system. The MBE systems consist of growth chambers connected to surface characterization chambers through sample transfer lines. The growth chambers have various electron beam and effusion cell sources along with reflection high-energy electron diffraction and quartz crystal oscillators to monitor the growth. The surface characterization chambers are equipped with several surface-science capabilities including x-ray photoelectron spectroscopy (XPS)/diffraction, Auger electron spectroscopy (AES) low-energy electron diffraction (LEED), and atomic force microscopy/scanning tunneling microscopy (AFM/STM). The MOCVD system is specially designed for epitaxial growth of oxide thin films. The system comprises a rotating disk reactor, two metal organic source

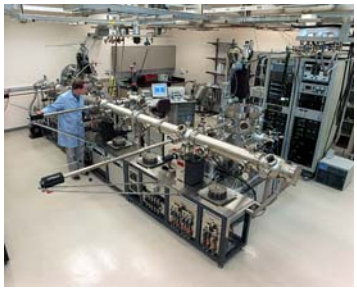

Figure 1. Oxygen plasma-assisted MBE system.

delivery systems (bubbler vapor-phase and direct liquid source-injection), an oxygen microwave plasma unit, a spectroscopic ellipsometer, and a Fourier transform infrared (FTIR) spectrometer. The system is capable of growing uniform (in both thickness and composition) oxide thin films with abrupt interfaces. The sputter deposition system consists of radio frequency and direct current sputtering sources.

Surface Analysis Suite. The surface analysis suite consists of a Physical Electronics Instruments (PHI) Quantum 2000 high-resolution, x-ray photoelectron spectrometer (Figure 2), a Kratos Axis multi-technique surface analysis system (SAS), a PHI Model T2100 time-of-flight secondary ion mass spectrometer (TOF-SIMS), and a PHI Model 680 AES/scanning Auger microprobe. The Quantum 2000 XPS system is unique in that it uses a focused monochromatic Al K α x-ray beam that can be varied in size from as small as 10 μm in diameter to approximately 200 μm. The TOF-SIMS system uses a pulsed and focused ion source and TOF analyzer to obtain high spatial- and mass-resolution data from a specimen surface. The multi-technique SAS enables surfaces to be probed with a variety of complementary analysis methods, and contains electron imaging, electron spectroscopy, and both primary and secondary ion-scattering capabilities. The Model 680 auger electron spectrometer (AES)/scanning Auger microprobe is based on a field-emission electron source and a cylindrical mirror analyzer. The electron beam size can be focused as low as 10 nm at 20 kV, although somewhat larger beams are typically used to collect AES data. Instrument features and capabilities include beam rastering, scanning electron microscope (SEM) imaging, mapping, specimen cleaning and depth profiling using a sputter gun, and sample rotation to allow "Zalar" rotation during sputtering. The system also is configured with an x-ray detector for near-surface analysis in combination with AES surface analysis.

Figure 2. X-ray photoelectron spectrometer.

Electron Microscopy Suite. The electron microscopy suite consists of a LEO 982 field-emission scanning electron microscope (FESEM), a high-resolution transmission electron microscope (TEM) (Figure 3), and another cryo-TEM dedicated for biological work (Cryo TEM). The FESEM is an ultrahigh-performance SEM with a resolution of 1 nm at 30 kV and 4 nm at 1.0 kV. It has a large specimen chamber equipped with multiple detectors, a below-lens secondary electron detector, an in-lens secondary electron detector, a backscatter electron detector, an energy-dispersive x-ray detector, and an electron backscatter diffraction detector. The JEOL 2010 is a high-resolution TEM with a spatial resolution of 0.194 nm. This instrument has a medium acceleration voltage of 200 kV, a high-brightness electron source, digital image recording, a computer-controlled sample goniometer, and a geometrically optimized x-ray detector. It has a wide range of illumination lens conditions: TEM mode, energy-dispersive spectroscopy mode, nanometer beam electron diffraction, and convergent beam electron

Figure 3. High-resolution TEM.

diffraction. The TEM is post-column attached with a Gatan image filter, giving an optimized energy resolution of approximately 1.2 eV, which allows analysis of light elements by electron energy-loss spectroscopy and elemental mapping in the electron spectroscopic imaging. The Cryo TEM is primarily used for biological imaging and tomography. The spatial resolution of the instrument is about 0.45 nm, and it has an accelerator voltage in the range of 80 to 120 kV.

Scanning Probe Microscopy. The scanning probe microscopy laboratory has a Digital Instrument Nanoscope IIIa AFM, a Topometrix TMX 1000 Explorer SPM, and a OmiCron variable non-contact ultrahigh vacuum (UHV) AFM/STM system with surface-science capabilities including XPS, Auger electron microscopy, plasma cleaning, and deposition. The instrument is capable of operating in both air and liquid environments and in several modes that include contact, tapping, frictional force, phase/frequency, capacitance, and magnetic/electrostatic force. As a real space probe, the instrument can be used to probe surface morphology, defects, and electrostatic, magnetic, dopant concentration, and mechanical properties of conducting and non-conducting materials. The Topometrix TMX 1000 Explorer SPM can be used for both AFM and STM in air and in liquid and is particularly useful for larger samples. This instrument includes both contact and non-contact AFM modes. STM requires an electrically conductive sample and produces images based on the topography and electronic structure of the sample. AFM samples may be insulating or conducting; the image is based on the force between the AFM probe and the sample and is primarily a map of the surface topography. The OmiCron variable scanning probe microscope can be used for both STM and AFM under UHV conditions. As a real space probe, this instrument is designed to probe surface structure, defects, and morphology of conducting and non-conducting materials. In addition to STM/AFM, the vacuum system also is equipped with other surface-science capabilities that include LEED, XPS, AES, and oxygen plasma cleaning.

Ion-Beam Processing and Analysis. The accelerator facility (Figure 4) is equipped with capabilities to perform material modification and analysis using high-energy ion beams. The facility has two ion sources, a 3-MeV tandem ion accelerator, injector and analyzing magnets, beam lines, and four end stations. The end station on the +30° beam line is equipped with LEED, AES, XPS, oxygen plasma, and sputter cleaning sources and effusion cells in addition to the conventional ion-beam capabilities. Ion-beam capabilities include fixed and movable detectors for Rutherford backscattering spectrometry/channeling, nuclear reaction analysis (NRA), and elastic recoil detection analysis (ERDA). This beam line extends through the end station to another end station where experiments can be performed with the beam size of 20 microns or greater. The micro-beam end station is also equipped with capabilities for conventional ion-beam techniques including RBS, NRA, and proton-induced x-ray emission (PIXE). The +15° beam line is equipped with a raster scanner for ion implantation and ion-beam modification of materials, and the end station is equipped with all the conventional ion-beam capabilities. The −15° end station is designed to carry out routine analytical work. The NEC RC 43 end station attached to this beam line is

Figure 4. Accelerator facility.

equipped with most of the standard ion-beam analytical capabilities including RBS, NRA, PIXE, particle-induced gamma emission, proton elastic scattering analysis, scanning transmission ion microscopy, and ERDA.

Surface Science and Catalysis Laboratory. Three UHV surface chemistry systems designed for studies of the molecular-level chemistry of adsorbates on metal oxide surfaces are available in the Surface Science and Catalysis Laboratory. These systems are equipped with a number of spectroscopic tools to follow changes in adsorbate chemistry, including high-resolution electron energy-loss spectroscopy, SIMS, ultraviolet photoemission, XPS, AES, and LEED. In addition, both electron-stimulated desorption and temperature-programmed desorption (TPD) studies are routinely performed in some systems. Typical information obtainable in TPD experiments includes the quantity and nature (intact or dissociated molecule) of an adsorbed gas. In addition, estimates of the sticking coefficient and the activation energy for desorption and/or reaction of the adsorbed molecule can be made. One of these systems has a combination of surface-science and high-pressure catalysis capabilities and is capable of measuring gas/solid reaction rates under realistic, high-pressure (approximately 1 atm) conditions using model, low-surface-area solid samples. Reaction rates as a function of temperature and varying reagent partial pressures also can be measured in this system.

Catalytic Reactors. The Reaction Engineering Laboratories are equipped with a variety of analytical capabilities and catalytic reactors including an Advanced Scientific Designs, Inc. RXM-100 catalyst testing and characterization instrument and a Zeton Altamira reactor test stand. The RXM-100, a multi-functional instrument used for catalyst studies, combines UHV and high-pressure capabilities in a single instrument without compromising specifications or ease of use. A number of measurements can be made using this instrument including chemical adsorption, physical adsorption, surface area, pore size, pore distribution, and temperature programmed characterization (desorption, reduction, and oxidation). An online mass spectrometer, gas chromatograph, FTIR, and thermal conductivity detector can be used to analyze effluent gases. The instrument has the capability of running up to 10 different gases simultaneously. In addition, high-pressure reactions (up to 1000 psi) can be run within a few minutes of each other on the same system, with little change in system configuration. This system offers extensive flexibility in catalyst testing and decreases inefficiency and contamination problems that arise from transferring materials between systems and waiting for data from other sources. The Zeton Altamira reactor test stand comprises three types of reactors generally used in bench-scale testing of catalysts: a fixed bed reactor, a Rotoberty reactor, and a continuous stirred tank reactor. This design allows users to evaluate catalyst performance and study chemical reactions in various reactor configurations.

X-Ray Diffraction. The suite of x-ray diffraction (XRD) equipment in EMSL consists of four instruments: a general-purpose XRD system for studying polycrystalline samples under ambient conditions, a special applications XRD system with low- and high-temperature sample stages covering the range of −193°C to +1000°C, and a four-circle XRD system. The general-purpose system is most often used to examine powder samples (x-ray powder diffraction), but it also can be used to study certain types of thin films. In addition to its non-ambient capabilities, the special applications system is equipped to examine thin-film

samples in more detail, including grazing-incidence XRD (GIXRD) and x-ray reflectivity (XRR) measurements. The four-circle system is typically configured for high-resolution x-ray diffraction studies of epitaxial thin films. Additional applications of the four-circle system include stress measurements, texture analysis, GIXRD, and XRR.

Chemically Selective Materials and Sensors. Development and evaluation of sensor materials and chemical microsensors are supported by a wet chemistry laboratory for organic, polymer, and nanomaterial synthesis; a laboratory for evaluation of chemical sensor and sensor materials using automated vapor generation and blending systems; and a clean room with selected microfabrication capabilities. A variety of techniques for applying sensing materials to sensor devices are available, and numerous electronic test instruments are available in the sensing laboratories and the EMSL Instrument Development Laboratory. These capabilities are complemented by a range of surface analysis and characterization instruments as well as conventional analytical instrumentation in EMSL. Users may wish to bring new sensing materials to EMSL for application to sensing devices and evaluation, while others may bring complete sensor systems with data collection capabilities to couple to EMSL automated vapor generation systems. Research areas include sensor arrays, sensor materials design and synthesis, sensing material/analyte interactions, and chemometric methods.

Microfabrication. Microfabrication equipment provides a significant research and development capability in the areas of microstructures, microsensors, and microanalytical systems. Unlike highly automated industrial production equipment, the microfabrication equipment in EMSL has multipurpose functionality. The equipment supports a variety of microprocessing activities that include thin-film deposition, various thermal treatments, microphotolithography, chemical etching, inspection and characterization, bonding and packaging, and testing and measurement.

Nanobiotechnology Laboratory. The Nanobiotechnology Laboratory is equipped with capabilities to synthesize single-enzyme nanoparticles, functionalize nanostructured matrices, and analyze the activity and stability of enzymes and single-enzyme nanoparticles. This new laboratory consists of various small instruments (such as a black box, a glove box, a Dean Stark system, and shakers), a spectrophotometer, and a spectrofluorometer. A variety of basic enzyme work can be performed in this laboratory, including enzyme modification, enzyme immobilization, and enzyme-activity and stability measurements.

Upgrades

Several instrument developments are being implemented or planned to enhance capabilities and support our major research areas or areas selected for EMSL development. In FY 2005, the following capability developments occurred in the INSF.

Scanning Probe Microscopy Capability Upgrade. A new generation of scanning probe microscopy is being adapted and applied to obtain single-site chemical information of particular importance to catalytic, photocatalytic, and other chemical processes. Acquiring single-site chemical information will lead to new knowledge important in several areas; in particular, heterogeneous catalysis is indeed strongly site-specific, and for important catalytic materials such as metal oxides, reactions involve various regular and defect sites. Ideally, we would like to obtain chemically specific information on a sub-nanometer scale. The variable UHV non-contact AFM/STM that was purchased during fiscal year 2004 is an ideal system to carry out these experiments. We have added many surface-science capabilities including XPS, AES, and plasma and sputter cleaning and deposition. Although the non-contact AFM portion is not completely tested, we have started working user research activities.

Liquid Delivery System for MOCVD Capability. MOCVD is a highly effective and useful approach for growth of many oxide and nanostructured materials. The system in EMSL is being updated to allow the use of new types of environmentally friendly and lower-cost chemical precursors. MOCVD is particularly applicable for growth of materials less suitable for PVD, MBE, or other high-vacuum-based methods, and we plan to expand spintronics and oxide-based nanomaterials use of this updated system. Although the MOCVD capability had been oversubscribed and there had been extensive output in peer-reviewed journals, the system did not allow use of new generations of precursors or precise control of composition of new multi-component systems. We have upgraded the capability with a new liquid delivery system and are integrating all the instrumentation so operation of MOCVD instrumentation will be user friendly.

Heavy Ion Elastic Recoil Detection Analysis Capability. Critical light element analysis involves several EMSL-associated research areas, including oxide thin films for optical, magnetic, and catalytic materials and characterization of environmental and biological samples. A high-resolution TOF ERDA capability at the EMSL accelerator facility is being developed to expand the speed, sensitivity, and reliability of such analyses. The TOF ERDA technique will provide simultaneous detection and absolute quantification of hydrogen, carbon, nitrogen, oxygen, and other light elements as a function of depth in complex matrices containing heavy elements, and as a result, considerable attention is being devoted to developing this capability in ion-beam facilities. Because this is a powerful method to investigate elemental concentrations in the surface regions, this capability can be effectively applied in many different areas. We started developing this capability in the middle of fiscal year 2004. It is 70 percent complete, and we will be using the capability in user research in the middle of fiscal year 2006.

Addition Effusion Cells. This unique EMSL-designed, state-of-the-art, oxygen plasma-assisted MBE system, on which much of our oxide work is based, was upgraded with additional effusion cells and a new plasma source. The total number of individually controlled MBE sources is now seven—four e-beams and three effusion cells. In addition, as discussed above, we plan to purchase a cryo TEM to enhance the electron microscopy capabilities in biological areas.

Cryo-TEM. Imaging of mineral/biological and other hard/soft interfaces is of increasing importance in geochemistry and in nanobiotechnology. New microscope capabilities will significantly expand our ability to examine these interfaces. As a part of this effort, we have purchased and installed a cryo-TEM and accessories. We presently are testing the capabilities of the system. We anticipate that this capability will be fully functional later in fiscal year 2006.

Future Directions

Overall objectives of this facility are to support our current highly productive users and user base and to expand our outreach and capabilities related to the developing areas associated with EMSL science themes and grand challenges. We will take necessary actions to develop capabilities that would be crucial to achieve these goals.

User Support

- Based on the number of users and their publications, our current user base is strong and productive. One objective is to maintain that base and high level of user-produced output.
- Considering our distinguished and prominent user base, we will strive to continue receiving more than 330 proposals and realizing at least 115 journal publications each year. Our long-term goal is to increase the number of peer-reviewed publications, especially in high-profile journals. In addition, we will focus our best efforts to increase the number of high-profile users.

New Research and Capability Development

- We will increase our contribution to the Biology and Biogeochemistry Grand Challenges. As a result, we hope to increase the number of publications produced from research in these areas. Along this line, we will fully implement the Cryo-TEM capability, and we will work toward increasing the number of high-profile users in this area. We have already made a strategic hire in this area, and we are in the process of defining a strategic biological position that will make use of the electron microscopy and scanning probe microscopy capabilities to develop new programs. This strategic hire can use the microscopy capabilities (electron and scanning probe) and surface and interface science capabilities to develop programs in biology.
- Both biological- and atmospheric-chemistry-related activities will be enhanced by a new-generation TOF SIMS capability that allows better depth resolution and extraction of information from environmentally unstable materials (i.e., biological and aerosol samples). Advances in our ion-beam analysis capability will allow increased time resolution for atmospheric chemical analysis. We have already made a strategic hire to manage the SIMS capabilities and interact with scientists in the atmospheric chemistry and biological areas.
- We will complete the following capability developments in fiscal years 2006 and 2007, and will develop the user base for these capabilities:
  - metal organic chemical vapor deposition
  - heavy ion elastic recoil detection analysis
  - Cryo-TEM
- The UHV STM/AFM capability is almost operational. Although we need to complete the non-contact AFM portion of the capability, we have already started working with users in this instrumentation. We will continue to expand the user base during fiscal year 2006. The instrument will be limited to five to six users per year. Currently, we have four to five users, and we will increase this to a maximum of six.

- We will increase the user base for the new MOCVD capability. Here again, we cannot have more than five to six users per year because of cross-contamination issues. Currently, we have two users, and we will strive to increase the number of users to the maximum of five to six in the next one to two years.
- The environmental TEM capability has been approved, and we are working with external and internal users to establish specifications and develop the instrumentation and capability. Our goal is to make this capability available for the users during fiscal year 2007.

Studies of Damage Accumulation in 4H Silicon Carbide by Ion-Channeling Techniques

Y Zhang,[a] F Gao,[b] W Jiang,[b] DE McCready,[a] and WJ Weber[b]
(a) W.R. Wiley Environmental Molecular Sciences Laboratory, Richland, Washington
(b) Pacific Northwest National Laboratory, Richland, Washington

The results of non-equilibrium defects introduced by irradiation have a broad impact by providing an understanding of equilibrium defect properties and materials performance for applications in environmental restoration, energy production, and national security.

Silicon carbide (SiC) is a wide-gap semiconductor material with superior electrical, thermal, and mechanical properties that can be used for high-power, high-frequency, and high-temperature or heterostructure applications. Doping in SiC is quite a challenge, because the thermal diffusion of dopants requires extremely high temperatures. Furthermore, epitaxial growth processes do not allow planar selective area doping, which is essential to fabricating devices. Ion implantation is a critical technique used to selectively introduce dopants when producing SiC-based devices at low temperatures. However, ion implantation produces defects and even amorphization of the crystalline lattice. Therefore, understanding defect production, accumulation, and damage-annealing mechanisms, which are essential to implementing implantation doping techniques in SiC-based electronic device fabrication, is one of the critical issues for SiC device fabrication.

In this work, single-crystal 4H-SiC was irradiated with 2-MeV gold ions at 165 K. Ion-induced defect configurations and damage accumulation were then studied by ion-channeling techniques along the <0001>, $<\bar{4}40\bar{3}>$, and $<\bar{2}20\bar{1}>$ directions. The Rutherford backscattering and nuclear analysis reaction spectra along the <0001> direction shown in Figure 1 are representative for the other orientations. The increase in disorder on both the silicon and carbon sub-lattices with increasing ion fluences is clearly evident in Figure 1. The disorder profiles of silicon sublattice along the three orientations are shown in Figure 2 for the as-implanted sample to a fluence of 1.1 × 1013 cm^{-2}, which represents the general behavior for other ion fluences. The results clearly show a higher degree of disorder along the $<\bar{4}40\bar{3}>$ and $<\bar{2}20\bar{1}>$ directions over the whole implantation range.

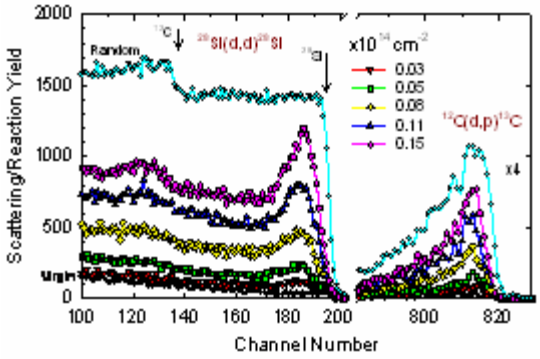

Figure 1. <0001>-aligned Rutherford back-scattering and nuclear reaction analysis spectra for 4H-SiC irradiated with 2.0-MeV gold ions to different ion fluences at 165 K.

The relative disorder on the silicon and carbon sublattices at the damage peak for the as-implanted samples is shown in Figure 3 as a function of the local dose (dpa). A sigmoidal dependence of damage accumulation on dose is observed along all three directions and on both sublattices. A nonlinear dependence of damage accumulation is observed for both the silicon and carbon sublattices along all three directions, and the relative disorder observed along the $<\bar{4}40\bar{3}>$ and $<\bar{2}20\bar{1}>$ directions is much higher than that along the <0001> direction, as shown in Figure 3. The damage accumulation can be described by a disorder accumulation model, which indicates that defect-stimulated amorphization is the primary amorphization mechanism in SiC, and the high-disorder level for the large off-axis angles is attributed to particular defect configurations. Molecular dynamics simulations demonstrate that most single interstitial configurations are shielded by silicon and carbon atoms on the lattice sites along the <0001> direction, which significantly reduces their contribution to the backscattering/reaction yield along the <0001> direction.

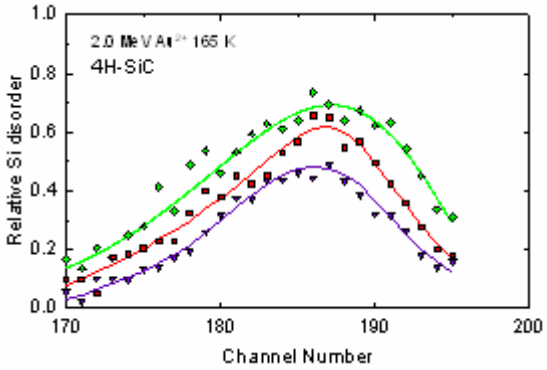

Figure 2. Relative silicon disorder along different orientations under 2-MeV Au^{2+} irradiation to a fluence of 1.1 × 1013 cm^{-2} at 165 K.

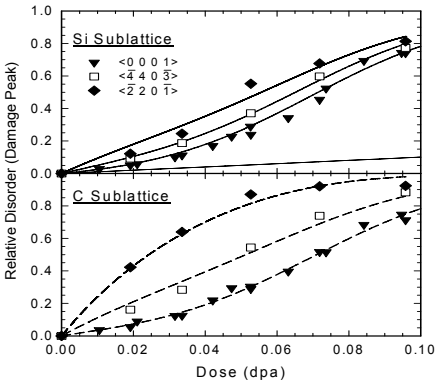

Figure 3. Relative disorder along the <0001>, $<\bar{4}40\bar{3}>$, and $<\bar{2}20\bar{1}>$ directions on both the silicon and carbon sublattices as a function of local dose at the damage peak.

Mechanism of Heteroepitaxial Growth at Initial Stages of Oxide Nanodot Formation: Cu_2O on $SrTiO_3(100)$

IV Lyubinetsky,[(a)] A El-Azab,[(b)] AS Lea,[(a)] S Thevuthasan,[(a)] and DR Baer[(b)]
(a) W.R. Wiley Environmental Molecular Sciences Laboratory, Richland, Washington
(b) Pacific Northwest National Laboratory, Richland, Washington

An efficient way of making hydrogen is important for the hydrogen economy. The ability to synthesize Cu(I) oxide quantum dots on strontium titanate surfaces is important for exploring applications related to photocatalytic splitting of water into hydrogen and oxygen or reduction of organic matter using sunlight. This work highlights the recent success of growth and characterization of Cu(I) oxide quantum dots.

The initial stages of island growth and interface formation have been examined by x-ray photoelectron spectroscopy (XPS). Spectra were acquired *in situ* at different stages of growth in a step-by-step mode by temporarily interrupting growth at a particular thickness and quenching the sample to room temperature. A series of copper $2p_{3/2}$ spectra taken at the very initial stages of the growth at 760 K are presented in Figure 1(a). At the very initial stages of Cu_2O nanodot growth, a small spectral feature associated with the Cu(II) state appeared at ~934.5 eV and disappeared at d > 0.8 nm. This observation indicates some additional interaction between deposited copper atoms and oxygen of the $SrTiO_3$ substrate.

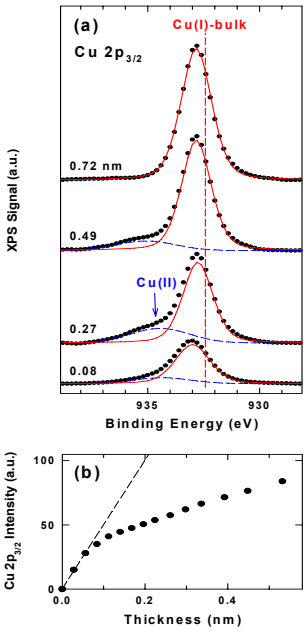

Figure 1. (a) Sequence of the copper $2p_{3/2}$ spectra, and (b) copper $2p_{3/2}$ intensity evolution for increasing effective thickness.

The intensity of the copper $2p_{3/2}$ signal as a function of the Cu_2O effective thickness at the very initial stages of growth is shown in Figure 1(b) where there is an apparent deviation from linear rise of the signal. This finding suggests an absence of the continuous (wetting) layer formation, which otherwise would exhibit a linear increase during uniform growth of the first monolayer. Thus, Cu_2O on the $SrTiO_3(100)$ evidently grows via an island formation mechanism, with the metal oxide clusters starting to grow already at sub-monolayer coverages.

Atomic force microscope (AFM) images of surface morphologies, acquired *ex situ* at different stages of growth, are shown in Figure 2. At very initial stages shown in Figure 2(a), AFM examination shows the formation of isolated square-based, truncated small nanodots with widths and heights in the range of ~8-15 nm and of 0.8 to 2.0 nm, respectively. This is consistent with results from XPS intensity analysis of the initial island formation at submonolayer coverages, discussed above. Thus, the flat areas between nanodots are, apparently, uncovered $SrTiO_3(100)$ surface. Both the shape and orientation of nanodots, with edges mostly along the <011> direction, indicate a crystalline

ordering and epitaxy. Further deposition results in an increase of nanodot density, as Figure 2(b) demonstrates for a 1.7-nm effective thickness. Comparison of the magnified image parts [inset of Figure 2(b)] reveals that lateral dimensions of nanodots do not change significantly in the process of initial quasi-planar growth. As a result, a dense layer of small, low-aspect-ratio nanodots forms at this stage of growth. In addition to the small nanodot layer, a sub-population of considerably larger rectangular- and hexagonal-based clusters, with average lateral and vertical dimensions of 30 to 80 and 6 to 16 nm, respectively, also appear, as shown in Figure 2(b). Large nanodot density increases when growth proceeds to a larger thickness. It is remarkable that these large dots start to form only when the small nanodots reach some critical density of ~10^{13} cm^{-2}, which occurs at d ~1.5 nm for a 760-K growth temperature.

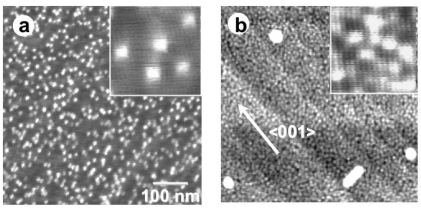

Figure 2. AFM images of the surface morphology evolution with thickness: (a) d = 0.3, (b) d =1.7 nm. Inset: part of the image magnified approximately three times.

In the studied system, the Cu_2O nanodot dimensions only weakly increase at the initial stages of growth, while continued deposition leads to an increase of dot density. A weak dependence of nanodot size on coverage indicates an existence of the optimal island size at initial stages of growth. The appearance of the larger-size dots beyond a certain density cannot be explained by a conventional ripening mechanism or by preferential direct growth of a subset of the small nanodots. If any of these mechanisms had been operable in the studied system, some more general transition would be expected in the size distribution from the small islands to the large ones. We propose that dot coalescence, driven by increasing dot density, decreasing separation, and fluctuations in dot size and separation during the growth/formation process, is the mechanism responsible for the sudden appearance of large dots superimposed on the distribution of small ones. To test this hypothesis, we used the kinetic model of the surface morphological evolution. It is based on surface diffusion driven by the elastic strain gradient and curvature of the surface, with or without interaction between neighboring dots. Figure 3 shows three snapshots of a distribution of dots, in which two dots are placed at a separation small enough to trigger interaction between the two dots. It is observed that when two dots are close enough, stress and diffusion cause the two dots to coalesce, leading to a larger dot that grows rapidly and adjusts to a different shape.

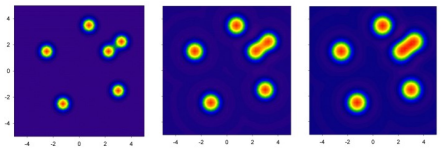

Figure 3. Simulated snapshots of evolution of the nanodot morphology.

Cleanup of Environment Using Iron Nanoparticles

DR Baer,[(a)] EJ Bylaska,[(a)] KH Pecher,[(a)] JE Amonette,[(a)] BD Kay,[(a)] M Dupuis,[(a)] JC Linelon,[(a)] DW Matson,[(a)] RL Penn,[(b)] MD Drissen,[(b)] PG Tratnyek,[(c)] JT Nurmi,[(c)] V Sarathy,[(c)] MH Engelhard,[(d)] and C Wang[(d)]

(a) Pacific Northwest National Laboratory, Richland, Washington
(b) University of Minnesota, Minneapolis, Minnesota
(c) Oregon Health and Science University, Portland, Oregon
(d) W.R. Wiley Environmental Molecular Sciences Laboratory, Richland, Washington

Work resulting from a collaboration involving Pacific Northwest National Laboratory (PNNL), the Oregon Health and Science University, and the University of Minnesota has shown that some types of iron nanoparticles reduce carbon tetrachloride contamination in water in a more environmentally benign way than larger iron particles or other iron nanoparticles.

The use of nanosized particles of iron for cleaning up contaminants in groundwater, soil, and sediments is an exciting new technology contributing to general enthusiasm about nanotechnology. However, there are many unanswered questions about the appropriate and optimal implementation of the nanoiron technology. Researchers from PNNL and collaborators from the Oregon Health and Science University and the University of Minnesota have been working several years to understand and exploit the chemical properties of iron nanoparticles (Nurmi et al. 2005; Borchardt 2005a, b). In this research, systematic chemical reaction experiments with nanoparticles have identified characteristics of nanosized iron particles that may enhance their ability to remove carbon tetrachloride contamination in groundwater.

Carbon tetrachloride is a manufactured toxic chemical historically used in cleaning fluids, as a degreasing agent, and as part of chemical processing. In many locations around the world, industrial waste and spilled liquids have infiltrated the soil and created very large areas of contaminated groundwater and soil.

Our interdisciplinary team includes 10 researchers from PNNL, three from Oregon Health and Science University, and two from the University of Minnesota. The PNNL researchers have synthesized and characterized several different iron nanoparticles using a variety of advanced microscopy and spectroscopy techniques at the W.R. Wiley Environmental Molecular Sciences Laboratory. Chemical reactivity experiments were carried out both at PNNL and the Oregon Health and Science University using electrochemical techniques.

Several reports indicate that nanosized zero-valent iron (Fe^0) exhibits greater reactivity than micron-sized particles of Fe^0, which would impart advantages for groundwater remediation or other environmental applications. Most of these comparisons were preliminary in that many potentially significant process variables, including the nature of the particles involved, were either uncontrolled or unresolved. To better understand the reactivity of these iron particles, we collected a range of iron nanoparticles with different sizes and processing histories. Because different synthesis, processing, and handling methods produce nanoparticles of various size distributions, with a variety of surface coatings and contaminants,

the nanoparticles may have a significant range of chemical behaviors and reaction properties. Our research focused on measurements of the physical and chemical properties of two materials that have been tested at environmental remediation sites. These iron nanoparticles included single-crystal nanoparticles and aggregates of nanoparticles. The particles studied ranged in size from 10 to 100 nm, with the particles coated by an iron oxide layer of a typical thickness of 2 to 3 nm or a coating rich in oxidized boron (Figure 1) resulting from the synthesis process. Although the reaction rates of the two nanoparticles were similar, the reaction products were significantly different. A commercially produced nanoparticle material that contained both metal particles with a crystalline oxide coating along with fully oxidized nanoparticles degraded carbon tetrachloride to a mixture of relatively harmless products, while larger-sized iron particles and those with boron-rich coatings produced significant amounts of chloroform, an undesirable and toxic by-product (Figure 2).

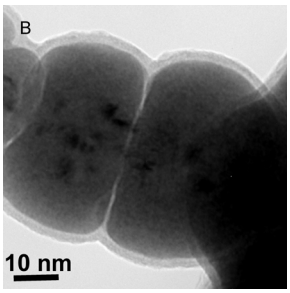

Figure 1. High-resolution transmission electron microscopy image showing the nature of the "protecting" layer on a metallic iron nanoparticle.

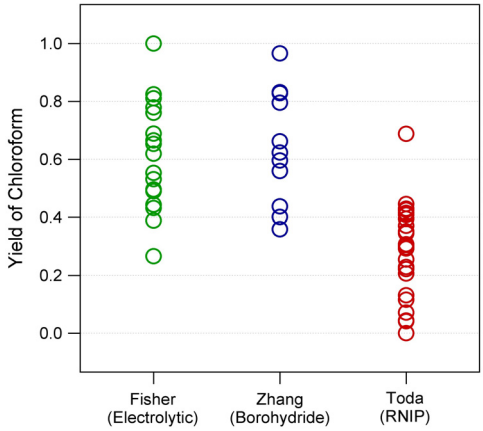

Figure 2. Yield of chloroform versus type of iron nanoparticles. Low chloroform yield suggests two-electron reaction pathway products: carbon monoxide, etc. Chloroform yield is typically 60 to 80 percent with iron, but one type of nanoiron yields <0.5. The yield likely is controlled by the composition of the oxide shell.

Citations

Borchardt JK. February 10, 2005a. "Small Science May Clean a Big Problem." *Christian Science Monitor*, http://www.csmonitor.com/2005/0210/p14s01-sten.html.

Borchardt JK. February 10, 2005b. "Nanotech Shows Promise for Cheaper Superfund Cleanup." *USA Today*, http://www.usatoday.com:80/tech/news/nano/2005-02-10-nano-iron-cleanup_x.htm.

Nurmi JT, PG Tratnyek, V Sarathy, DR Baer, JE Amonette, K Pecher, C Wang, JC Linehan, DW Matson, RL Penn, and MD Driessen. 2005. "Characterization and Properties of Metallic Iron Nanoparticles: Spectroscopy, Electrochemistry, and Kinetics." *Environmental Science and Technology* 39(5):1221-1230.

Nanostructures for Enzyme Structures

J Kim,[(a)] JH Kwak,[(a)] JW Grate,[(a)] AS Lea,[(b)] C Wang,[(b)] J Lee,[(c)] CW Lee,[(c)] KS Min,[(c)] HB Na,[(c)] HK Ahn,[(d)] and BS Kim[(d)]

(a) Pacific Northwest National Laboratory, Richland, Washington
(b) W.R. Wiley Environmental Molecular Sciences Laboratory, Richland, Washington
(c) Seoul National University, Seoul, South Korea
(d) Chungbuk National University, Chongju, South Korea

Enzymes are useful biocatalysts of nanometer scale that regulate the chemistry of cells and organisms. The potential application of enzymes as practical biocatalysts is well recognized and also growing. The unique activities and specificities of enzymes play a key role in yielding the wide range of applications. However, the widespread application of enzymes is generally limited by their short lifetimes. We have developed various nanostructures that can be used to stabilize enzyme activity for several applications.

We have developed a new nanostructure containing an enzyme within a hybrid organic/inorganic polymer network with sufficient porosity to allow substrates to diffuse to the active site. The procedure used to synthesize this nanostructure involves enzyme modification and two orthogonal polymerization steps. It yields nanoparticles containing a single enzyme that can be observed by transmission electron microscopy (Figure 1). In experiments with α-chymotrypsin, incorporation into the nanostructure dramatically increased enzymatic stability. Furthermore, the nanoscale structure around the enzyme is sufficiently thin so that it does not impose a significant mass transfer limitation on the substrate. Because these nanoparticles remain soluble or suspended in solutions, they can be processed into a variety of forms.

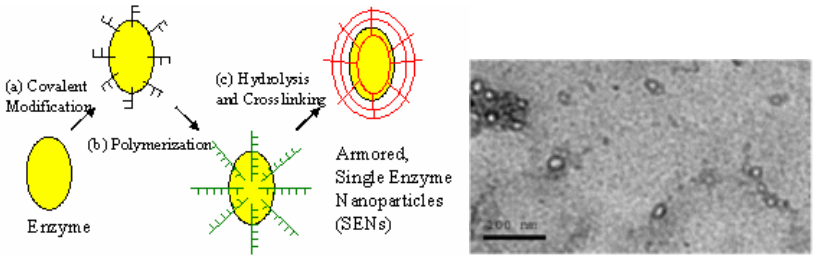

Figure 1. Left: Schematic of single-enzyme nanoparticle synthesis. Right: Transmission electron microscopy images of single-enzyme nanoparticles containing α-chymotrypsin.

The second nanostructure is mesoporous media (Figure 2). We have developed nanoscale enzyme reactors in mesoporous silica via a ship-in-a-bottle approach, which employs adsorption of enzymes followed by cross-linking using glutaraldehyde treatment. Mesocellular mesoporous silica, small particles (200 to 500 nm) with large mesocellular pores (37 nm) connected by mesoporous channels (13 nm), was selected as a carrier of nanoscale enzyme reactors. The resulting nanoscale enzyme reactors show an impressive stability and activity with an extremely high loading of enzymes. For example, nanoscale enzyme reactors containing α-chymotrypsin could hold 0.5 g of chymotrypsin in 1 g of silica, which is comparable to the maximal loading of chymotrypsin in mesocelluar mesporous silica.

However, the specific activity of nanoscale enzyme reactors containing α-chymotrypsin was 4.2 times higher than that of the adsorbed chymotrypsin, with a lower loading (0.07 g of chymotrypsin per 1 g of silica), which was further decreased by a continuous leaching of adsorbed chymotrypsin.

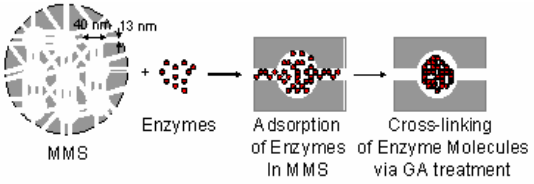

Figure 2. Schematic diagram for nanometer-scale enzyme reactors mesocellular mesoporous silica.

The final nanostructure is electrospun nanofibers. Nanofibers consisting of enzyme-polymer composites have been directly prepared (Figure 3) by electrospinning a toluene solution containing surfactant-stabilized enzyme and polymer.

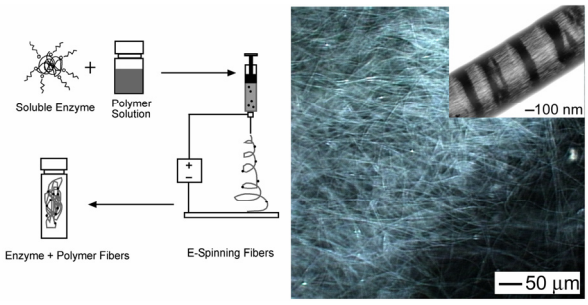

Figure 3. Schematic diagram for the preparation of enzyme-polymer composite nanofibers.

Additional treatment with glutaraldehyde could greatly stabilize the enzyme activity of the fibers, which could be maintained in a buffer under shaking conditions for more than two weeks. The nanofibers also showed great improvement in the enzyme activity over bulk films as a result of increased mass transfer for substrate molecules to and from the enzyme reactive sites. The apparent specific activity of nanofibers with an enzyme loading of 6.3 percent could be achieved up to 40 percent of that of free enzymes. These stable and catalytically active nanofiber-based mats were highly durable and could be easily recovered from a solution, making them ideal candidates for large-scale applications. We have also developed a unique approach for the fabrication of enzyme aggregate coatings on the surfaces of electrospun polymer nanofibers. This approach employs covalent attachment of seed enzymes onto nanofibers consisting of a mixture of polystyrene and poly (styrene-co-maleic) anhydride, followed by a glutaraldehyde treatment that cross-links additional enzyme molecules and aggregates from solution onto the covalently attached seed enzyme molecules. These cross-linked enzyme aggregates, covalently attached to the nanofibers via the linkers of seed enzyme molecules, are expected to improve both the enzyme activity and stability due to increased enzyme loading.

Nitrogen Analysis Using Energetic Ion Beams

W Jiang,[(a)] V Shutthanandan,[(b)] S Thevuthasan,[(b)] C Wang,[(b)] and WJ Weber[(a)]
(a) Pacific Northwest National Laboratory, Richland, Washington
(b) W.R. Wiley Environmental Molecular Sciences Laboratory, Richland, Washington

As a special case of nuclear reaction analysis, nuclear elastic scattering analysis (or non-Rutherford scattering analysis) is one of the important methods in ion-beam analysis, and it is the preferred technique for analyzing light elements in a heavy matrix. To quantify the light elements, the cross sections of the elements need to be established to perform the nuclear elastic scattering analysis. This study reports cross sections for $^{14}N(p,p)^{14}N$ and $^{14}N(\alpha,\alpha)^{14}N$ at a scattering angle of 150° in the laboratory system.

The excitation curves for $^{14}N(p,p)^{14}N$ in the proton energy range from 2.480 to 3.230 MeV are shown in Figure 1. Both the data from this experiment at θ_{Lab} = 150° and the data of Bashkin and co-workers (1959) for θ_{Lab} = 159.5° show a sharp nuclear resonant peak at ~3.2 MeV. The peak intensity and full width at half maximum (FWHM) at 150° correspond to 24σR and 20 keV, respectively. Although the FWHM is small, this width corresponds to ~900 nm in materials such as GaN because of the small stopping powers of the energetic protons. For this reason, analysis of ^{14}N in solids can be performed around the resonant peak over a small range of energy (ΔE ≈ 5 keV) at 150° for which the variation of the scattering cross sections is ~10%. Besides the resonance, there is also a cross-section plateau (~6.8σR) over a wide range of energy from 2.48 to 3.15 MeV for elastic scattering at 150°. The energy width (~700 keV) of the plateau corresponds to a depth of ~28 μm for GaN, based on the SRIM-2003 database. This plateau can be used to quantify the ^{14}N (total content) in solids. However, for conventional ion-beam analysis using surface-barrier detectors, this cross-section plateau is not strongly recommended for profiling ^{14}N because the depth resolution is poor, on the order of 150 nm. For He^+ elastic scattering from ^{14}N, the cross-section data are shown in Figure 2 for θ_{Lab} = 150° (this experiment) and θ_{Lab} = 165° (from Feng et al. 1994). At a scattering angle of 150°, the cross section

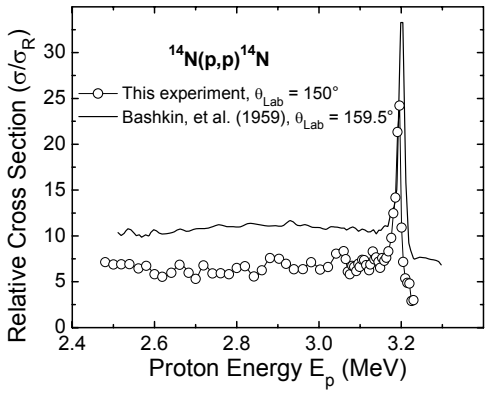

Figure 1. Cross section of H^+ backscattering from ^{14}N at 150° as a function of ion energy. Also included are the data at θ_{Lab} = 159.5° from Bashkin and co-workers (1959).

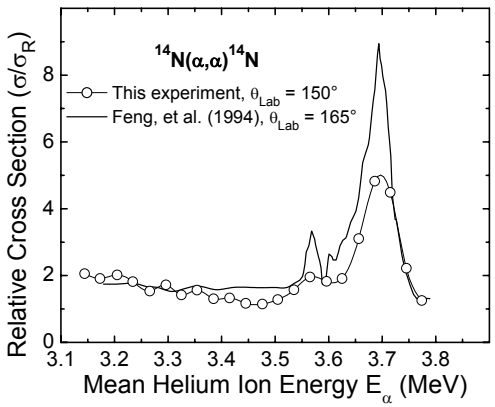

Figure 2. Cross section of He^+ backscattering from ^{14}N at 150° as a function of ion energy. Also included are the data at θ_{Lab} = 165° from Feng and co-workers (1994).

decreases gradually from 2σR to σR with increasing ion energy over the range between 3.144 and 3.505 MeV. At 3.565 MeV, there is a small resonant peak (1.96σR), followed by a stronger nuclear resonance located at 3.686 MeV, with the peak maximum of 4.82σR.

Although the resonant peak positions of the two datasets agree well, the intensity of the cross sections at the larger peak is greatly reduced from 8.9σR at 165° to 4.82σR at 150°. In both cases, the enhancement of the cross section is relatively small compared to the proton scattering shown in Figure 1. The resonant peak at 3.686 MeV has a FWHM of ~100 keV at 150°. Compared with the $^{14}N(p,p)^{14}N$ elastic scattering at 150°, the $^{14}N(\alpha,\alpha)^{14}N$ scattering has a much better depth resolution (~25 nm for GaN at the surface), but the probing depth is greatly reduced (~120 nm starting from GaN surface with allowance of a 10 percent variation in cross section at the peak). The lower cross-section values of the $^{14}N(\alpha,\alpha)^{14}N$ scattering make it less favorable to analyze the total content of ^{14}N in solids as compared to the $^{14}N(p,p)^{14}N$ scattering shown in Figure 1.

As an example to illustrate nitrogen analysis based on the measured scattering cross sections, a GaN single-crystal film on an Al_2O_3 substrate was analyzed in channeling geometry along the <0001> axis (close to the surface normal). The specimen was irradiated with 1.0 MeV Au^{2+} ions to a fluence of 1.5 ions/nm² at 150 K. Conventional 2.0 He^+ Rutherford backscattering/channeling analysis leads to a broad damage peak on the gallium sublattice; however, the scattering signals from ^{14}N are completely buried by the high intensity of the gallium spectrum. Such a spectrum does not allow for the study of the nitrogen sublattice in GaN. Figure 3 shows the results from the 3.746 MeV He^+ non-Rutherford backscattering/channeling for the same sample. Clearly, the damage peaks on both the gallium and nitrogen sublattices in GaN appear in the spectrum. Based on a slightly higher energy (3.8 MeV) of He^+ ions, the accumulation of disorder on both the gallium and nitrogen sublattices in wurtzite GaN has been studied as a function of ion fluence.

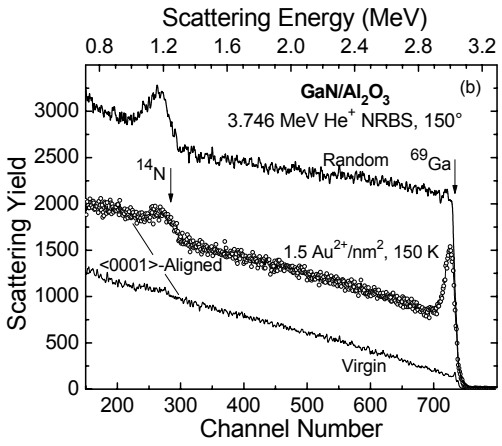

Figure 3. A typical example showing the energy spectra of 3.746 MeV He^+ non-Rutherford backscattering/channeling for a GaN film on a sapphire substrate.

Citations

Bashkin S, RR Carlson, and RA Douglas. 1959. "Cross Section for Elastic Scattering of Protons by N^{14}." *Physical Review* 114(6):1552-1553.

Feng Y, Z Zhou, G Zhau, and F Yang. 1994. "Cross Sections for 165° Backscattering of 2.0-9.0 MeV ^4He Ions from Nitrogen." *Nuclear Instruments and Methods in Physics Research Section B: Beam Interactions with Materials and Atoms* 94:11-14.

Defect Configuration and Relaxation in 4H Silicon-Carbide

Y Zhang,[(a)] F Gao,[(b)] W Jiang,[(b)] DE McCready,[(a)] and WJ Weber[(b)]
(a) W.R. Wiley Environmental Molecular Sciences Laboratory, Richland, Washington
(b) Pacific Northwest National Laboratory, Richland, Washington

The wide-band-gap semiconductor silicon carbide (SiC) has remarkable physical, chemical, and electronic properties that make it very attractive for high-speed communications and high-temperature, high-frequency, high-power applications. Doping SiC material is necessary for these applications, and ion implantation can be used effectively for doping. This study investigates the effects induced by ion irradiation in SiC.

Ion implantation is the only planar, selective-area doping technique available for SiC because the diffusion coefficients of impurities in SiC are negligibly small at or below 1800 K. Ion implantation, however, inevitably produces a significant concentration of defects and lattice disorder, which lead to a growth of secondary defects or other polytype structures during post-implantation annealing or high-temperature operation. Failure of prototype devices is often associated with point defects or larger agglomerates of point defects formed by the implantation process or during post-implantation annealing. One of the critical issues for SiC device fabrication is to understand defect configuration, relaxation, and annihilation following annealing. Irradiation-induced defects are studied for both the silicon and carbon sublattices in 4H-SiC under 2 MeV gold-ion irradiation at 165 K in 4H-SiC using ion channeling techniques along two crystallographic directions (Figure 1).

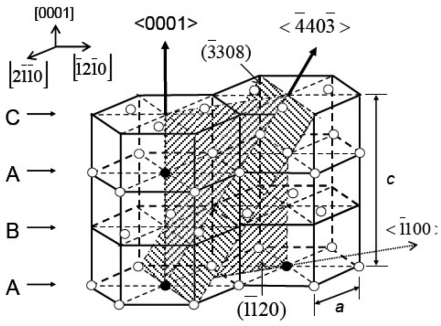

Figure 1. The first stacking sequence of the silicon sublattice in 4H-SiC with the axes <0001> and <4403> indicated. The filled symbol is used when the silicon atom is on the corresponding axis.

Molecular dynamics simulations on defect evolution in SiC under ion irradiation indicate that energetic ions primarily produce interstitials, monovacancies, antisite defects, and small defect clusters within collision cascades. In covalent SiC, dumbbell interstitials are important defects because of their low formation energies, as shown in Figure 2. In addition to dumbbell interstitials, there are other possible single interstitial configurations. For example, the seven carbon interstitial configurations are illustrated in Figure 3. The molecular dynamics results demonstrate that most single interstitial configurations are formed on the silicon-carbon dimer rows that are parallel to the <0001> direction. When aligning the probe beam

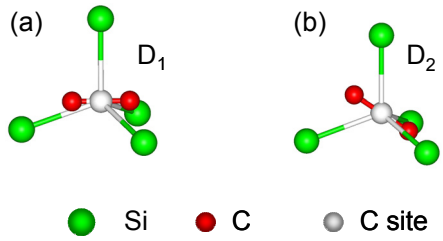

Figure 2. Fundamental structure of dumbbell interstitials: (a) D_1 and (b) D_2. The light gray spheres and cylinders show the tetrahedron in the ideal lattice.

along the <0001> direction, the D_1 and D_2 dumbbell interstitials and the C_H and Si_H type single interstitials can be detected.

The other single interstitial configurations are shielded from the analysis beam by the silicon-carbon rows along the <0001> direction and, therefore, will not contribute to the backscattering/reaction yield. On the other hand, along the $<\bar{4}40\bar{3}>$ direction, all seven possible configurations for the single interstitials and all the dumbbell interstitials are accessible to the probe beam used for Rutherford backscattering spectroscopy and ^{12}C $(d,p)^{13}C$ nuclear reaction analysis. Because all interstitial configurations contribute to the backscattering along the $<\bar{4}40\bar{3}>$ direction, a significantly higher relative disorder is observed on both the silicon and carbon lattices along this direction.

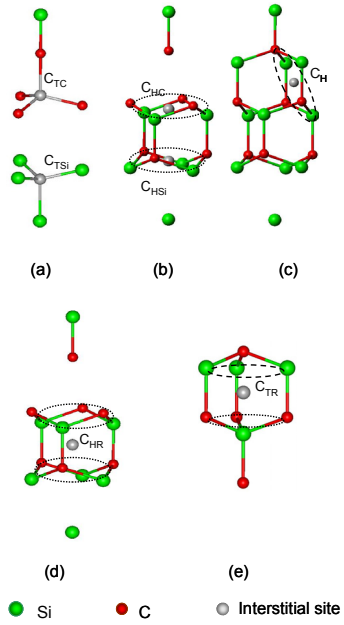

Figure 3. Seven possible positions for carbon single interstitials, two tetrahedral positions on the long row as (a), three hexagonal positions as (b) and (c), and two highly symmetric interstitial structures, as (d) between the two hexagonal Si_3C_3 rings on the long row and (e) between a trigonal Si_3 and a trigonal C_3 rings on the short row.

After completion of the channeling measurements for the as-implanted samples, isochronal annealing was carried out sequentially at temperatures from 200 to 870 K. The relative residual disorders for the higher-dose samples at the damage peak for both the Si and C sublattices were determined along both directions after each annealing. The relative increase at 200 K along the $<\bar{4}40\bar{3}>$ direction, particularly for the C sublattice, is associated with the relaxation of defects to lower-energy configurations that give an increased contribution to the backscattering. As the annealing temperature further increases, the residual disorder decreases along both the <0001> and $<\bar{4}40\bar{3}>$ directions. At higher annealing temperatures, interstitials will migrate, resulting in annihilation or clustering. This leads to a decrease in the concentration of local defects and some defect-stimulated epitaxial recrystallization of amorphous domains. Above room temperature, there is a recovery stage at ~500 K that is more pronounced for high-dose samples. This recovery stage is not observed by positron lifetime spectroscopy, which suggests that vacancy defects are unaffected by the recovery process at these temperatures.

Complete recovery of the residual disorder is not observed on either sublattice or along either direction after annealing up to 870 K because of residual amorphous domains and stable defect clusters. Thermal annealing at 1300 K or higher is necessary for complete restoration of the crystalline order.

Formation of Cadmium Nanowires on Ion-Cut Surfaces of $Cd_2Nb_2O_7$

W Jiang,[(a)] WJ Weber,[(a)] C Wang,[(b)] JS Young,[(b)] LA Boatner,[(c)] J Lian,[(d)] LM Wang,[(d)] and RC Ewing[(d)]

(a) Pacific Northwest National Laboratory, Richland, Washington
(b) W.R. Wiley Environmental Molecular Sciences Laboratory, Richland, Washington
(c) Oak Ridge National Laboratory, Oak Ridge, Tennessee
(d) University of Michigan, Ann Arbor, Michigan

Nanowires of semiconductors and metals are of technological interest because of their potential applications in many fields, including electronics, magnetics, optoelectronics, thermoelectrics, and photonics. Use of these materials rather than their bulk counterparts will not only allow for device miniaturization, but also may improve device performance or create new functions. We describe a novel method for the synthesis of crystalline cadmium nanowires without involving either templates or a "seeded" structure.

Irradiation of a $Cd_2Nb_2O_7$ single crystal using 3.0-MeV He^+ ions at and below room temperature has been performed and formation of nanowires on the ion-cut surfaces was observed (Figure 1). The 70°-tilted view of the nanowires reveals a variety of diameters, lengths, and shapes. The wires are randomly distributed on the ion-cut surfaces; they can be as long as several tens of microns with diameters ranging from less than 100 nm to nearly 1 μm. Some of the wires have a granular knob at the top of the nanowire (Figure 1a); both straight and curved wires are abundant (Figure 1b). In general, the sidewalls of the thin wires are relatively smooth and their diameters are uniform, while the thicker wires have a "ridged" surface. The insert of Figure 1b shows a side view of a broken wire. The composition of the nanowires was determined by energy-dispersive x-ray spectroscopy. The niobium concentration throughout the nanowires is below the detection limit, although the niobium peak is stronger than that of cadmium in the original $Cd_2Nb_2O_7$ crystal. The nanowires formed primarily as metallic cadmium under these conditions, and their surfaces subsequently became oxidized when the sample was exposed to air because cadmium can be readily oxidized under ambient conditions. The backside of the exfoliated layer was also analyzed using energy-dispersive x-ray spectroscopy; the results show that it consists primarily of niobium and oxygen with no detectable cadmium.

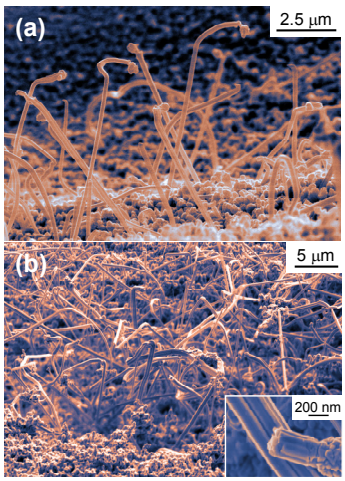

Figure 1. a: 70°-tilted view of short nanowires on an ion-cut surface. b: General view (70°-tilted) of an ion-cut surface containing nanowires. The irradiation dose for (b) is greater. Insert to (b) shows the side view of a broken nanowire.

To characterize the atomic-scale structure by transmission electron microscopy, several nanowires on the ion-cut surfaces were placed on a copper grid with a thin formvar support film that was coated with a few atomic layers of carbon. Figure 2 shows a typical nanowire of ~80 nm in diameter. There appear to be two facetted faces at the tip of the wire, suggesting that the wire is a single crystal. The insert of the figure shows a selected-area electron diffraction (SAED) pattern for the area marked on the wire. The bright spots in the diffraction pattern, which are grouped with dashed lines, confirm that the nanowire in this region is mono-crystalline. Assuming that the wire has the same structure as bulk cadmium, the diffraction maxima are from the (02-23) and (10-13) planes, as indicated in the SAED insert of Figure 2. The two symmetric, but faint, spots indicated by arrows might originate from the thin CdO shell of the nanowire, which is consistent with the nanowire composition.

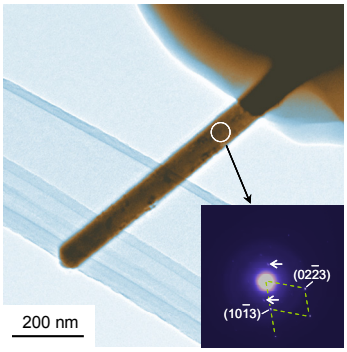

Figure 2. Transmission electron microscopy micrograph for a single nanowire. The insert is the SAED image for the nanowire. The diffraction pattern suggests that the nanowire is a single crystal. The two arrows point to faint diffraction maxima that may have resulted from the CdO layer on the surface of the nanowire.

During the irradiation of $Cd_2Nb_2O_7$, implanted helium–and perhaps some oxygen–accumulate at the peak in the irradiation-induced vacancy concentration and near the projected range of the implanted helium. Prior to surface exfoliation, there is a gas-accumulation and bubble-formation stage that forms a blister-like structure in which the upper surface layer begins to separate from the underlying substrate and bows outward under the high gas pressure. At this stage, there is high compressive stress on the inside of the top layer; as a result, the phase-separated, soft metallic cadmium possibly is extruded as wires through the pores in the material. Such cadmium wires may also be simultaneously pulled from the inner top layer because the bond strength at the interface between the metallic cadmium and the underlying substrate is much stronger than that of the metallic cadmium within the residual niobium and niobium-oxide in the decomposed top layer. Consequently, some of the thick cadmium wires may be strong enough to survive the pulling process. In addition, a probable volume expansion induced by amorphization of $Cd_2Nb_2O_7$ under these ion-irradiation conditions could increase the pressure on the cadmium inclusions in the decomposed material and enhance the extrusion of the soft cadmium through pores. Thermal expansion of cadmium from 140 to 295 K might also contribute to the extrusion process because the coefficient of linear thermal expansion for cadmium (30.8×10^{-6} K^{-1} at 298 K) is much larger than that for niobium (7.3×10^{-6} K^{-1} at 298 K). Mechanistically, a single-crystal structure can result from a strain-anneal process driven by the large strain produced by the extrusion process. The granular knob (Figure 1a), which has a similar composition to the crater surface, is apparently a mass of material that is pulled off the crater surface as the cadmium nanowire is extruded from the original surface. The observed surface ridges (striations or grooves) on the surface of the thick wires (Figure 1b) appear to result from the extrusion or pulling process through the large and irregular pores.

Effect of Zirconium Substitution for Titanium in $Gd_2Ti_2O_7$ Pyrochlore: Ti 2p and O 1s NEXAFS Study

P Nachimuthu,[a,b] S Thevuthasan,[c] EM Adams,[c] WJ Weber,[d] BD Begg,[e] BS Mun,[b] DK Shuh,[b] DW Lindle,[a] EM Gullikson,[b] and RC Perera[b]

(a) University of Nevada, Las Vegas, Nevada
(b) Lawrence Berkeley National Laboratory, Berkeley, California
(c) W.R. Wiley Environmental Molecular Sciences Laboratory, Richland, Washington
(d) Pacific Northwest National Laboratory, Richland, Washington
(e) Australian Nuclear Science and Technology Organization, Menai, New South Wales, Australia

Pyrochlores have a broad range of potential for different technological applications, such as catalysts, fluorescence centers, both cathode and electrolyte materials in solid-oxide fuel cells, oxygen-gas sensors at high-radiation environments, and as host matrices for the immobilization of actinide-rich wastes. In this work, we investigated the structural properties of these materials before and after ion-beam irradiation.

Of the potential applications for pyrochlores, the use in solid-oxide fuel cells and as host matrices for actinide-rich wastes are receiving increasing attention because recent studies show that the isovalent substitution of zirconium for titanium in $Gd_2Ti_2O_7$ n increases the oxygen ionic conductivity by ~4.5 orders of magnitude at 875 K and the radiation resistance increases by ~5 orders of magnitude in radiation tolerance. Recent experimental studies concluded that the cation disorder and anion Frenkel defects are the main cause for dramatic increase in oxygen ion conductivity and radiation tolerance in Gd_2Zr_2O. We have investigated structural properties of pure and irradiated single-crystal and polycrystalline $Gd_2Ti_2O_7$ and $Gd_2(Ti_{1-y}Zr_y)_2O_7$, using site-sensitive near-edge x-ray absorption fine structure (NEXAFS) and x-ray photon spectroscopy (XPS). XPS measurements suggest that the charge state shift of 1.6 eV in the O 1s binding energy between the oxygen anions in the 48f and 8b sites results from a lower electron density on oxygen with shorter gadolinium-oxygen (8b, 0.221 nm) compared to longer gadolinium-oxygen (48f, 0.254 nm) bonds. NEXAFS measurements were carried out at beam lines 6.3.2 and 9.3.2 at the Advanced Light Source, Lawrence Berkeley National Laboratory.

The Ti 2p and O 1s NEXAFS of TiO_2 (rutile), $Gd_2(Ti_{1-y}Zr_y)_2O_7$ (y=0.0-1.0), $SrTiO_3$, yttria-stabilized zirconia (y-ZrO_2), and Gd_2O_3 are shown in Figures 1(a) and (b), respectively. Although the Ti 2p NEXAFS show exactly the same features for both single-crystal and polycrystalline $Gd_2Ti_2O_7$, isovalent substitutions of zirconium for titanium in $Gd_2Ti_2O_7$ produce significantly different spectra. The notable observation found in Figure 1(a) is that the splitting of the e_g states, which indicates the degree of distortion from octahedral site symmetry, decreases with increasing zirconium substitution in $Gd_2(Ti_{1-y}Zr_y)_2O_7$. The energy separation between the d_{z^2} and $d_{x^2-y^2}$ orbitals is found to be to 1.0 eV, 0.8 eV, 0.6 eV, and 0.4 eV for $Gd_2(Ti_{1-y}Zr_y)_2O_7$ with y = 0.0, 0.25, 0.5, and 0.75, respectively. Similarly, the energy separation amounts to 1.2 eV for TiO_2. In contrast, titanium in $SrTiO_3$ occupies perfect octahedral symmetry and hence the transitions to e_g states show no splitting; however, the profile is slightly unsymmetrical. Thus, curve-fitting the transitions to e_g states of $SrTiO_3$ with two Guassians produces an energy separation of ~0.5 eV, which is very close

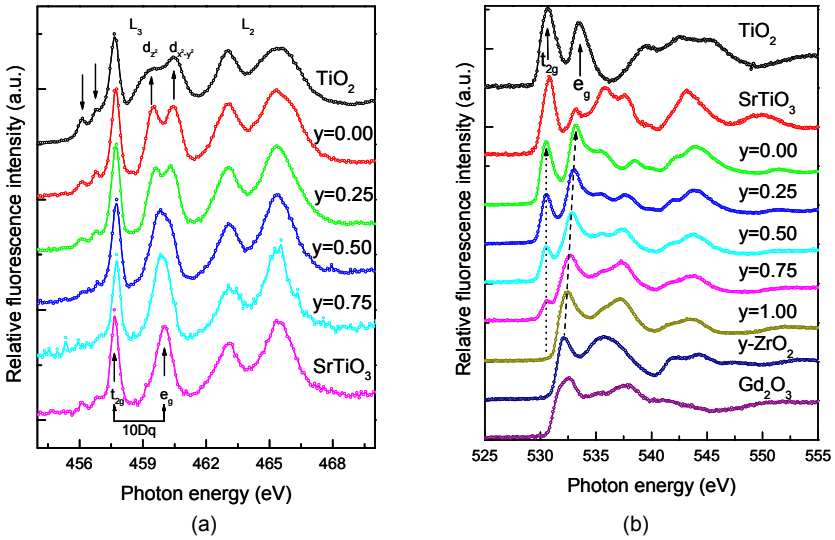

Figure 1. (a) Ti 2p NEXAFS for TiO_2 (rutile), $Gd_2(Ti_{1-y}Zr_y)_2O_7$ (y=0.0, 0.25, 0.5, and 0.75), and $SrTiO_3$; (b) O 1s NEXAFS for TiO_2 (rutile), $SrTiO_3$, $Gd_2(Ti_{1-y}Zr_y)_2O_7$ (y=0.0, 0.25, 0.5, 0.75, and 1.0), yttria-stabilized zirconia (y-ZrO_2), and Gd_2O_3.

to that of $Gd_2(Ti_{1-y}Zr_y)_2O_7$ with y= 0.75, suggesting no distortion in the TiO_6 octahedron, as in $SrTiO_3$. In addition, the magnitude of the transitions to e_g states relative to the transitions to t_{2g} states increases with increasing zirconium substitution in $Gd_2(Ti_{1-y}Zr_y)_2O_7$. Thus, these results clearly show that the titanium retains its octahedral site symmetry; however, the distortion present in the TiO_6 octahedron decreases with increasing Zr substitution for Ti.

Transitions labeled as t_{2g} and e_g in O 1s NEXAFS for TiO_2, $SrTiO_3$, and $Gd_2(Ti_{1-y}Zr_y)_2O_7$ result from transitions to the final states, Ti^{4+}: $3d(2t_{2g})^1$-O^{2-}: $(1s)^{-1}$-$2p^6$ and Ti^{4+}: $3d(3e_g)^1$-O^{2-}: $(1s)^{-1}2p^6$, respectively, where $(1s)^{-1}$ denotes a hole in the O 1s shell [Figure 1(b)]. The energy separation between t_{2g} and e_g states amounts to 2.8 eV, 2.7 eV, and 2.5 eV for TiO_2, $Gd_2Ti_2O_7$, and $SrTiO_3$, respectively, which is a direct measure of the ligand field strength of TiO_6 octahedron. O 1s NEXAFS of polycrystalline $Gd_2(Ti_{1-y}Zr_y)_2O_7$ show only the transitions from oxygen anions located in the 48f oxygen sites, which are coordinated to both Ti^{4+} and Gd^{3+}; hence, gadolinium-oxygen also contributes to intensity in the vicinity of e_g states (533.3 eV) of TiO_6 octahedron in $Gd_2Ti_2O_7$. Further, the intensities of the transitions to t_{2g} and e_g states of TiO_6 octahedron decrease, and the oxygen ions coordinated to zirconium increasingly contribute to the intensity in the vicinity of the transitions to e_g states in addition to titanium-oxygen and gadolinium-oxgyen. However, this transition shifts systematically towards lower energy with increasing substitution of zirconium for titanium in $Gd_2(Ti_{1-y}Zr_y)_2O_7$. Thus, a systematic shift towards lower energy of the transition at 533.3 eV for y = 0.0 to 532.5 eV for y = 1.0 shows an increase of zirconium coordination from 6 to nearly 8 with increasing substitution of zirconium for titanium in $Gd_2(Ti_{1-y}Zr_y)_2O_7$.

Surface Studies on Highly Active CeO_2-Supported Cu-Pd Bimetallic Catalysts for the Oxygen-Assisted Water-Gas-Shift Reaction

EB Fox,[(a)] MH Engelhard,[(b)] S Velu,[(a)] and C Song[(a)]
(a) Pennsylvania State University, University Park, Pennsylvania
(b) W.R. Wiley Environmental Molecular Sciences Laboratory, Richland, Washington

Better catalytic performance has been observed using Cu-Pd bimetallic catalysts over monometallic catalysts containing copper alone or palladium alone supported on the CeO_2 support. However, the role of copper and palladium in the catalytic performance and the surface nature of the Cu-Pd bimetallic catalysts have not been well understood. The objective of the present work is to investigate the role of palladium on the catalytic performance in the oxygen-assisted water-gas-shift (OWGS) reaction to achieve carbon monoxide reduction. Such catalysts have potential use in proton exchange membrane fuel cells.

Reformed hydrocarbon fuels may become an important source of hydrogen for proton exchange membrane fuel cells. To use these hydrogen sources, however, low levels of sulfur and carbon monoxide must be achieved. In a conventional fuel reformer for fuel-cell feed gases, the carbon monoxide reduction steps of the high- and low-temperature water-gas-shift and referential oxidation can take up more than 50 percent of the fuel-cell system's volume and weight. To reduce volume, the water-gas-shift and PrOx reactions are combined and performed in a single step—the OWGS reaction. We recently developed a new series of highly active and less pyrophoric Cu-Pd bimetallic catalysts supported on high-surface-area CeO_2 catalysts for the OWGS. A catalyst containing about 30 wt% Cu and 1 wt% Pd has been found to be optimum in order to achieve high CO conversion, close to 100 percent (around 230°C). The effect of temperature and space velocity on catalytic performance has been evaluated. In this study, we employed *in situ* x-ray photoelectron spectroscopy (XPS) and Fourier transform infrared spectroscopy studies on the Cu-Pd/CeO_2 catalysts to understand the nature of active species involved in the OWGS reaction.

The synthesis and characterization of various high-surface-area CeO_2 supports and Cu-Pd/CeO_2 catalysts have been described in our recent publication (Fox et al. 2006a, b). Cu and Pd were impregnated over a CeO_2 support in two steps, copper followed by palladium. XPS measurements of both unreduced as well as reduced catalysts were performed by a "pseudo *in situ* method" at the W. R. Wiley Environmental Molecular Sciences Laboratory. About 100 mg of the catalysts were loaded in a quartz reactor and reduced in a 5 percent H_2/Ar mixture (50 cc/min). The samples were reduced at a heating rate of 5°C/min up to 225°C and maintained at this temperature for about 1 hour before cooling to room temperature. The reactor was sealed and transferred into a glove box and the reduced catalysts were retrieved and mounted for XPS analysis without exposure to air.

XPS data of three samples, namely Cu(30)Pd(0)/CeO_2 containing only copper without palladium, Cu(0)Pd(1)/CeO_2 containing only palladium without copper, and Cu(30)Pd(1)/CeO_2 containing both copper and palladium in the unreduced as well as reduced form, have been collected to understand the effect of palladium on the surface chemical properties of Cu/CeO_2 catalysts. The unreduced samples exhibited peaks corresponding to Cu^{2+}, Pd^{2+}, and Ce^{4+} species in these samples. Upon reduction around 225°C, the Cu^{2+} and Pd^{2+} species are reduced mainly to their metallic states, while cerium exists mainly in the Ce^{4+} state.

Figure 1 shows the XPS spectra of reduced Cu-Pd/CeO_2 catalysts in the copper 2p and palladium 3d regions. The copper 2p XPS spectra exhibit sharp peaks around 932 eV for metallic copper species. Significant differences in peak position and spectral intensity could be noticed in the copper 2p spectra. Addition of palladium to the copper/CeO_2 catalyst shifts the copper $2p_{3/2}$ peak position towards lower binding energy by about 0.4 eV [932.4 eV for Cu(30)Pd(0)/CeO2 and 932.0 eV for Cu(30)Pd(1)/CeO_2 catalysts], indicating that the reducibility of copper is improved by the addition of palladium. This also leads to a decrease in intensity of the copper 2p peak, suggesting that the surface dispersion of copper is improved by the addition of palladium. The XPS spectra collected in the valence band region, below 10 eV, showed that copper 3d bands are located close to the Fermi energy (EF = 0), indicating that copper is mainly involved in chemical interaction, converting carbon monoxide into CO_2. The overall spectral intensity decreased upon addition of palladium, further supporting the core level observation that copper dispersion is improved by the addition of palladium. The XPS spectra in the palladium 3d region indicate that the palladium is present mostly in the Pd0 state in the catalyst containing both copper and palladium, while a significant amount of Pd^+ and/or Pd^{2+} is present in the catalyst without copper. The presence of copper helps to retain palladium in its metallic state. Thus, the existence of a synergistic interaction between copper and palladium in the Cu-Pd bimetallic catalysts supported on CeO_2 is clearly seen from the XPS data. The existence of Cu-Pd alloy on the surface of these Cu-Pd bimetallic catalysts could be responsible for the higher catalytic activity for carbon monoxide oxidation.

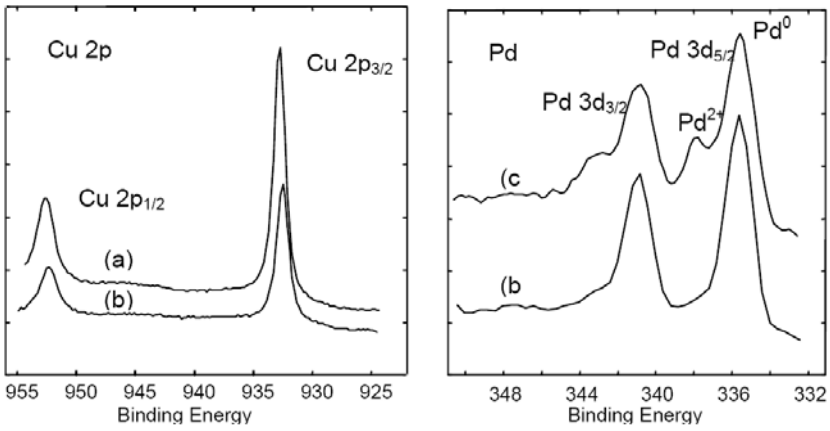

Figure 1. Copper 2p and palladium 3d XPS spectra of Cu-Pd/CeO_2 catalysts: (a) Cu(30)Pd(0)/CeO_2, (b) Cu(30)Pd(1)/CeO_2, and (c) Cu(0)Pd(1)/CeO_2.

Citations

Fox E, MH Engelhard, S Velu, and C Song. 2006a. "Surface Studies on Highly Active CeO_2 Supported CuPd Bimetallic Catalysts for the Oxygen-Assisted Water-Gas-Shift Reaction." Chapter N2 in *American Chemical Society Division Fuel Chemistry*, Vol. 50, pp. 522-523. PNNL-SA-48055, Pacific Northwest National Laboratory, Richland, Washington.

Fox E, S Velu, C Song, MH Engelhard, and Y Chin. 2006b. "The Promotional Roles of Cu and Pd in CeO_2 Supported Cu-Pd Bimetallic Catalysts for the Oxygen-Assisted Water-Gas-Shift Reaction." PNNL-SA-48298, Pacific Northwest National Laboratory, Richland, Washington. Submitted to *J. of Catalysis*

Unusual Aggregates from the Oxidation of Alkene Self-Assembled Monolayers: A Previously Unrecognized Mechanism for SAM Ozonolysis?

TM McIntire,[(a)] AS Lea,[(b)] DJ Gaspar,[(b)] N Jaitly,[(b)] Y Dubowski,[(c)] Q Li,[(a)] and BJ Finlayson-Pitts[(a)]

(a) University of California, Irvine, California
(b) W.R. Wiley Environmental Molecular Sciences Laboratory, Richland, Washington
(c) Technion-Israel Institute of Technology, Haifa, Israel

In conjunction with literature reports of polymer formation from VOC-NOx photooxidations, formation of aggregates and polymers in the atmosphere may be much more widespread than previously thought.

Airborne particles have well-documented effects on human health, visibility, and the chemical and radioactive properties of the atmosphere. Mineral dust, of which silica is commonly a major component, adsorbs organic compounds that are oxidized during transport. Oxidation is thought to convert hydrophobic coatings into polar, hydrophilic coatings that will adsorb increased amounts of water, influencing the chemical and radiative properties of the particles. However, present studies show that as oxidation proceeds, the underlying substrate is increasingly exposed. This suggests that the model of conversion of fully coated organic hydrophobic particles into a uniform, hydrophilic coating that takes up increased amounts of water may not, indeed, be the case.

In the present study, self-assembled monolayers (SAMs) of vinyl-terminated 3- and 8-carbon compounds were generated on silica substrates and reacted at room temperature with ~1 ppm gaseous O_3. A combination of atomic force microscopy (AFM), scanning electron microscopy, Auger electron spectroscopy, and time-of-flight secondary ion mass spectrometry was used to study the surface composition and morphology after oxidation.

AFM imaging of the organic-coated sample showed a relatively smooth surface, as was expected for a SAM on silicon (Figure 1). However, after oxidation with O_3, large, irregular particles with dimensions varying from tens of nanometers to several microns were observed. Furthermore, the substrate surrounding these irregular particles became depleted of carbon compared to the unreacted SAM. Long-chain C8- and C12-saturated SAMs generated on a silicon substrate and exposed to O_3 under similar conditions, however, showed no evidence of agglomeration. This highly unusual result establishes that the mechanism of ozonolysis of alkene SAMs must have a channel that is unique compared to that in the gas phase or in solution, and may involve polymerization induced by the Criegee intermediate. Oxidation at 60 percent relative humidity (RH) led to the formation of a number of smaller aggregates (as shown in Figure 1d), suggesting water intercepted the intermediate in competition with aggregate formation.

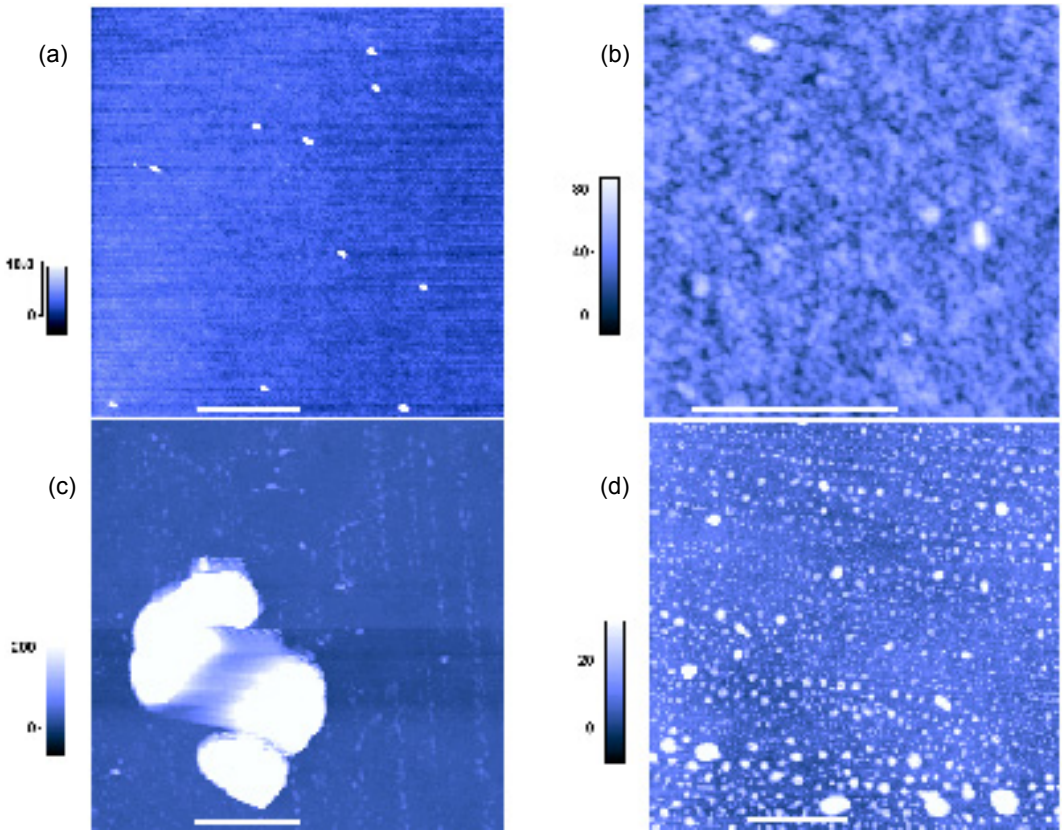

Figure 1. Intermittent contact mode AFM images of (a) a clean silcon substrate; (b) a silicon substrate on which a C8 = SAM has been deposited; (c) as in (b) but after reaction with ~10^{13} molecules cm^{-3} O_3 for 40 minutes; and (d) a C8 = SAM after ozone oxidation in presence of water at 60 percent RH. The scale bar in all images is 500 nm.

This suggests that the model of conversion of fully coated organic hydrophobic particles into a uniform, hydrophilic coating that takes up increased amounts of water may not, indeed, be the case. In fact, we have found that uptake of water, measured using transmission Fourier transform infrared spectrometry, did not increase upon oxidation of these films. Figure 2 shows the amount of surface-adsorbed water at equilibrium at various RH for an unreacted C8 = SAM, an ozone-oxidized C8 = SAM, and for comparison, an unreacted saturated C18 SAM, all on quartz substrates. The water adsorbed on the less-ordered, unreacted C8 = SAM is larger than on the well-ordered, relatively defect-free C18 SAM. This is consistent with defects and imperfections on the C8 = SAM through which water can penetrate to the substrate. However, there is no difference in water uptake before and after the oxidation of the C8 = SAM. The C3 = SAM showed similar behavior. For SAM monolayers and lower concentrations of ozone, oxidation of the SAM clearly does not lead to enhanced water uptake, which may be the result of control of water uptake by the substrate for both the reactant and for the oxidized sample.

Ozone, a toxic air pollutant for which air quality standards are set, is found in the atmosphere globally at ~30 to 40 ppb in remote regions, and at higher levels in polluted areas. The results presented here suggest that alkene SAMs may not have long-term stability in ambient air that contains even "background" amounts of ozone and that the formation of these large organic aggregates may occur more generally when alkenes are present on a surface. In addition, this oxidation leads to surface segregation of the organic material, which will change the interactions of the particle with biological systems in ways that remain to be explored. In studies of the atmospheric oxidation of organic compounds, less than 50 percent of the condensed-phase products in particles have typically been identified. Recent laboratory studies indicate that the missing material is at least in part polymeric. Whether the reactions leading to the polymers require acid catalysis is not clear. However, the present studies show that the formation of organic aggregates and/or polymeric material in airborne particles may be a quite general phenomenon that is neither restricted to reactions of secondary organics in the liquid phase nor to acid-catalyzed chemistry.

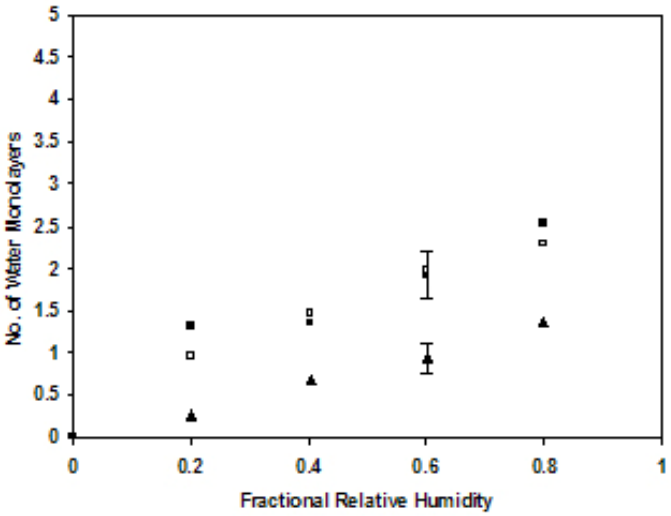

Figure 2. Water uptake as a function of RH at 295 K measured using Fourier transform infrared spectrometry. C18 SAM (▲); C8 = SAM (■); and C8 = after reaction with ~10^{13} molecules cm^{-3} O_3 for 40 min (□). Representative error bars are given for the C18 and oxidized C8 = SAMs.

Further details on this research were published by McIntire and co-workers (2005).

Citation

McIntire TM, AS Lea, DJ Gaspar, N Jaitly, Y Dubowski, Q Li, and BJ Finlayson-Pitts. 2005. "Unusual Aggregates from the Oxidation of Alkene Self-Assembled Monolayers: A Previously Unrecognized Mechanism for SAM Ozonolysis?" *Physical Chemistry Chemical Physic: PCCP* 7(20):3605-3609.

Observations of Void Formation during the Initial Oxidation of Iron Nanoparticles at Room Temperature and Their Implications

CM Wang,[(a)] DR Baer,[(a)] LE Thomas,[(b)] JE Amonette,[(b)] J Antony,[(c)] Y Qiang,[(c)] and GJM Duscher[(d,e)]

(a) W.R. Wiley Environmental Molecular Sciences Laboratory, Richland, Washington
(b) Pacific Northwest National Laboratory, Richland, Washington
(c) University of Idaho, Moscow, Idaho
(d) North Carolina State University, Raleigh, North Carolina
(e) Oak Ridge National Laboratory, Oak Ridge, Tennessee

The use of nanosized particles of iron for cleaning up contaminants in groundwater, soil, and sediments is an exciting new technology contributing to general enthusiasm about nanotechnology. However, there are many unanswered questions about the appropriate and optimal implementation of the nanoiron technology. In this research, microstructure of iron nanoparticles passivated with an iron-oxide shell were studied using high-resolution transmission electron microscopy (HRTEM) and high-angle annular dark-field (HAADF) imaging in aberration-corrected scanning transmission electron microcopy (STEM).

Phenomena related to iron oxidation are common in our daily lives. In nature, iron occurs in oxidation states that range from Fe^0 (e.g., at the core-mantle boundary) to Fe^{3+} (at the Earth's surface). A pristine surface of Fe^0 exposed to air or oxygen-including atmosphere is oxidized instantly, a process normally called initial oxidation. Oxidation behavior of iron is highly dependent on factors such as temperature, oxygen partial pressure, and time, all having an influence on the overall oxide layer thickness. High-temperature thickening of oxide layers on metal surfaces is very well understood based on experimental work and thorough theoretical derivations. Microscopically, the phase and composition of the thick oxide layer depend on the distance of the layer to the iron/oxide interface. It is normally true that a thick oxide layer has the oxidation products Fe:FeO:Fe_3O_4:Fe_2O_3.

Contrasted with the understanding of high-temperature growth of thick oxide layers, less is known about the initial oxidation process of iron and the structural nature of their product. The initial oxidation process has two features: 1) the formed oxide layer is normally just a few nanometers and 2) the growth rate is rapid. Depending on the type of migrating lattice defects, the reaction of oxide either can be at the metal-oxide interface (oxygen ions inward transport) or at the oxide-gas interface (metal ions outward transport). Under the frame-work of the Caberra-Mott theory of oxidation of metal, the initial oxidation process of iron can be described as follows: Upon initial attachment of oxygen onto the surface of metal and formation of a thin layer of oxide, the electron tunnels through the thin oxide layer and ionizes the oxygen, leading to an electrical field between the metal and the surface of the oxide layer. The electrical field will subsequently drive the outward diffusion of the ionized iron. With the Caberra-Mott model, estimates have indicated that at room temperature, it takes about 0.2 femtosecond to form an initial 1-nm thickness of oxide layer on a freshly exposed iron surface, and 40 seconds for a film of 2 nm, 40 weeks for a film of 3 nm, and 600 years for a film of 4 nm. Two issues have to be addressed related to the initial oxidation: 1) the phase formed and 2) the transporting species during this process. Intensive research

has been carried out to understand the nature of this oxidation process using single-crystal Fe(100) at ultrahigh vacuum. Based on these research efforts, a common notion that has been reached is that the oxidation layer formed during the initial oxidation is composed of γ–Fe_2O_3/Fe_3O_4.

In this highlight, we report measurements on two types of iron nanoparticles using HRTEM (Figure 1), HRTEM image simulations, HAADF imaging in aberration-corrected STEM (Figure 2), and nanometer-scale energy-dispersive spectroscopy analysis of initial oxidation products of these two types of iron particles. We found that as a result of fast cation diffusion, the oxidized iron nanoparticles have a hollow core.

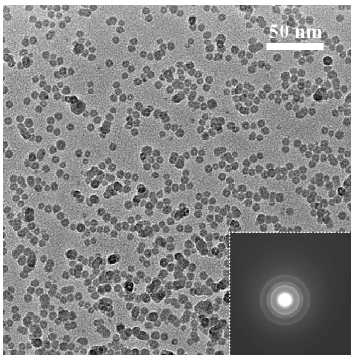

Figure 1. HRTEM images of the iron nanoparticles.

Implications of this observation on application of nanoparticles were also discussed. For particles larger than ~10 nm, it shows a core-shell structure with a thickness of the oxidized layer being around 3.5 nm. Electron diffraction and HRTEM imaging have revealed that although the core iron is a single crystal, the oxide layer is not single crystal. It is composed of small crystallites that were oriented differently. Multidomain orientations of the oxide layer indicate that the nucleation and growth of the oxide shell on the single-crystal surface of iron follow a homogenous nucleation process. The average oxide layer thickness was around 3.5 nm and showed no significant dependence on particle size. It should be noted that the oxide layer thickness depends on the time the particle was exposed to air. Furthermore, the crystallite nature of the oxide grains makes any single measurement of oxide thickness just an approximation.

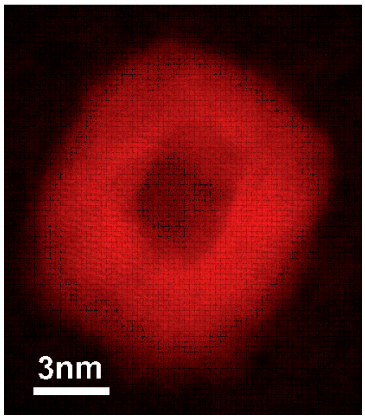

Figure 2. STEM-HAADF image of the iron nanoparticles.

We have observed that particles with a diameter of less than 8 nm are fully oxidized. A very common feature for the fully oxidized particles is the enclosure of a void at the center of the particle, as is typically shown in the STEM-HAADF image. After further scrutiny of a large number of particles, we found particles that were not fully oxidized frequently contained visible voids. For those core-shell-structure particles, each particle includes several voids spatially located at the interface between the iron core and the oxide shell. This research provides critical insights for pinpointing the physical and chemical processes that influence the behavior of iron nanoparticles for environmental remediation.

In Situ TEM Study of Morphological Evolution of $Ba(NO_3)_2$ Supported on α-Al_2O_3(0001)

CM Wang,[(a)] JH Kwak,[(b)] DH Kim,[(b)] J Szanyi,[(b)] R Sharma,[(c)] S Thevuthasan,[(a)] and CHF Peden[(b)]

(a) W.R Wiley Environmental Molecular Sciences Laboratory, Richland, Washington
(b) Pacific Northwest National Laboratory, Richland, Washington
(c) Arizona State University, Tempe, Arizona

Effective removal of pollutants such as NOx species is important to maintain and improve environmental quality. In this research, we explore the structural properties of the catalyst system based on BaO for removal of NOx species. To clarify the structural characteristics of this catalyst system during the uptake and release of NOx, instead of using traditional high-surface area γ-Al_2O_3 powders as a supporting material, we chose to support the $Ba(NO_3)_2$ particles on a single-crystal α-Al_2O_3. Based on this model system, the structural and morphological features of $Ba(NO_3)_2$ and the formation of BaO from $Ba(NO_3)_2$ during the release of NOx were systematically studied.

BaO supported on alumina has been extensively studied as a potential storage component of NOx storage/reduction catalysts. The mechanisms associated with the NOx uptake and release by this material have been examined in detail using temperature-programmed desorption, vibrational spectroscopies (e.g., infrared spectroscopy), x-ray diffraction, electron microscopy (e.g., transmission electron microscopy [TEM]), and energy-dispersive spectroscopy. We have proposed that the active NOx adsorption material consists of γ-Al_2O_3 surfaces covered by a monolayer BaO film, and with BaO nanoparticles sitting on top of this film when the BaO loading exceeds that required to form the monolayer coating (e.g., for a 20 wt% BaO/Al_2O_3 sample). When the BaO/Al_2O_3 material is synthesized by the standard "wet-impregnation" method using an aqueous solution containing dissolved $Ba(NO_3)_2$, initially large $Ba(NO_3)_2$ crystallites are formed on the alumina support after drying at low (<473 K) temperatures. A large fraction of the alumina surface remains barium-free after this procedure. Upon higher (~773 K) temperature thermal treatment required to prepare the active catalyst, these large $Ba(NO_3)_2$ crystallites decompose to form the nanosized BaO particles and monolayer BaO film. During room-temperature NO_2 uptake, both BaO-phases are transformed with the structure now consisting of nanosized (<5 nm) $Ba(NO_3)_2$ particles in addition to a monolayer nitrate phase. Heating the material to higher temperature (573 K) in the presence of NO_2 results in the sintering of the nanosized particles into larger $Ba(NO_3)_2$ crystals (<15 nm). At still higher temperatures, and even in the absence of NO_2, the average particle size of $Ba(NO_3)_2$ crystallites increases further (<32 nm), and then, as $Ba(NO_3)_2$ decomposes between 500 and 900 K, the nanosized BaO particles reform on top of the interfacial (ML) BaO layer.

To address these issues and understand the effects of crystal orientation, $Ba(NO_3)_2$ was supported on single-crystal α-Al_2O_3(0001) instead of conventional γ-Al_2O_3 powder particles. The structural and morphological evolutions of this model system, as a function of calcination temperature, were studied in detail using a combination of *ex situ* and *in situ* TEM imaging, electron diffraction, energy-dispersive spectroscopy, and Wulff shape construction.

The general morphology of $Ba(NO_3)_2$ supported on the single-crystal α-Al_2O_3 is revealed by the TEM picture shown in Figure 1. $Ba(NO_3)_2$ possesses a well-defined morphology when imaged in TEM with the substrate oriented along the [0001] zone axis. Selected area electron diffraction indicates that the triangle-shaped $Ba(NO_3)_2$ particle is a single crystal. The crystallographic orientational relationship can be written as α-Al_2O_3[0001]// $Ba(NO_3)_2$[111] and α-Al_2O_3(1-210)//$Ba(NO_3)_2$ (110). Based on Wulff shape constructions, it is clear that the $Ba(NO_3)_2$ particles supported on a single-crystal α-Al_2O_3 adopt a platelet morphology, with the surfaces and interfaces being invariably defined by 8 {111}-type planes.

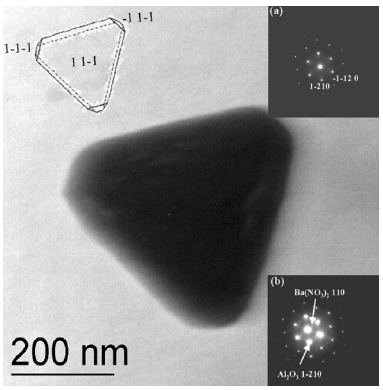

Figure 1. TEM image of the as-prepared $Ba(NO_3)_2$ particle supported on single-crystal α-Al_2O_3.

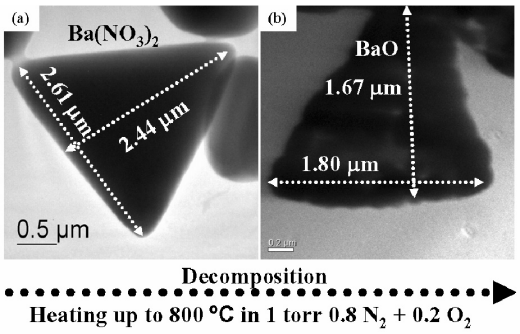

Figure 2. TEM images taken during the decomposition of the $Ba(NO_3)_2$ to form BaO particle

Decomposition of the single-crystal $Ba(NO_3)_2$ particles supported on α-Al_2O_3 was monitored in real time during the annealing of the specimen in an environmental TEM with a gas mixture of 0.8 N_2 + 0.2 O_2 at a total pressure of 1 torr. During high-temperature annealing up to 1075 K, $Ba(NO_3)_2$ decomposed to form BaO. Following the decomposition, BaO still retained an overall morphology similar to its parent single-crystal $Ba(NO_3)_2$ particle, as shown in the TEM images Figure 2. The particle appears to go through a uniform shrinkage, therefore maintaining its original morphological shape. The measured linear shrinkage of the particle following decomposition is ~31 percent, which is approximately equal to the theoretically expected linear shrinkage of 32 percent, assuming that the newly formed BaO particles are single crystals or a fully dense polycrystalline compact. Detailed TEM imaging indicates that the BaO particles are not single crystals, instead being a collection of clusters of relatively small BaO particles. Furthermore, detailed electron diffraction analysis indicates that these BaO particles show neither orientational correlation among themselves nor specific orientational relationships with respect to the α-Al_2O_3 substrate.

Thermal Lattice Expansion in Epitaxial $SrTiO_3$(100) on Si(100)

DE McCready,[(a)] Y Liang,[(b)] V Shutthanandan,[(a)] CM Wang,[(a)] and S Thevuthasan[(a)]
(a) W.R. Wiley Environmental Molecular Sciences Laboratory, Richland, Washington
(b) Motorola Labs, Tempe, Arizona

Single-crystal SrTiO3 films on silicon have many applications in the semiconductor industry, including an alternate high dielectric material and a template layer that can be used to grow single-crystal oxide films on top of it. We have investigated the film and interface stability as a function of annealing under various environments. In this highlight, we discuss the film and interfacial quality after annealing the film in air.

Crystalline metal-oxides possess a wide range of dielectric, magnetic, optical, and chemical properties. To use the potential of these materials in device applications, it is necessary and desirable to integrate them with semiconductors. Further, by combining the rich properties of oxides with mature semiconductor technology, new structures and new functionalities can be attained. Epitaxial $SrTiO_3$ on Si, realized by molecular beam epitaxy, is of importance because its structural properties permit its use as a virtual substrate for integration of various functional oxides with Si. Because lattice mismatch often dictates defectivity in epitaxial thin films, an important factor in such materials integration is thermal lattice expansion at different temperatures. By properly managing strain caused by differential thermal expansion between a substrate and a film, or by lattice mismatch, materials properties can be modified.

A $SrTiO_3$(100) epilayer (~400 Å) deposited on Si(100) was examined during this study. A thin, amorphous SiO_x layer (~20 Å) was also deliberately formed at the $SrTiO_3$/Si interface by increasing the oxygen partial pressure during later stages of deposition. The structure thus formed was subsequently cleaved into 15 mm x 15 mm specimens for *in situ* x-ray diffraction (XRD) analysis, during which the thickness of the interfacial SiO_x layer significantly increased. For comparison with the epitaxial film, a bulk $SrTiO_3$(100) single-crystal (10 mm x 10 mm) was also examined under the same non-ambient conditions.

XRD data were collected in air during both heating and cooling at the following temperature points: 25°C, 100°C, 200°C, 300°C, 400°C, 500°C, 600°C, 700°C, 750°C, 850°C, 900°C, 950°C, and 1000°C. In the case of the thin-film specimens, the Si (400) peak was also used as an internal reference point. For the bulk $SrTiO_3$ crystal, the position data were externally calibrated. Separate thin-film specimens were subjected to a single non-ambient cycle and two thermal cycles executed in series; the bulk $SrTiO_3$ crystal was examined over one non-ambient cycle.

Figure 1 illustrates the corrected thermal expansion curves for an epitaxial thin-film specimen subjected to two non-ambient cycles executed in series. During first-cycle heating, the coefficient of thermal expansion (CTE) for the $SrTiO_3$ epilayer was ~6.8 x 10^{-5} $°C^{-1}$; during cooling, the CTE decreased to ~6. 8 x 10^{-5} $°C^{-1}$. In addition, the out-of-plane $SrTiO_3$ lattice parameter relaxed ~0.2 percent after completion of the first cycle. During the second thermal cycle, the out-of-plane CTE further decreased to ~5.48 x 10^{-5} $°C^{-1}$ with no additional relaxation. For comparison, the corrected CTE value for the bulk crystal was ~3.98 x 10^{-5} $°C^{-1}$ (CTE ~3.28 x 10^{-5} $°C^{-1}$ for $SrTiO_3$ in powder form).

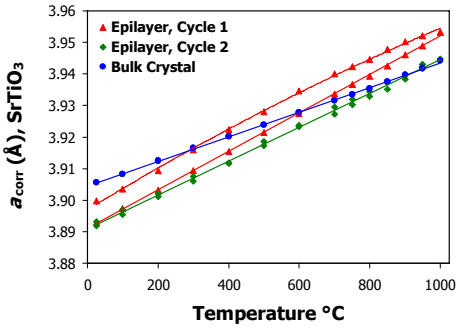

Figure 1. Thermal expansion curves for epitaxial and bulk $SrTiO_3$(100).

Although not directly observed by XRD, results from Rutherford backscattering and channeling (RBS/C) and transmission electron microscopy (TEM) showed that heating the $SrTiO_3$(100) epilayer in air promoted growth of a thick (~1000 Å) layer of amorphous SiO_x at the STO/Si interface. In spite of the formation of this non-templating surface, the $SrTiO_3$ layer retained its epitaxial form. RBS/C also indicated that the crystalline quality of the $SrTiO_3$ film increased after one thermal cycle (χ_{min} = 1.2 percent), but decreased slightly after two cycles (χ_{min} = 6.8 percent). Similarly, dark-field TEM cross sections showed fewer domain boundaries and shorter-range stress fields in the specimen annealed for one thermal cycle (Figure 2).

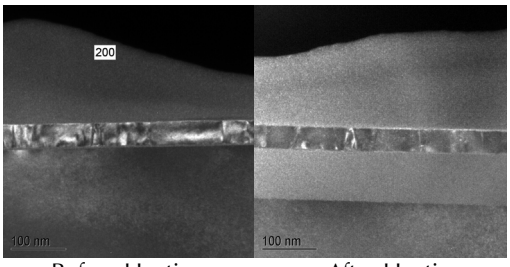

Before Heating After Heating

Figure 2. Dark-field TEM micrographs.

Comparison of the experimental CTE values for the epitaxial $SrTiO_3$(100) film, the bulk $SrTiO_3$(100) single-crystal, and data found in the literature for $SrTiO_3$ in powder form, shows that the rate of thermal expansion in epitaxial $SrTiO_3$ in the out-of-plane direction is approximately 1.5 to 2.0 times the bulk value. This effect is largely attributed to the two-dimensional, in-plane confinement of the film. The CTE value for epitaxial $SrTiO_3$ is highest during initial heating then decreases slightly during cooling and subsequent thermal cycling. Such behavior is likely the result of two effects. First, the amorphous SiO_x layer between $SrTiO_3$ and Si can deform quite easily at high temperature, which would partially relieve the lateral constraint on the $SrTiO_3$ film and facilitate its lateral (in-plane) lattice expansion at high temperature. Second, annealing of point defects in the $SrTiO_3$ film (e.g., oxygen vacancies introduced during growth) led to improvements in its crystallinity, which in turn further modified its expansion.

Aerosol Composition and Source Apportionment in the Mexico City Metropolitan Area with PIXE/PESA/STIM and Multivariate Analysis

KS Johnson,[(a)] B de Foy,[(a)] B Zuberi,[(a)] LT Molina,[(a)] MJ Molina,[(a)] Y Xie,[(b)] A. Laskin,[(c)] and V Shutthanandan[(c)]

(a) Massachusetts Institute of Technology, Cambridge, Massachusetts
(b) Pacific Northwest National Laboratory, Richland, Washington
(c) William R. Wiley Environmental Molecular Sciences Laboratory,Richland, Washington

Aerosols play an important role in the atmosphere but are poorly characterized, particularly in urban areas like the Mexico City Metropolitan Area (MCMA). The chemical composition of urban particles must be known to assess their effects on the environment, and specific particulate emissions sources should be identified to establish effective pollution controls.

In this project, samples of particulate matter ≤2.5 μm ($PM_{2.5}$) were collected during the MCMA-2003 Field Campaign (from April 3 through May 4) for elemental and multivariate analyses. Proton-induced x-ray emission (PIXE), proton-elastic scattering analysis (PESA), and scanning transmission ion microscopy (STIM) were done to determine concentrations of 19 elements from Na to Pb, hydrogen, and total ion mass, respectively. Positive matrix factorization (PMF) was applied to PIXE and PESA data to help identify particulate emissions sources in the MCMA.

PMF analysis of PIXE and PESA data identified eight factors in Stage A, seven in Stage B, and four in Stage C. Figure 1 shows the composition elements and relative contribution for each size category. Among PIXE elements, sulfur was highest in concentration; it was surpassed only by silicon in Stage C. Single-particle analysis and aerosol mass spectrometry measurements during MCMA-2003 confirm that sulfur was a major component of $PM_{2.5}$ and suggest that it was present as ammonium sulfate during the majority of the campaign. The relatively high minimum concentration of sulfur in $PM_{2.5}$ (0.826 μg/m^3, sum of stages A, B, and C) indicates a consistent background of particulate sulfate, most likely formed by aqueous phase SO_2 oxidation on a regional, rather than local scale. Heavy metals appearing in several of the factors suggest industrial emissions. Copper comprises a separate factor in

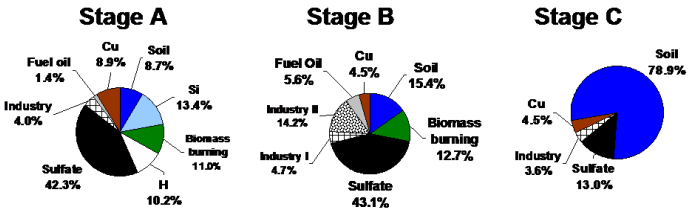

Factor	Elements	Factor	Elements	Factor	Elements
Sulfate	S, P	Sulfate	S	Sulfate, Fuel oil	S, V, Ni
Fuel oil	V, Ni	Fuel oil	V, Ni		
Soil	Al, Mg, Si, Ca, Ti, Mn, Fe	Soil	Al, Si, Mg, Ca, Ti, K, Na, Mn, Fe, Sn	Soil	Mg, Al, Si, Ca, Ti, Mn, Fe
Biomass burning	K, Cl, Br, Sn	Biomass burning	K, Cl, H, Br, Sn		
Industry	Zn, As, Mn, Na	Industry I	Zn, As, Mn, Na	Industry	Zn, Mn
		Industry II	Mn, Zn, Fe, P, H		
Cu	Cu	Cu	Cu	Cu	Cu
Si	Si				
Hydrogen	H, Cl, K, Sn				

Figure 1. PMF factors for stages A, B, and C.

each size range (Figure 1), perhaps signifying a particular sector or source. The other factors marked by zinc, manganese, sodium, and arsenic may be a mix of various industrial activities.

The industrial factors reflect individual emissions events rather than consistent patterns. On April 9, concentrations of sodium, manganese, arsenic, and zinc rose sharply during the early morning (from 0:00 to 6:00 a.m.), as shown in Figure 2a. The sudden increase is clearly distinguishable above the low background levels measured during most of the campaign. In order to ascertain the likely direction of the plume, simulations of particle back-trajectories were performed. The paths for particle tracers arriving at the Technical University of Tecamac (CENICA) at 6:00 a.m. (Figure 2b) shows that the air masses during this time came from north/northeast of MCMA, which is among the more industrial sections of the city. Similarly, a sharp increase in fuel oil components vanadium and nickel was observed for April 10 (Figure 3a). The vanadium/nickel ratio of 5.25 is comparable to that found in a study that sourced the metals directly to power plant emissions in the United States. The maximum vanadium and nickel values coincided with a large SO_2 plume to strongly suggest an anthropogenic, rather than volcanic, emissions source. Particle back-trajectory simulations follow a north/northwest source direction (Figure 3b) with paths over the location of the Tula power plant located approximately 80 km from CENICA.

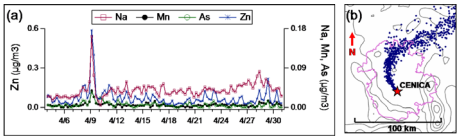

Figure 2. Industrial emissions on April 9. (a) Time series of industrial emissions markers sodium, manganese, arsenic, and zinc from PIXE analysis. (b) Particle cloud back trajectory from CENICA.

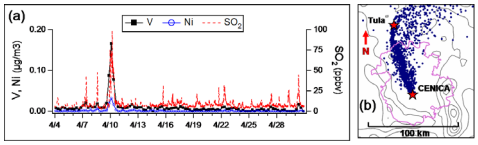

Figure 3. Emissions on April 10. (a) Time series of fuel oil components vanadium and nickel shown with SO_2 measured at CENICA. (b) Particle back trajectory indicating a north/northwest emissions source.

Factors composed of potassium, chlorine, tin, bromine, and hydrogen indicate biomass burning where hydrogen is a tracer for organic compounds. Potassium salts, such as KCl, are commonly found in particulate emissions from burning vegetation. The time series for potassium, chlorine, and organic hydrogen are shown in Figure 4; organic hydrogen is calculated as the amount in excess of ammonium sulfate ($[H]_{total} - 0.25[S]$) assuming loss of volatile compounds (nitrates, water) prior to PIXE/PESA analysis. The most volatile organics are also assumed to have been lost in vacuum.

Soil factors represented by common earth elements were identified in each of the three particle-size categories. Figures 5a-c show that the concentrations of soil components (silicon, calcium, aluminum, iron, magnesium, and titanium) clearly track one another

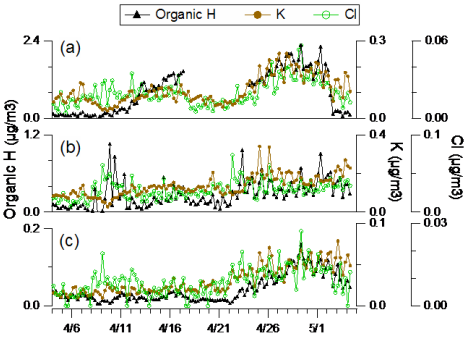

Figure 4. Elemental markers of biomass burning, potassium, chlorine, and organic hydrogen for (a) Stage A, (b) Stage B, and (c) Stage C.

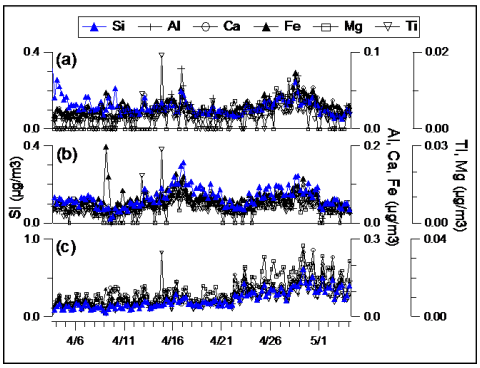

Figure 5. Time series of soil factors (a) Stage A, 1.15 to 2.5 µm; (b) Stage B, 0.34 to 1.15 µm; and (c) Stage C, 0.07-0.34 µm.

throughout the campaign. Soil particles followed a diurnal pattern with the highest concentrations in the morning when winds were typically calm and mixing heights were low. An anti-correlation between fine soil particles and wind speed may be explained through dilution effects.

Synthesis and Characterization of Cobalt Silicide Films on Silicon

CT Joensson,[(a)] IA Maximov,[(a)] HJ Whitlow,[(b)] V Shutthanandan,[(c)] L Saraf,[(c)] DE McCready,[(c)] BW Arey,[(c)] Y Zhang,[(c)] and S Thevuthasan[(c)]

(a) Lund University, Lund, Sweden

(b) University of Jyväskyla, Jyväskyla, Finland

(c) William R. Wiley Environmental Molecular Sciences Laboratory, Richland, Washington

Cobalt silicide is widely used for metallization of very large-scale integrated electronic circuits as interconnects, ohmic contacts, Schottky barriers, and electrodes because of its unique properties for a good metallization to silicon, namely low resistivity, good mechanical properties, high-temperature chemical stability, and formation of uniform films on silicon with well-defined and reproducible interface. In this project, we investigated the deposition and charcaterization of cobalt silicide films on silicon.

A cobalt film was deposited on high-quality, single-crystal Si(100) substrate using radio frequency magnetron sputtering for 3 hours with an argon gas pressure of 4 x 10^{-3} Torr. The wafer was then carefully cut into smaller pieces that were used in various characterizations using Rutherford backscattering spectrometry (RBS), nuclear reaction analysis (NRA), x-ray diffraction (XRD), scanning electron microscopy (SEM), and an optical interferometer. Sample annealing was carried out in a vacuum chamber with a base pressure of 2.0 x 10^{-8} Torr and annealed at 600, 700, 800 and 900°C for about 10 minutes. The as-deposited and annealed samples were also characterized by the above-mentioned techniques. The optical interferometer study of the as-deposited samples indicated that the film thickness varies between 200 to 400 nm. Although these results show that the film thickness is not uniform, the film was somewhat uniform in the center region of the wafer. The areal atomic density measured by RBS on same samples showed that the average thickness was 3 x 10^{18} atoms/cm^2; this is consistent with the results obtained from the interferometer measurements. The XRD measurements also confirmed the formation of cobalt film on the silicon substrates.

The absence of oxygen along with highly stoichiometric cobalt silicide is important for its applications. However, because there was enough oxygen in the high-pressure background in the sputtering chamber, all the as-grown films showed oxygen at the silicon/cobalt interface and on the cobalt film surface. The RBS spectrum from as-grown sample (not shown) is similar to the spectrum that is shown in Figure 1(a) and annealing up to 600°C did not make that much difference. However, annealing at 700°C initiated cobalt diffusion into silicon and this is clearly visible in the RBS spectrum in Figure 1(a). The

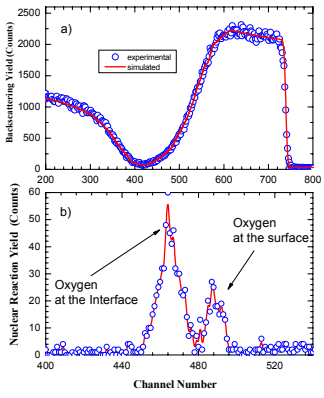

Figure 1. a) RBS spectrum of the sample annealed at 700°C. b) NRA spectrum for the sample annealed at 700°C. It reveals the presence of interfacial oxygen (channel 460) and surface oxygen (channel 87).

total oxygen content was measured by the $^{16}O(d,p_1)^{17}O$ nuclear reaction; these results for the sample annealed at 700°C are presented in Figure 1(b). The total content of oxygen remains the same within the experimental uncertainties in all the as-grown and annealed samples up to 700°C. The first peak, around 465 channel number, is from the oxygen content at the interface and the second peak, around 487 channel number, is from the oxygen at/on the surface. These results clearly demonstrate that the film surface and the interface were oxidized during the growth.

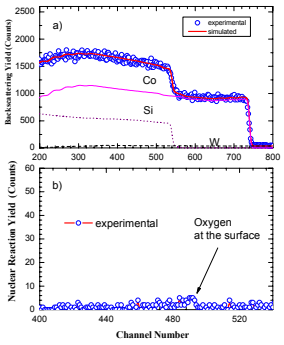

Figure 2. a) RBS spectrum of the sample annealed at 800°C. It reveals a well developed $CoSi_2$ layer. b) NRA spectrum for the sample annealed at 800°C. It reveals a significant reduction of the oxygen level.

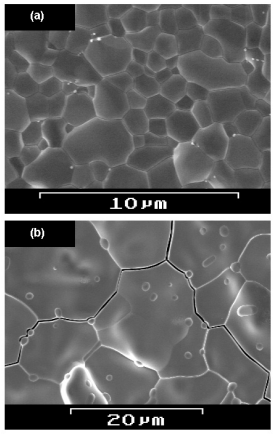

Figure 3. (a) SEM image from the sample annealed at 800°C. (b) SEM image from another part of the surface where the grains are about 10 to 30 μm.

In Figure 2, the RBS spectrum from the sample annealed at 800°C is presented along with the secondary ion mass spectrometry nuclear reaction analysis (SIM/NRA) simulated spectrum. These results clearly demonstrate that the cobalt silicide was formed during this heating. From the SIM/NRA simulations it was found that the cobalt and silicon concentrations were close to 33 percent and 67 percent, which indicates that the film stoichiometry is close to $CoSi_2$. The simulations also demonstrate that the silicide layer appears to be consisting of 8 x 10^{18} atoms (cobalt + silicon)/cm^2. Although the majority of the phase appeared to be $CoSi_2$, it is possible that some cobalt atoms are bonded to one silicon atom in a form of CoSi. This is consistent with the XRD results (not shown). In addition, the RBS spectrum results suggest that no significant amount of oxygen existed either at the interface or on the surface. Although these results are more or less consistent with the NRA results shown in Figure 2(b), a trace amount of oxygen can be seen in the surface region of the sample. This might result from exposure of the sample to air during transfer from the annealing chamber to the chamber where the NRA experiments were carried out. These results clearly show that annealing at around 800°C promoted the evaporation of SiOx interface, and as a result, cobalt could react with Si and could have formed cobalt silicide during annealing. This is not surprising because native oxide on Si can be removed by annealing the sample in vacuum around 800 to 900°C. After the RBS and NRA analysis, this sample was characterized by SEM. As shown in Figures 3(a) and (b), the SEM micrographs reveal that the cobalt silicide film consists of crystal grains of varying sizes. The size distribution of these grains varies significantly in the surface region, ranging from 1 to 3 μm in one region [Figure 3(a)] to 10 to 30 μm in another region [Figure 3(b)], possibly because of inhomogeneous annealing of the sample. Some intragranular thermal cracks and precipitates can also be seen in the micrographs. Annealing at 800 and 900°C provides similar results.

Fundamental Studies of Candidate Ferromagnetic Oxide Semiconductors for Spintronics

TC Kaspar,[a] TC Droubay,[a] SM Heald,[a] CM Wang,[b] DR Gamelin,[c] DJ Bryan,[c] AJ Kellock,[d] MF Toney,[e] DE McCready,[b] CH Ahn,[f] X Hong,[f] V Shutthanadan,[b] S Thevuthasan,[b] AS Lea,[b] and SA Chambers[a]

(a) Pacific Northwest National Laboratory, Richland, Washington
(b) W.R. Wiley Environmental Molecular Sciences Laboratory, Richland, Washington
(c) The University of Washington, Seattle, Washington
(d) IBM Almaden Research Center, San Jose, California
(e) Stanford Synchrotron Radiation Laboratory, Stanford, California
(f) Yale University, New Haven, Connecticut

Continued progress in spintronics requires the discovery of ferromagnetic semiconductors in which magnetically aligned dopant spins couple to the band structure of the host lattice, resulting in spin polarization of free carriers. We have synthesized crystalline films and determined the properties of a number of magnetically doped transition metal oxides to probe the structure-magnetic/electronic function relationships is this deceptively complex class of materials. One of the prototypical systems under study around the world is doped TiO_2 anatase. We show, through painstaking growth and characterization, that magnetic ordering in these materials is driven by structural defects and is not an intrinsic property.

The theoretical prediction and observation of room-temperature ferromagnetism in doped transition metal oxides is one of the most interesting and provocative scientific developments of the early 21st century. One of the 125 critical unanswered scientific questions recently posed in *Science* magazine asks, "Is it possible to create magnetic semiconductors that work at room temperature?" A ferromagnetic semiconductor typically consists of a non-magnetic semiconductor doped with a few to several atomic percent of some open-shell transitional metal dopant. A true ferromagnetic semiconductor is one in which the magnetic dopant spins retain remanent alignment under the influence of spin-polarized free carriers, which are introduced by either the magnetic dopant or by some secondary electronic dopant. It is critical to distinguish true ferromagnetic semiconductors from those that merely show magnetic hysteresis. The latter can result from other physical causes, such as phase separation, that lead to magnetic secondary phase formation. Such materials do not consist of spatially distributed localized moments that can impart spin polarization to carriers in a gateable fashion. Nonmagnetic semiconductors with embedded secondary-phase ferromagnetic particles may exhibit anomalous magnetic and magnetotransport properties. However, any spin polarization in the majority carrier band is not controllable in a way that is useful in spin-based devices, at least as the latter have been conceived thus far. Thus, such materials might be referred to as "semiconductors that are ferromagnetic," as opposed to "true ferromagnetic semiconductors." Failing to differentiate between these two classes of materials has led to much confusion in the field.

Our approach to discovering new diluted magnetic semiconductors has been to combine careful epitaxial growth, detailed material characterization, transport and magnetic measurements, and theory to determine structure-function relationships. We have investigated, among other systems, cobalt- and chromium-doped TiO_2 anatase grown

epitaxially on $LaAlO_3$ and $SrTiO_3(001)$. These materials were among the first found to exhibit ferromagnetism at and above room temperature, and until recently, several in the oxide materials science community believed that they were *bona fide* DMSs. The critically important question is whether the magnetic ordering results from the magnetic dopant spins interacting with free carriers, magnetic polarons resulting from dopant substitution, or whether it results from some other physical cause. By refining the epitaxial growth to the point that the material is structurally near perfect, we have been able to answer this important question.

We have found that ferromagnetism in both cobalt- and chromium-doped TiO_2 anatase results from structural defects associated with multiple crystallite orientations. All our molecular beam epitaxy-grown films are nominally single-crystal anatase with $(001)_{film}||(001)_{sub}$ and $[100]_{film}||[100]_{sub}$. Moreover, the dopant distribution can be made to be random, resulting in the materials being dilute magnetic systems. However, we have found that the saturation magnetization scales with the mosaic spread, which is a measure of the distribution of crystallite orientations throughout the film. We show in Figure 1(a) the high-resolution x-ray diffraction (XRD) $(004)_{anatase}$ reflection from several $Cr_{\sim 0.05}Ti_{\sim 0.95}O_2$ films.

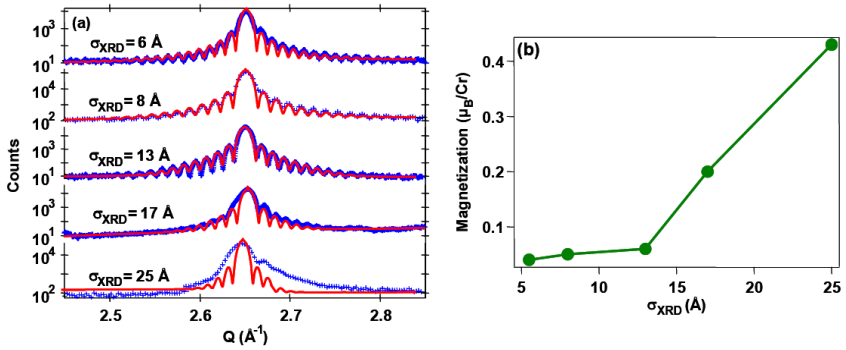

Figure 2. Measured (blue) and calculated (red) $(004)_{anatase}$ reflections (a), and saturation moment *vs* σ_{XRD} (b) for several $Cr:TiO_2$ films grown on $LaAlO_3(001)$.

Keissig fringes, which are a measure of the crystalline perfection over the finite depth of the film, are visible on each side of the Bragg peak. Model fits based on equation (1) are also shown in Figure 2(a).

$$IQ = \frac{\sin^2(QL/2)}{\sin^2(Qd/2)}\exp(-|Q - 2\pi/d|\sigma_{XRD} \qquad (1)$$

The physical significance of σ_{XRD} is that it represents the overall roughness and crystalline imperfection of each film. Q is the scattering vector, and L and d are the film thickness and layer spacing, respectively. Going down the series, the Keissig fringes become weaker as the crystalline order degrades, and σ_{XRD} increases accordingly. Figure 2(b) shows the room-temperature saturation magnetization in the plane of the film as a function of σ_{XRD}. The increase in magnetization with decreasing crystallinity strongly suggests that defects created at the interfaces of nanocrystallites activate the ferromagnetism. This result is consistent with analogous studies of spin-coated films of $Cr:TiO_2$ nanoparticles grown by direct chemical methods. Here, the nanoparticles are structurally perfect and paramagnetic as grown, but become ferromagnetic upon spin coating and partial sintering at elevated temperatures.

Formation and Decomposition of $BaAl_2O_4$ on BaO/Al_2O_3

JH Kwak,[(a)] DH Kim, [(a)] SD Burton, [(a)] T Szailer, [(a)] J Szanyi, [(a)] and CHF Peden[(a)]
(a) Pacific Northwest National Laboratory, Richland, Washington

Fundamental chemical issues that could be relevant to new catalytic conversion technologies for "lean"-combustion diesel engines were investigated in this project.

The control of NO_x (NO and NO_2) emission from combustion processes, including vehicle engines, remains a challenge, particularly for systems operating at high air-to-fuel ratios (so-called "lean" combustion). The current "three-way," precious-metal-based catalytic converters are unable to selectively reduce NO_x with reductants in the presence of excess oxygen. In the last few years, worldwide environmental regulations regarding NO_x emissions from diesel engines (inherently operated in a "lean" condition) have become significantly more stringent, resulting in considerable research efforts to reduce NO_x under the highly oxidizing engine operation conditions. In the mid 1990s, alkaline and alkaline earth oxide-based NO_x storage/reduction catalysts (especially $Pt\text{-}Rh/BaO/Al_2O_3$) were developed by Toyota, and had shown promising activities for lean-NO_x reduction. Although there are extensive studies about the NO_x storage/reduction mechanism, a fundamental question still remains concerning what barium phases are most favorable for storing and releasing NO_x. It is reported that BaO and Al_2O_3 react at high temperature (>800°C) to form an aluminate phase, $BaAl_2O_4$. We recently reported the effects of thermal aging and H_2O treatment on the $BaAl_2O_4$ formation and decomposition on BaO/Al_2O_3.

Here we report the results of a solid-state ^{27}Al magic-angle-spinning nuclear magnetic resonance (NMR) investigation on the formation and decomposition of $BaAl_2O_4$ phase in the $BaO(x)/Al_2O_3$ (x = 8 and 20 wt%) system. Interestingly, the 8 wt% BaO/Al_2O_3 sample did not show any detectable changes upon high-temperature thermal treatment, while a significant amount of $BaAl_2O_4$ was formed on the 20 wt% BaO/Al_2O_3 sample under identical reaction conditions (1000°C for 10 hours).

The results of this solid-state ^{27}Al-NMR study clearly show the difference of $BaAl_2O_4$ formation in BaO/Al_2O_3 systems with different BaO loadings. Figures 1(a) and (b) show the solid-state ^{27}Al-(NMR) spectra of Al_2O_3 and $BaAl_2O_4$ standard samples (after treatment at 1000°C for 10 hours). The spectrum of the Al_2O_3 sample in Figure 1(a) contains two peaks at ~0 ppm and at ~60 ppm chemical shifts, which are typically assigned to Al^{3+} in octahedral and tetrahedral coordination environments, respectively. The spectrum of the $BaAl_2O_4$ sample exhibits a peak at 70 ppm, which has been assigned to aluminum species with tetragonal coordination in the $BaAl_2O_4$ phase. Figures 1(c) and (d) show the ^{27}Al-NMR spectra of 8 and 20 wt% BaO/Al_2O_3 samples after calcination at 1000°C for 10 hours. The spectrum of the 20 wt% BaO/Al_2O_3 sample clearly shows the formation of a significant amount of $BaAl_2O_4$, while that of the 8 wt% BaO/Al_2O_3 sample was basically the same as the original alumina. When the high-temperature-calcined 20 wt% BaO/Al_2O_3 sample was treated with water at room temperature [Figure 1(e)], the alumina phase reformed and the $BaAl_2O_4$ phase totally disappeared. A new peak, assigned to $Al(OH)_4^-$, appeared at 79 ppm chemical shift. These $Al(OH)_4^-$ species completely disappear and convert to Al_2O_3 species

upon drying the sample in an oven at 120°C, as shown in Figure 1(f). These results clearly demonstrate the water-induced decomposition of the $BaAl_2O_4$ phase in high-temperature-calcined 20 wt% BaO/Al_2O_3. These results imply the practical importance of regenerating the thermally deactivated lean NO_x trap materials in real systems by water treatment.

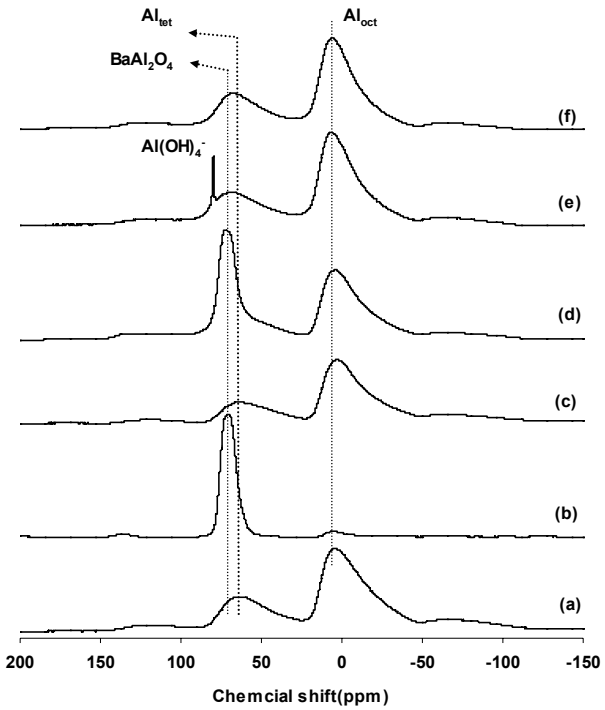

Figure 1. Solid-state ^{27}Al-NMR spectra change: (a) alumina, (b) $BaAl_2O_4$ (1000°C for 10 hours), (c) 8% BaO/Al_2O_3 (1000°C for 10 hours), (d) 20% BaO/Al_2O_3 (1000°C for 10 hours), (e) H_2O treatment of (d), (f) 120°C dry for (e).

Functional Nanomaterials for Biosensing Applications

Y Lin,[(a)] G Liu,[(a)] J Wang,[(a)] CJ Zhong,[(b)] MH Engelhard,[(a)] and CM Wang[(a)]
(a) Pacific Northwest National Laboratory, Richland, Washington
(b) State University of New York at Binghamton, Binghamton, New York

The research undertaken in this project focused on the development of functional nanomaterials for sensing applications in biological systems.

Biosensors Based on Layer-By-Layer Assembly of Enzymes on Carbon Nanotubes. Carbon nanotubes (CNTs) have emerged as a new class of nanomaterials that is receiving considerable interest because of their unique structure and mechanical and electronic properties. One promising application of CNTs involves their use in the construction of chemical sensors and biosensors (Wang et al. 2005; Liu and Lin 2006a, b). In the research described in this highlight, highly sensitive amperometric biosensors for glucose, choline, organophosphate pesticides, and nerve agents based on self-assembly of enzymes on a CNT electrode have been developed.

The glucose biosensor was fabricated based on immobilizing glucose oxidase (GOx) on the negatively charged CNT surface by alternatively assembling a cationic polydiallyldimethyl-ammonium chloride (PDDA) layer and a GOx layer (Figure 1).

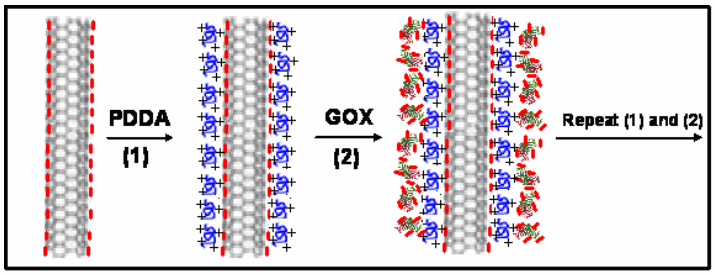

Figure 1. Schematics of layer-by-layer electrostatic self-assembly of protein-polyion on a carbon nanotube template.

The unique sandwich-like layer structure (PDDA/GOx/PDDA/CNT) formed by self-assembling provides a favorable microenvironment to maintain the bioactivity of GOx while preventing enzyme molecule leakage. The excellent electrocatalytic activity toward H_2O_2 of the fabricated PDDA/GOx/ PDDA/CNT electrode indicated that the polyelectrolyte-protein multilayer does not affect the electrocatalytic properties of CNT, enabling sensitive determination of glucose. Flow injection amperometric detection of glucose is carried out in 0.05 M phosphate buffer solution with a wide linear response range of 15 μM to 6 mM and a detection limit of 7 μM. The PDDA/GOx/PDDA/CNT/GC biosensor showed excellent properties for the sensitive determination of glucose with good reproducibility, remarkable stability, and freedom of interference from other co-existing electroactive species.

The biosensor for organophosphate pesticides and nerve agents was fabricated based on self-assembly of acetylcholinesterase (AChE) on a CNT electrode using the same layer-by-layer approach described above. The electrocatalytic activity of CNT leads to a greatly

improved electrochemical detection of the enzymatically generated thiocholine product, including a low oxidation overpotential (+150 mV), higher sensitivity, and stability. The sensor performance, including inhibition time and regeneration conditions, was optimized with respect to operating conditions. Under optimal conditions, the biosensor was used to measure as low as 0.4 pM paraoxon with a 6-minute inhibition time. A choline biosensor was also fabricated based on layer-by-layer assembly of a bienzyme of choline oxidase (ChO) and horseradish peroxidase (HRP) onto a CNT electrode. Because of the electrocatalytic effect of CNTs, the measurement of faradic responses resulting from enzymatic reactions has been realized at low potential with a good sensitivity. We found that the biosensor based on a bienzyme (i.e., ChO/HRP/CNT) electrode is more sensitive than a biosensor based on one enzyme (i.e., the ChO/CNT) for choline detection.

Monodispersed Core-Shell Fe_3O_4@Au Nanoparticles. The ability to synthesize and assemble monodispersed core-shell nanoparticles is important for exploring the unique properties of nanoscale core, shell, or their combinations in technological applications. This work describes findings of an investigation of the synthesis and assembly of core (Fe_3O_4)-shell (Au) nanoparticles with high monodispersity. Fe_3O_4 nanoparticles of selected sizes were used as seeding materials for the reduction of gold precursors to produce gold-coated Fe_3O_4 nanoparticles (Fe_3O_4@Au) (Figure 2).

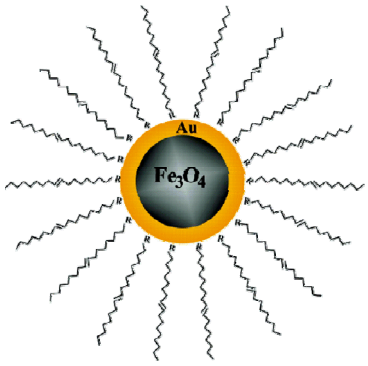

Figure 2. Illustration of the core-shell Fe_3O_4@Au nanoparticle with an outmost organic shell encapsulation (R = $-CO_2H$ or $-NH_2$).

Our approach differs from many nanoparticle-to-nanoparticle-based approaches by the ability to control a combination of thermally activated desorption of the capping layer, deposition of Au on the exposed Fe_3O_4 surface, and subsequent re-encapsulation of the Au surface by the capping agent. In addition to transmission electron microscope detection of the change in particle size, spectro-photometric observation of the change in SP optical band, x-ray diffraction detection of the change in diffraction peaks, x-ray photoelectron spectroscopy analysis of the surface compositions, and superconducting quantum interference device measurement of the magnetic properties, the formation of the core-shell morphology was further confirmed by direct current plasma-auger electron spectroscopy analysis of the core-shell composition in terms of gold and iron in molecularly mediated thin-film assembly of Fe_3O_4@Au nanoparticles. The study of the thin-film assembly of the

core-shell nanoparticles via interfacial molecular linking chemistry has provided new insights into the controllability of size monodispersity and surface properties of the core-shell nanoparticles toward nanocomposite materials, which could find broad applications in biosensor development.

Citations

Liu G and Y Lin. 2006a. "Biosensor Based on Self-Assembling Acetylcholinesterase on Carbon Nanotubes for Flow Injection/Amperometric Detection of Organophosphate Pesticides and Nerve Agents." *Analytical Chemistry* 78(3):835-843.

Liu G and Y Lin. 2006b. "Amperometric Glucose Biosensor Based on Self-Assembling Glucose Oxidase on Carbon Nanotubes." *Electrochemistry Communications* 8:251-256.

Wang L, J Luo, MM Maye, Q Fan, R Qiang, MH Engelhard, CM Wang, Y Lin, and C Zhong. 2005. "Iron Oxide-Gold Core-Shell Nanoparticles and Thin-Film Assembly." *Journal of Materials Chemistry* 15(18):1821-1832.

On the NO_x Storage Capacity and Thermal Aging of $BaO/\theta\text{-}Al_2O_3/NiAl(100)$ Model Catalyst

E Ozensoy,[(a)] CHF Peden,[(a)] and J Szanyi[(a)]
(a) Pacific Northwest National Laboratory, Richland, Washington

Because of their outstanding catalytic performance for NO_x reduction under the highly oxidizing conditions (i.e., "lean"-operating conditions) typical for diesel engine operation, BaO and transition metal-based NO_x storage/reduction (NSR) catalysts have recently become an important alternative to the traditional selective catalytic reduction (SCR) approach.

Diesel engines are typically operated at high air-to-fuel ratios (A/F = 25/1; weight/weight), which provides an improvement in the fuel efficiency up to 35 percent when compared to gasoline engines in which lower air-to-fuel ratios (A/F = 14.5) are used. It should be noted that conventional (paladium or platinum-ruthenium)/γ-Al_2O_3-based three-way catalysts, which are commonly employed in automotive catalysts to reduce NO_x emissions, severely fail under highly oxidizing (lean) conditions (i.e., A/F > 18) (Epling et al. 2004).

The first commercial NSR catalyst was introduced in 1994 by Toyota Motor Company (Epling et al. 2004). For that catalyst, a platinum/BaO/γ-Al_2O_3-based formulation was used. In this formulation, the platinum component provides NO oxidation and NO_x reduction (redox) capabilities whereas the primary role of BaO sites is NO_x storage in the form of $Ba(NO_3)_2$. The γ-Al_2O_3 support material enables dispersion of the active sites over a large surface area, and facilitates the reactant transport between the active sites on the catalyst via surface diffusion. NSR catalysts are typically operated in two alternating cycles. In the so-called "storage cycle," exhaust gas composition is abundant in oxygen (i.e., the conditions are "lean"). Under these conditions, NO(g), which is the major NO_x component in the untreated exhaust gas composition, is readily oxidized to NO_2 on the platinum sites. Next, NO_2 migrates onto the BaO storage sites via gas phase adsorption and/or surface diffusion and is eventually converted to $Ba(NO_3)_2$. After the active barium-containing phase is saturated with nitrates, the "reduction cycle" is started by quickly switching to an exhaust gas phase composition that is abundant in fuel, hydrocarbons (HC), carbon monoxide, and hydrogen (i.e., the conditions are "rich"). During the reduction cycle, the barium component releases the stored nitrates in the form of NO_2, NO, and oxygen, which is subsequently transferred onto the platinum sites to be reduced by HC, carbon monoxide, and hydrogen, resulting in the regeneration of the active BaO storage component (Epling et al. 2004).

Although a number of studies on the high-surface-area NSR catalysts have been undertaken, only a limited number of surface-science studies have addressed the fundamental chemical and physical phenomena taking place on NSR catalyst surfaces, which ultimately dictate the reaction mechanisms and the catalytic performance of these systems. To address this issue, we recently employed a systematic approach using model catalysts to study some of the key surface-science phenomena relevant to the NSR systems. We used a bottom-up synthetic strategy to prepare a model NO_x storage catalyst (Figure 1). This was achieved by using an ordered θ-Al_2O_3 ultrathin film, grown on a NiAl(100) bimetallic alloy substrate, mimicking

the high-surface-area alumina counterpart. The spectroscopic characteristics of the alumina support material and its interaction with H_2O (Ozensoy et al. 2005a), NO_2 (Ozensoy et al. 2005b), and H_2O+NO_2 in the absence of the active barium-containing phase were investigated in previous reports. Next, deposition, oxidation, and growth of the barium phase on the θ-Al_2O_3/NiAl(100) substrate were studied via different preparation protocols to obtain a model NO_x storage catalyst in the form of BaO/ θ-Al_2O_3/NiAl(100).

As a continuation of this effort, in the current work, we focus on the NO_x storage on the BaO/θ-Al_2O_3/NiAl(100) model catalyst surface upon NO_2 adsorption using temperature programmed desorption (TPD) and x-ray photoelectron spectroscopy (XPS) techniques. Furthermore, NO_2 uptake of the BaO/θ-Al_2O_3/NiAl(100) model catalyst surface as well as the Ba-free θ-Al_2O_3/NiAl(100) substrate will be discussed in a comparative fashion. Finally, various factors influencing the thermal aging and the deactivation of the NSR systems will be examined. This will be illustrated by NO_2 adsorption and subsequent TPD analysis on a BaO/θ-Al_2O_3/NiAl(100) model catalyst surface that is pretreated at high temperatures (1100 K) prior to NO_x adsorption, in an attempt to simulate some of the long-term thermal aging effects that can occur under regular operational temperatures (573 to 673 K).

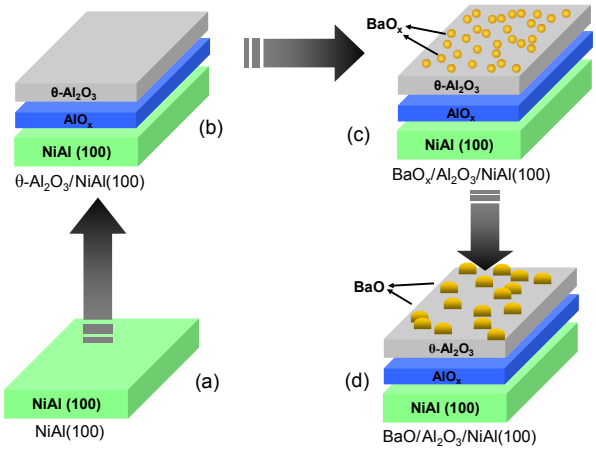

Figure 1. Model catalyst synthesis protocol.

Results and Conclusion

NO_x storage behavior of a BaO/θ-Al_2O_3/NiAl(100) model catalytic system during NO_2 adsorption was studied via XPS and TPD techniques and compared to that of the θ-Al_2O_3/NiAl(100) support material and a thermally aged BaO/θ-Al_2O_3/NiAl(100) model catalyst at 1100 K. At temperatures greater than 300 K, adsorbed NO_2 is converted to nitrates on all of the surfaces studied. Nitrates residing on the alumina sites of the model catalyst surfaces are relatively weakly bound and typically desorb within with the 300-to-600-K temperature range (Figure 2), leading to NO(g) evolution. Nitrates associated with the BaO sites are significantly more stable and desorb within the 600-to-850-K temperature range, resulting in NO(g) or NO(g)+O_2(g) evolution. NO_x uptake by the BaO sites of the BaO/θ-Al_2O_3/NiAl(100) model catalyst surface was found to be as high as a factor of five with respect to that of the θ-Al_2O_3/NiAl(100) support material. Thermal aging

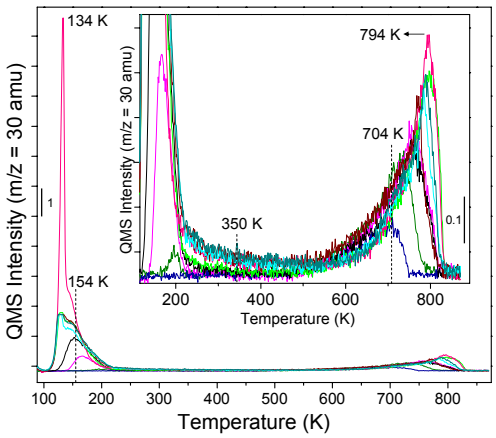

Figure 2. TPD spectra for NO_2 adsorption on BaO/θ-Al_2O_3/NiAl(100) model catalyst.

of a BaO/θ-Al_2O_3/NiAl(100) model catalyst surface at 1100 K prior to NO_x uptake experiments, brings about a significant (>70 percent) reduction in the NO_x storage capacity of the model catalyst surface.

Citations

Epling WS, LE Campbell, A Yezerets, NW Currier, and JE Parks II. 2004. "Overview of the Fundamental Reactions and Degradation Mechanisms of NOx Storage/Reduction Catalysts." *Catalysis Reviews* 46(2):163-245.

Ozensoy E, J Szanyi, and CHF Peden. 2005a. "Interaction of Water with Ordered θ-Al_2O_3 Ultrathin Films Grown on NiAl(100)." *Journal of Physical Chemistry* B 109(8):3431-3436.

Ozensoy E, CHF Peden, and J Szanyi. 2005b. "NO_2 Adsorption on Ultrathin θ-Al_2O_3 Films: Formation of Nitrite and Nitrate Species." *Journal of Physical Chemistry B* 109(33):15977-15984.

Inherent Disorder in $A_2Ti_2O_7$ (A=Sm and Gd) and Its Role in Radiation-Induced Amorphization Determined by Near-Edge X-Ray Absorption Fine Structure

P Nachimuthu,[(a)] S Thevuthasan,[(b)] WJ Weber,[(b)] V Shutthanandan,[(b)] Y Zhang,[(b)] DK Shuh,[(c)] DW Lindle,[(a)] G Balakrishnan,[(d)] DM Paul,[(d)] EM Gullikson,[(c)] and RCC Perera[(c)]

(a) University of Nevada, Las Vegas, Nevada
(b) Pacific Northwest National Laboratory, Richland, Washington
(c) Lawrence Berkeley National Laboratory, Berkeley, California
(d) University of Warwick, Coventry, United Kingdom

The changes in spectral widths in near-edge x-ray absorption fine structure (NEXAFS) spectra from $A_2Ti_2O_7$ (A=Sm and Gd) provide evidence for the presence of inherent disorder in these pyrochlore-structured oxides. These inherent disorders in the pyrochlores prior to irradiation facilitate rearrangement and relaxation of ions/defects within the crystal structure during the ion-beam-induced phase transition from the pyrochlore to the fluorite structure.

The diverse chemistry of pyrochlore-structured oxide materials results in a remarkable variation of properties that have many important technological applications such as catalysis, luminescence, magnetism, conductivity, and host matrices for actinide wastes. Their use as ceramic waste forms for the immobilization of actinides, particularly plutonium, is receiving increasing attention since the recent discoveries of radiation-resistant compositions such as $Gd_2Zr_2O_7$ and $Er_2Zr_2O_7$. However, several pyrochlores undergo a radiation-induced transformation from crystalline to amorphous upon irradiation. This behavior provides a basis for understanding the mechanisms responsible for increased radiation tolerance in $Gd_2Zr_2O_7$ and $Er_2Zr_2O_7$.

The Ti 2p and O 1s NEXAFS spectra from $Sm_2Ti_2O_7$(100) and $Gd_2Ti_2O_7$(100) single crystals recorded prior to irradiation at normal incidence ($\theta=0^o$), where the electric field vector (E) of the x-rays is parallel to the a axis (E||a); grazing incidence ($\theta=82.5^o$), where E is nearly parallel to the c axis (E||c); and following Au^{2+}-ion beam irradiation, at normal incidence ($\theta=0^o$) are compared in Figure 1. The polarization-dependent NEXAFS spectra show no anisotropic distribution of Ti and O sites in $Sm_2Ti_2O_7$(100) and $Gd_2Ti_2O_7$(100). The energy separation between t_{2g} and e_g states is related to the crystal field strength, which is ~2.2 and ~2.3 eV for $Sm_2Ti_2O_7$ and $Gd_2Ti_2O_7$, respectively. The e_g states, which consist of d_{z^2} and $d_{x^2-y^2}$ orbitals, are directed towards ligand anions and are, therefore, more sensitive to deviations from Ti O_h symmetry. Consequently, the splitting of e_g states into d_{z^2} and $d_{x^2-y^2}$ indicates the degree of distortion from O_h symmetry, which is ~1.0 eV for both pyrochlores. These results suggest that Ti in $Sm_2Ti_2O_7$ and $Gd_2Ti_2O_7$ is tetravalent and occupies distorted O_h site symmetry. Thus, the distortion from pure O_h site symmetry for $Sm_2Ti_2O_7$ and $Gd_2Ti_2O_7$ is the same. However, the crystal field strength derived from the TiO_6 O_h is slightly less for $Sm_2Ti_2O_7$ compared to $Gd_2Ti_2O_7$. The size difference between Sm^{3+} and Gd^{3+} is therefore reflected in bonding characters between cations and anions in

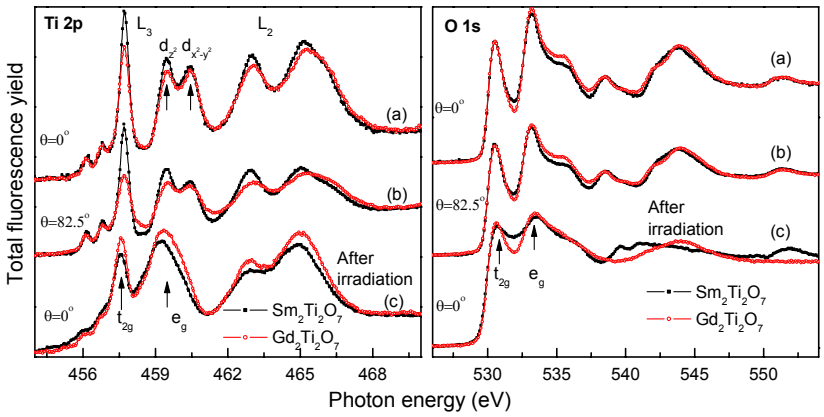

Figure 1. Ti 2p and O 1s NEXAFS spectra from $A_2Ti_2O_7$(100) (A=Sm or Gd). Spectra (a), (b), and (c) were recorded at normal (θ=0°, E||a), grazing (θ=82.5°, E||c) incidence prior to irradiation, and normal (θ=0°, E||a) incidence following Au^{2+}-ion beam irradiation, respectively.

these pyrochlores. This is also substantiated by the lattice parameter and the average bond distances between cations and anions. In general, the electronic transitions in NEXAFS occur from a selected atomic core level to unoccupied states and intensities of these transitions are related to the unoccupied density of states, which results from the electronic structures of given chemical compositions. The area analyses show that the increase in intensities for the transitions in Ti 2p NEXAFS prior to irradiation for $Sm_2Ti_2O_7$(100) compared to $Gd_2Ti_2O_7$(100) is ~13 % and ~52 % for E||a and E||c geometries, respectively. The intensity decrease in Ti 2p NEXAFS prior to irradiation for the E||c geometry compared to the E||a geometry is ~24 percent and ~43 percent for $Sm_2Ti_2O_7$(100) and $Gd_2Ti_2O_7$(100), respectively. The spectral intensity decrease for the E||c geometry compared to the E||a reflects a weaker covalence between Ti(d_{z^2}) and O(p_z) along the c axis with an elongated Ti-O distance in TiO_6 O_h of $Sm_2Ti_2O_7$ and $Gd_2Ti_2O_7$, providing evidence for a tetragonal distortion. Overall, the full width at half maximum of the transitions in Ti 2p NEXAFS spectra are slightly smaller for $Sm_2Ti_2O_7$(100) compared to $Gd_2Ti_2O_7$(100). These FWHMs also increase from E||a to E||c geometries. This is apparent in Figure 1 for the transitions from Ti $2p_{1/2}(L_2)$ to the e_g states. The variations in the spectral widths for the Ti 2p NEXAFS transitions suggest the presence of disorder in both $Sm_2Ti_2O_7$ and $Gd_2Ti_2O_7$. The degree of disorder is smaller for $Sm_2Ti_2O_7$ compared to $Gd_2Ti_2O_7$. This disorder increases from E||a to E||c geometry with a slightly smaller magnitude for $Sm_2Ti_2O_7$ compared to $Gd_2Ti_2O_7$.

A comparison of the Ti 2p NEXAFS spectra from the irradiated $Sm_2Ti_2O_7$(100) and $Gd_2Ti_2O_7$(100) shows a decrease in intensities for the transitions, suggesting less short-range order for $Sm_2Ti_2O_7$ compared to $Gd_2Ti_2O_7$ under identical irradiation conditions. Similar observations were also made in O 1s NEXAFS from $Sm_2Ti_2O_7$(100) and $Gd_2Ti_2O_7$(100) prior to and following ion-beam irradiation. These results enable us conclude that the inherent disorder in $Sm_2Ti_2O_7$ and $Gd_2Ti_2O_7$ facilitate the rearrangement and relaxation of Sm/Gd, Ti, and O ions/defects within the crystal structure during the ion-beam-induced phase transformation from the pyrochlore to the defect fluorite structure.

User Projects

Field-Emission Scanning Electron Microscopy (SEM) of Anode-Supported Yttria-Stabilized Zirconia Fuel Cells Poisoned by Chromium

Pacific Northwest National Laboratory, Richland, Washington
SP Simner
W.R. Wiley Environmental Molecular Sciences Laboratory, Richland, Washington
MH Engelhard

Surface and Interface Study of Contacts to Carbon-Based Films

Carnegie Mellon University, Pittsburgh, Pennsylvania
LM Porter, PB Kulkarni

Determination of the Catalytic Properties of Metal-Coated Nanowires

Washington State University, Pullman, Washington
AD Lalonde, MG Norton

Modification of Structure and Selectivity of Sensing Layers

Georgia Institute of Technology, Georgia Tech Research Corporation, Atlanta, Georgia
M Josowicz

Surface Characterization of Ambient Ultrafine Particles

Central Washington University, Ellensburg, Washington
EL Bullock, AM Johansen, C Thomas-Bradley

Stability of H Species in Various Dielectric Films Used in Advanced Microelectronic Fabrication

Texas Instruments Incorporated, Dallas, Texas
YR Kuan

Routine Scanning Electron Microscope (SEM) Analysis of Lysed Bacillus Spores

Pacific Northwest National Laboratory, Richland, Washington
CL Warner, CJ Bruckner-Lea, B Arey

Microscopy of Hanford Tank Sludge

Pacific Northwest National Laboratory, Richland, Washington
EC Buck

Electron Microscopy Investigation of Bacterial Outer Membrane Vesicles

Duke University, Durham, North Carolina
MJ Kuehn

Surface Area and Porosity Analyses of Mesoporous Thin Films and Powders

Pacific Northwest National Laboratory, Richland, Washington
RD Champion, S Li, AR Courtney

Scanning Electron Microscopy (SEM) Investigation of Thermal Barrier Coatings and Oxide Dispersion Strengthened Alloys
Pacific Northwest National Laboratory, Richland, Washington
GJ Grant, B Arey

Transmission Electron Microscopy (TEM) Study on Solid Oxide Fuel Cells Interconnects
Pacific Northwest National Laboratory, Richland, Washington
Z Yang

Deposition of Active Boron Carbide Thin Films by Plasma-Enhanced Chemical Vapor Deposition
Pacific Northwest National Laboratory, Richland, Washington
SN Kundu

An Experimental and Data-Analysis Investigation into the Trapped Gases and Non-Ice Material on the Surfaces of the Outer Planets
Planetary Science Institute, Pasadena, California
CA Hibbitts

Physical Characterization of Defects in ZnO-Diluted Magnetic Semiconductors
University of Washington, Seattle, Washington
KR Kittilstved, DR Gamelin

Investigation of Oxygen Diffusion in Single-Crystal Strontium Titanium Oxide (STO) Films Grown on Silica
Motorola, Tempe, Maryland
ZJ Yu

Characterization of Mesoporous SiO_2 Particles for the Characterization of Non-Ideal Sorption Behavior
Washington State University, Pullman, Washington
DR Yonge, DL Washington

Electrochemical Sensors and Biosensors for Environmental and Health Monitoring
Nanjing University, Nanjing, China
J Xu

Electrochemical Detection of Lead in Saliva
Pacific Northwest National Laboratory, Richland, Washington
W Yantasee

Molecular Beam Epitaxy Growth of Strontium Cobaltite
South Dakota School of Mines and Technology, Rapid City, South Dakota
AJ Anderson

Trace Metal Composition of Cobalt
Pacific Northwest National Laboratory, Richland, Washington
JB Cliff

A Combinatorial Sputtering Approach to Magnetic Properties: Modification of FeCoB
National Institute of Standards and Technology, Boulder, Colorado
RR Owings, DP Pappas

Controlling the Thermal and Non-Thermal Reactivity of Metal Oxide Structures Through Nanoscaling: Controlling Reactivity of Oxide Structures
Pacific Northwest National Laboratory, Richland, Washington
MA Henderson, KM Rosso, NI Iordanova, SA Chambers, M Dupuis, MS Gutowski, AG Joly, JE Jaffe, G Xiong, RN Shao
W.R. Wiley Environmental Molecular Sciences Laboratory, Richland, Washington
IV Lyubinetsky, KM Beck

X-Ray Photoelectron Diffraction of MgO(111)-(1x1)
Sandia National Laboratory, Milwaukee, Wisconsin
RA Plass
University of Wisconsin, Milwaukee, Milwaukee, Wisconsin
M Gajdardziska-Josifovska

Electrochemical and Transmission Electron Microscopy (TEM) Characterization of Metal Nanoparticles Deposited in Carbon Nanotubes
University of Idaho, Moscow, Idaho
CM Wai

Chemical Characterization of Sub-Micrometer Mineral Phases in Extraterrestrial Materials Previously Characterized by Nano-Secondary Ion Mass Spectroscopy (SIMS) Isotope Imaging
Washington University in St. Louis, St. Louis, Missouri
FJ Stadermann, CN Floss

Chemically Selective Sensor Film Characterization
University of Cincinnati, Cincinnati, Ohio
C Seliskar, W Heineman, N Pantelic

Advanced Electrode Concepts for CdZnTe Radiation Detectors
Pacific Northwest National Laboratory, Richland, Washington
CE Lehner, G Dunham

Energetic Ion Studies of Key Future Technological Materials
University of Jyvaskyla, Jyvaskyla, Finland
MI Laitinen, HJ Whitlow, V Touboltsev

Investigation of the Surface Characteristics of Chemically Modified Natural Fibers
Pacific Northwest National Laboratory, Richland, Washington
LS Fifield, JD Holbery

Characterization of Chalcopyrite Nanoparticles
University of Idaho, Moscow, Idaho
PJ Shapiro, JJ Nairn, N Kowliki

X-Ray Powder Diffraction Study of Fe_2O_3-Mn_2O_3 Phase Diagram
Pacific Northwest National Laboratory, Richland, Washington
JV Crum

Mesopore Uniformity and Hydrothermal Stability of Silica Thin Films for High-Permeabilty Applications
Pacific Northwest National Laboratory, Richland, Washington
RE Williford

Ceria Nanoparticles
University of Central Florida, Orlando, Florida
S Kuchibhatla, S Seal, D Bera
Pacific Northwest National Laboratory, Richland, Washington
DR Baer, KH Pecher

Nanoporous TiO_2 Ceramics
Washington State University, Pullman, Washington
A Bandyopadhyay

Novel Micro-Manipulation Methods for Radioactive Particle Isolation and Characterization with Energy-Filtered Electron Microscopy
Pacific Northwest National Laboratory, Richland, Washington
EC Buck, A Dohnalkova, BK McNamara

Scanning Electron Microscopy/Energy-Dispersive Spectroscopy (SEM/EDS) of Solid Oxide Fuel-Cell Seal Materials
Pacific Northwest National Laboratory, Richland, Washington
JS Vetrano, B Arey

Thermogravimetric Analysis of Organometallic Compounds and Semiconductor/Metal Nanoparticles
Pacific Northwest National Laboratory, Richland, Washington
MG Warner

X-Ray Photoelectron Spectroscopy (XPS) Studies of Self-Assembling Monolayers
Pacific Northwest National Laboratory, Richland, Washington
BJ Tarasevich

Understanding the Properties of Oxide and Metal Nanostructures
University of Jaffna, Jaffna, Sri Lanka
S Sivarajah, K Ahilan

Electroactive Materials for Anion Separation: Technetium from Nitrate
Pacific Northwest National Laboratory, Richland, Washington
TL Hubler, SD Rassat

Spectroelectrochemical Sensor for Technetium Applicable to the Vadose Zone
Pacific Northwest National Laboratory, Richland, Washington
AS Del Negro, TL Hubler, SA Bryan, Z Wang

Surface Migration of Additives in Polymers
Cornell University, Ithaca, New York
LA Archer, VS Minnikanti

Characterization of Functional Nanoscale Materials for Vapor Sensing
Pacific Northwest National Laboratory, Richland, Washington
CL Aardahl, RS Addleman, LS Fifield, F Zheng, DL Baldwin, O Reid, B Arey
Shasta College, Redding, California
SP Garland

Oxidation State of Technetium Electrodeposited on Platinum
Pacific Northwest National Laboratory, Richland, Washington
MD Engelmann

Antireflection Coatings
Pacific Northwest National Laboratory, Richland, Washington
WD Bennett, DC Stewart, CC Bonham, D Matson

Characterization of Oxide Nanoparticles
Pacific Northwest National Laboratory, Richland, Washington
L Wang

X-Ray Photoelectron Spectroscopy (XPS) Study of CeO_2 and $CeZrO_2$
Pacific Northwest National Laboratory, Richland, Washington
L Wang, S Azad

Novel Biosensor Based on Nanomaterials
Pacific Northwest National Laboratory, Richland, Washington
G Liu, Yn Lin, B Arey

Surface Analysis of Functional Carbons
Pacific Northwest National Laboratory, Richland, Washington
Y Shin

Ion-Beam Synthesis of Materials for Hydrogen Storage
Pacific Northwest National Laboratory, Richland, Washington
W Jiang

***In Situ* Fourier Transform Infrared (FTIR) Studies of Alumina in a Hydrogen Environment: A Study of Hydrogen Chemistry Within Ceramics**
Pacific Northwest National Laboratory, Richland, Washington
AC Stowe, RN Jones, C Henager, J Szanyi

Steam Reforming of Biomass
Pacific Northwest National Laboratory, Richland, Washington
H Roh

Homogeneous Precipitation of Cerium Dioxide Nanoparticles
Oregon State University, Corvallis, Oregon
C Tseng
Pacific Northwest National Laboratory, Richland, Washington
EC Buck

Nanocrystalline MoS_2 Catalysts
Pacific Northwest National Laboratory, Richland, Washington
WJ Shaw, JA Franz

Determination of Nanoporous Material Oxidation States
Pacific Northwest National Laboratory, Richland, Washington
DM Wellman, AJ Karkamkar, Z Hontz

Characterization of Pure and Doped ZnO Nanoclusters
University of Idaho, Moscow, Idaho
J Antony, Y Qiang

Study of Some Specific Inclusions in a Garnet Matrix Using High-Resolution Transmission Electron Microscopy
Washington State University, Pullman, Washington
MJ Guinel, MG Norton

Time-of-Flight-Secondary Ion Trap Microscopy (TOF-SIMS) and Auger Studies of Ozone Oxidation of Unsaturated Self-Assembled Monolayers on Silicon Surfaces
University of California, Irvine, Irvine, California
BJ Finlayson-Pitts, TM McIntire

Preparation, Characterization, and Application of Chemically Modified Electrodes
Pacific Northwest National Laboratory, Richland, Washington
X Cui

X-Ray Photoelectron Spectroscopy (XPS) Analysis of Fabric Chars to Determine the Phosphorous-Nitrogen Synergism in Flame Retardants
University of California, Davis, Davis, California
S Gaan, S Gang

Image Iron Oxide Nanoparticles
W.R. Wiley Environmental Molecular Sciences Laboratory, Richland, Washington
GR Holtom

Stabilization of Polar Oxide Interfaces: Integrated Experimental and Theoretical Studies of Atomic Structure and Electronic Properties
University of Wisconsin, Milwaukee, Milwaukee, Wisconsin
M Gajdardziska-Josifovska, S Cheung

Ion Beam Characterization of Nanocomposite Tribological Coatings
Montana State University, Bozeman, Montana
RJ Smith, PE Gannon

Surface Texture of Zircon Grains from the Sierra Madera Impact Structure in West Texas
Washington State University, Pullman, Washington
SA Huson, MC Pope

Model Hematite Thin Films and Bacterial Iron Reduction
Pacific Northwest National Laboratory, Richland, Washington
TC Droubay, ZN Wang, L Shi, BH Lower

Characterization of Manganese Cobalt Oxides Using X-Ray Photoelectron Spectroscopy (XPS)
Pacific Northwest National Laboratory, Richland, Washington
G Xia

Molecularly Organized Nanostructural Materials
Pacific Northwest National Laboratory, Richland, Washington
Y Shin, G Exarhos, CF Windisch

Measurements of Aerosol Composition by Aircraft During the 2005 Marine Stratus Experiment
Brookhaven National Laboratory, Upton, New York
PH Daum

Nuclear Reaction Analysis of Biotite Minerals
University of Michigan, Ann Arbor, Michigan
CV Ramana, E Essene

Determination of the Cause of Bloating in Titanium Pellets
Pacific Northwest National Laboratory, Richland, Washington
NL Canfield

Metal Nanoparticles
University of Idaho, Moscow, Idaho
JM Shreeve

Preparation of ZnO Thin Films by Metal Organic Chemical Vapor Deposition
University of Washington, Seattle, Washington
KR Kittilstved, DR Gamelin

Investigation of Structural Properties of Oxide and Nitride Nanowires
Lawrence Berkeley National Laboratory, Berkeley, California
MC Johnson

Characterization of GaN/InGaN/GaN Thin-Film Structures
University of Washington, Seattle, Washington
FS Ohuchi, E Venkatasubramanian, K Poochinda

Compositionally Graded Cobalt- and Chromium-Doped TiO_2 Rutile for Optimum Thermoelectric Power
Pacific Northwest National Laboratory, Richland, Washington
L Saraf
W.R. Wiley Environmental Molecular Sciences Laboratory, Richland, Washington
V Shutthanandan
National Institute of Advanced Industrial Science and Technology, Ibaraki, Japan
A Yamamoto
University of Washington, Seattle, Washington
FS Ohuchi, S Iwanaga

Electron Microscopy of Single-Walled Carbon Nanotubes During Growth on CoMo Bimetallic Catalysts
University of Oklahoma, Norman, Oklahoma
N Sakulchaicharoen, DE Resasco

Aerosol Sampling
Los Alamos National Laboratory, Los Alamos, New Mexico
PC Gray

Catalytic Ammonia Oxidation
Pacific Northwest National Laboratory, Richland, Washington
GE Fryxell

Structural Analysis of Kinetically Stabilized Core-Shell Nanoparticles
University of Maryland, College Park, Maryland
B Eichhorn

Analysis of Nanoparticulates
Pacific Northwest National Laboratory, Richland, Washington
EW Hoppe

Scanning Electron Microscopy (SEM) Analysis of Rotating Drum Impactor Filter Strips for Biological Species
W.R. Wiley Environmental Molecular Sciences Laboratory, Richland, Washington
ML Alexander

Adhesion of Polymer Sphere to Modified Natural Fiber Via Atomic Force Microscopy (AFM)
Pacific Northwest National Laboratory, Richland, Washington
JD Holbery

Collaborative Water Initiative Project on Stabilization of Water Treatment Residuals
University of Arizona, Tucson, Arizona
SV Burnside, JK Shaw, WP Ela

Systematic Study of Novel Nanomagnetic Materials
Alfred University, Alfred, New York
D Li, Y Liu, X Wang
Biophan Technologies, Inc., West Henrietta, New York
J Helfer

Functionally Graded Brake Materials
Pacific Northwest National Laboratory, Richland, Washington
EV Stephens

Determination P-Dopant Concentration in a Wide-Band-Gap SnO_2 Semiconductor Using a Rutherford Backscattering Technique
Portland State University, Portland, Oregon
SB Rananavare, A Chaparadza

Fabrication of Microconduits
Pacific Northwest National Laboratory, Richland, Washington
G Dunham

Low-Temperature Silicon Device Fabrication
Pacific Northwest National Laboratory, Richland, Washington
B Arey
University of Washington, Seattle, Washington
C Shih, ST Dunham, H Guo

Interdiffusion Studies in a Iron-Uranium Binary System in Inert and Hydrogen Atmospheres
University of Nevada, Reno, Reno, Nevada
D Chandra

Characterizing Size, Morphology, and Mechanical Properties of Superalloy Carbides
Washington State University, Pullman, Washington
J Hutchinson, KO Findley, JD Yeager

Analysis of the Composition of Copper Films
Washington State University, Pullman, Washington
R Johnson, DP Field

Design and Synthesis of Tailored Band-Gap SiGe(C) Detectors
Pacific Northwest National Laboratory, Richland, Washington
C Henager

Depth Profiles of Isotopic Oxygen in Cerium Oxide Catalysts
National Energy Technology Laboratory, Morgantown, West Virginia
DA Berry

Surface Characterization of Granular Iron from Cores of an *In Situ* Permeable Reactive Barrier
Oregon Health Sciences University/Oregon Graduate Institute, Beaverton, Oregon
PG Tratnyek

Proton-Induced X-Ray Emission (PIXE) Elements Analysis of Carbon Nanosheets
College of William and Mary, Williamsburg, Virginia
M Zhu, BC Holloway

Norovirus Transmission Electron Microscopy (TEM) Proposal
Tulane University, New Orleans, Louisiana
C Nickerson, K Honer, Z Bentrup
Pacific Northwest National Laboratory, Richland, Washington
TM Straub, B Arey
University of Arizona, Tucson, Arizona
CP Gerba
Arizona State University, Tempe, Arizona
B Mayer

Rhenium and Technetium Uptake by Iron-Based Materials
Pacific Northwest National Laboratory, Richland, Washington
KM Krupka, B Arey

Profilometry Studies of Printed Electrode Films for Fuel-Cell Applications
Pacific Northwest National Laboratory, Richland, Washington
CF Windisch

Cost-Effective, Ultrathin, Palladium-Based Membrane for Hydrogen Separation and Purification
Innovatek, Inc., Richland, Washington
Y Peng

High-Resolution Transmission Electron Microscopy (TEM) Images and Electron Diffractions for Gold Nanotubes/Nanorods and Metal Vanadate Nanotubes/Nanorods
University of Washington, Seattle, Washington
Y Wang, G Cao

Nickel Coating of Polmer Microbeads
Pacific Northwest National Laboratory, Richland, Washington
RM Ozanich

Electron Microscopy Imaging of *Cyanobacteria synechcystis*
Pacific Northwest National Laboratory, Richland, Washington
A Dohnalkova, B Arey

Development of Advanced Durable Lean NOx Catalysts for Diesel Engines After Treatment
Caterpillar, Inc., Alabama
PW Park, K Koshkarian

Characterization of Tungsten Carbide Synthesized by Controlled Template Method
Pacific Northwest National Laboratory, Richland, Washington
J Kwak, B Arey

Evaluation of Secondary Ion Mass Spectroscopy (SIMS) for Location of Bacterial Spores and to Source Growth Media and Geographic Location
Pacific Northwest National Laboratory, Richland, Washington
JB Cliff

X-Ray Diffraction (XRD) Analysis of Inorganic Chemicals
Colorado State University, Fort Collins, Colorado
AF Fuciarelli
Toxicology Northwest, Richland, Washington
LL Reed

Post-Growth Analysis of GaN and InGaN Grown with Metal Organic Chemical Vapor Deposition
University of Washington, Seattle, Washington
E Venkatasubramanian, K Poochinda, T Chen

Crystal Perfection in Cadmium Zinc Telluride Radiation Detectors
Pacific Northwest National Laboratory, Richland, Washington
MB Toloczko, M Bliss, ZN Wang

Materials for Automotive Sensor Development
Pacific Northwest National Laboratory, Richland, Washington
GW Coffey

Chemistry of Cadmium-Zinc Telluride Surfaces after Processing
eV Products, Saxonburg, Pennsylvania
AA Rouse, C Szeles

X-Ray Diffraction (XRD) Data Analysis and Consultation
Western Washington University, Bellingham, Washington
ME Bussell

Characterizations of Ni-Au Bimetallic Butane Steam-Reforming Catalyst
Pacific Northwest National Laboratory, Richland, Washington
Y Chin

Low-Angle X-Ray Characterization of Catalyst Porosity
Pacific Northwest National Laboratory, Richland, Washington
XS Li

The Characterization of the Solid-State Materials with Planar Carbon Cluster Unit
Washington State University Tri-Cities, Richland, Washington
H Zhang

Strengthening Mechanisms in Ultrahigh-Strength, Corrosion-Resistant Steel
Portland State University, Portland, Oregon
WE Wood, G Nightingale, G Mares, J Keegan

Determination of the Factors Controlling Colloid Generation from Altered Waste Forms: Transmission Electron Microscopy (TEM) Study of Colloid Interactions and Form Structure
Pacific Northwest National Laboratory, Richland, Washington
EC Buck

Microstructure Characterization of Platinum on Silicon
Pacific Northwest National Laboratory, Richland, Washington
BR Johnson

Stable Isotopes to Study Nutrient Cycling In Soils
Oregon State University, Corvalis, Oregon
DD Myrold, PJ Bottomley
Pacific Northwest National Laboratory, Richland, Washington
JB Cliff, CE Lehner

Evaluation of Multicomponent Porous Oxide Films
Pacific Northwest National Laboratory, Richland, Washington
XS Li

Characterization of Aluminosilicate Phases Forming Under Low-Silica Conditions
Pacific Northwest National Laboratory, Richland, Washington
S Mattigod

Spectroscopy and Microscopy of Doped TiO_2 Nanocrystalline Materials
University of Washington, Seattle, Washington
DR Gamelin, JD Bryan, P Radovanovic, NS Norberg, KM Whitaker

Fuel-Reforming Catalyst Characterization
Innovatek, Inc., Richland, Washington
PM Irving, Q Ming

Determination of Valance Band Offset in $Sr_2TiO_4/SrTiO_3$ Heterostructures
Pennsylvania State University, University Park, Pennsylvania
JH Haeni, DG Schlom

Investigation of Oxidation State of Elements in Natural Brannerites
Australian Nuclear Science and Technology Organization, Lucas Heights, Australia
MX Colella
Pacific Northwest National Laboratory, Richland, Washington
EC Buck

Fundamental Studies of Monolayer-Protected Nanoparticles by Gas Chromatography
Pacific Northwest National Laboratory, Richland, Washington
JW Grate
University of Washington, Seattle, Washington
RE Synovec, GM Gross

Epitaxial Growth and Properties of Nanoscale Oxides for Spintronics
University of Washington, Seattle, Washington
D Schmidt, FS Ohuchi, M Olmstead

Nondestructive Carbon Nanotube Modification of Tailored Functionality
Pacific Northwest National Laboratory, Richland, Washington
LS Fifield, CL Aardahl

Dilute Magnetic Semiconducting Oxide Thin Films and Nanostructures
University of Washington, Seattle, Washington
K Krishnan, KA Griffin, X Ji

How Desert Varnish Forms
University of Wisconsin-Parkside, Kenosha, Wisconsin
V Kolb
University of Washington, Seattle, Washington
RS Perry, JT Staley, RS Sletten

MeV Ion Irradiation of Non-Ice Solar System Analogue Materials
Jet Propulsion Laboratory, Pasadena, California
PM Beauchamp
University of Washington, Seattle, Washington
TB McCord, GB Hansen
Planetary Science Institute, Pasadena, California
CA Hibbitts

Characterization of Nanocomposites Using Electrochemistry, X-Ray Photoelectron Spectroscopy (XPS), Transmission Electron Microscopy (TEM), and Scanning Electron Microscopy (SEM)
University of California–San Diego, La Jolla, California
X Ye

Investigating Electrochemical Properties, Composition, and Oxidation States of Nanoparticles and Catalysts Using X-Ray Photoelectron Spectroscopy (XPS)
State University of New York at Binghamton, Binghamton, New York
C Zhong

Development of a Capability to Quantify Arsenic in an Adsorbent
University of Western Sydney, Penrith South DC, Australia
S Maheswaran, NN Yadav

Continued Investigation into the Spinel Nickel-Cobalt Oxide System
National Institute of Standards and Technology, Boulder, Colorado
RR Owings

Microstructural and Microchemical Analysis of Chalcogenide Nanowires
Pacific Northwest National Laboratory, Richland, Washington
BR Johnson

Reactivity of Primary Soil Minerals and Secondary Precipitates Beneath Leaking Hanford Waste Tanks
Pacific Northwest National Laboratory, Richland, Washington
W Um

Use of the W.R. Wiley Environmental Molecular Sciences Laboratory (EMSL) Scanning Microscopy Capabilities to Study Soil Mineral Weathering
Washington State University, Pullman, Washington
Z Balogh, J Dickinson, CK Keller, AL Espana

Scanning Electron Microscopy (SEM) of Life Stages of Gall Wasps of the Family *Cynipidae*
Humboldt State University, Arcata, California
JD DeMartini

Magnetic Nanoparticles Characterization
University of Washington, Seattle, Washington
Y Bao

Scanning Electron Microscopy (SEM) Image Acquisition: X-Ray Elemental Analysis
Pacific Northwest National Laboratory, Richland, Washington
RM Ozanich

Morphology of Colloids Formed in Soil Reacted with Simulated Hanford Waste Tank Solutions and the Distribution of Incorporated Adsorbed Cesium in the Colloids
Washington State University, Pullman, Washington
Y Deng, JB Harsh, M Flury

Reaction Specificity of Nanoparticles in Solution
University of Idaho, Moscow, Idaho
Y Qiang, J Antony
University of Minnesota, Minneapolis, Minnesota
RL Penn
Pacific Northwest National Laboratory, Richland, Washington
A El-Azab, DR Baer, KH Pecher, JE Amonette, EJ Bylaska, BD Kay, M Dupuis
Oregon Health Sciences University/Oregon Graduate Institute, Beaverton, Oregon
PG Tratnyek

Hematite Thin-Film Preparation for X-Ray Spectroscopic Studies of the Reactivity and Distribution of Pb(II) and As(V) at Natural or Matter/Iron Oxide Interfaces
Stanford University, Stanford, California
T Yoon, GE Brown

Assessment of Toxic Release Inventory Chemical Emission Factors from Munitions by Real-Time Mass Spectrometric Air Monitoring

Pacific Northwest National Laboratory, Richland, Washington
BT Jobson
W.R. Wiley Environmental Molecular Sciences Laboratory, Richland, Washington
ML Alexander
Battelle Columbus Operations, Columbus, Ohio
CW Spicer

Texture, Morphology, and Stress in Lead-Zirconium-Titanium Oxide Thin Films

Washington State University, Pullman, Washington
DF Bahr, AL Olson, MS Kennedy, JV Martinez, MC Robinson

Confirmation of Si-C Bonds in Grafted Monolayers through X-Ray Photoelectron Spectroscopy (XPS) Analysis

South Dakota School of Mines and Technology, Rapid City, South Dakota
CD Struckman

Experimental Measurements of the Band Offsets of Epitaxial Silicon on $LaAlO_3$ Single Crystals

Pacific Northwest National Laboratory, Richland, Washington
SA Chambers, JR Williams
Pennsylvania State University, University Park, Pennsylvania
LF Edge, DG Schlom, V Vaithyanathan

Structural Characterizations of Biogenic Germanium Oxide Nanospheres

Oregon State University, Corvallis, Oregon
C Chang, G Rorrer, S Liu

Determination of the Bonding of Various Surfactants onto ZrW_2O_8

South Dakota School of Mines and Technology, Rapid City, South Dakota
ED Swanson

Using Nickel-Ion Irradiation for the Development of Advanced Materials for the Next-Generation Nuclear Reactor

University of Wisconsin-Madison, Madison, Wisconsin
TR Allen
Argonne National Laboratory West, Idaho Falls, Idaho
J Gan

Characterization of Defects in Nd:YAG Using High-Resolution Transmission Electron Microscopy (TEM)

Washington State University, Pullman, Washington
DE Eakins, MG Norton

Hydrolytic Stability and Susceptibility of Transition Metal Diolate Complexes and Applications to Green Oxidation
Oregon State University, Corvallis, Oregon
KP Gable

Characterization of Manganese Oxidation State with Electron Energy Loss Spectroscopy
Pacific Northwest National Laboratory, Richland, Washington
EC Buck

Oxidation Studies of Coatings for Interconnect Plates in Solid Oxide Fuel Cells
Montana State University, Bozeman, Montana
RJ Smith, AN Kayani, PE Gannon
University of Michigan, Ann Arbor, Michigan
CV Ramana

Characterization and Method Development for Back-End-of-the-Line Wafer Processing Concepts
Pacific Northwest National Laboratory, Richland, Washington
AJ Carman, TS Zemanian, CR Yonker, JL Fulton, D Matson, BJ Tarasevich, RJ Orth, GE Fryxell, AH Zacher, B Arey
LAM Research Corporation, Fremont, California
DJ Hymes

Metallurgical Characterization of Coatings Deposited by Electrospark Deposition
Portland State University, Portland, Oregon
J Keegan, WE Wood, GA Tewksbury

Catalyst Development for Microreactors
Montana State University, Bozeman, Montana
PE Gannon
Pacific Northwest National Laboratory, Richland, Washington
DR Palo

Synthesis and Characterization of One-Dimensional Nanostructures
Washington State University Tri-Cities, Richland, Washington
H Zhang, L Wang

Solid-Phase Transformations in the Hanford Sediments Treated with Aluminum-Rich, Hyperalkaline, and Saline Solutions
Pacific Northwest National Laboratory, Richland, Washington
NP Qafoku

Environmental Scanning Electron Microscopic Analysis of Gas Hydrate and Hydrate-Bearing Sediments

Pacific Northwest National Laboratory, Richland, Washington
BP McGrail
W.R. Wiley Environmental Molecular Sciences Laboratory, Richland, Washington
JS Young

Scanning Electron Microscopy (SEM) on Electrode Surface/Electrode Preparation and Testing

Pacific Northwest National Laboratory, Richland, Washington
W Yantasee

Modified Carbon Supports for Aqueous Phase Catalysis: Applications for the Conversion of Glucose and Fermentation Products to Value-Added Chemicals

Pacific Northwest National Laboratory, Richland, Washington
GE Fryxell, JF White, JG Frye

Immobilized Enzymes for Bioremediation and Biosensing

Inha University, Incheon, South Korea
S Lee
University of Akron, Akron, Ohio
H Jia, Xn Zhao
Pacific Northwest National Laboratory, Richland, Washington
J Kim, JW Grate
University of Washington, Seattle, Washington
TE Herricks
Seoul National University, Seoul, South Korea
J Lee, C Lee, K Min, S Chung, H Na
Korean Advanced Institute of Science and Technology, Daejeon, South Korea
M Kim, J Youn
Pennsylvania State University, University Park, Pennsylvania
S Nair
Chungbuk National University, Chungbuk, South Korea
H Ahn, BS Kim
Gwangju Institute of Science and Technology, Gwangju, South Korea
B Kim
Dongguk University, Seoul, South Korea
S Jun

Measurements for Nano-Tip'ID

W.R. Wiley Environmental Molecular Sciences Laboratory, Richland, Washington
R Zhao

Characterization of Defects in Yttrium Orthovanadate

Washington State University, Pullman, Washington
JB LeBret, MG Norton, JP Winterstein, AD Lalonde

Scanning Probe Microscope Observation of Anatase TiO_2 Films
Kanagawa Academy of Science and Technology, Takatsu-ku, Kawasaki-shi, Japan
H Onishi

Scanning Electron Microscopy (SEM) and Secondary Ion Mass Spectroscopy (SIMS) Analysis of Organic Semiconductor Films Grown Using Liquid Crystal Solvents
Western Washington University, Bellingham, Washington
DL Patrick, FS Wilkinson

Characterization of Heat-Treated Silicon Carbide Specimens Using Scanning Electron Microscopy (SEM)
Washington State University, Pullman, Washington
MJ Guinel, MG Norton

X-Ray Photoelectron Spectroscopy (XPS) Characterization of the Passive Film/Corrosion Products Formed on Carbon Steel and a Nickel-Based Alloy in the Yucca Mountain Repository
University of Nevada, Reno, Reno, Nevada
V Arjunan, JH Lamb

Characterizing Metal Nanoparticle Nanoassemblies
Western Washington University, Bellingham, Washington
SR Emory, HR Pugsley

Novel Strucutres in Nanocrystalline Ceramic Materials
University of Colorado, Boulder, Colorado
G Zhan

High-Resolution Transmission Electron Microscopic Evidences of Stacking Faults in Zeolitic Minerals Formed in Hanford Sediments with Simulated Tank-Waste Solutions
Washington State University, Pullman, Washington
Y Deng

Microelectromagnets
Pacific Northwest National Laboratory, Richland, Washington
G Dunham

EM Analysis of Bacterial Co-Cultures
Pacific Northwest National Laboratory, Richland, Washington
FJ Brockman

Online Determination of Selected Vapor-Phase Hoffmann List Compounds by Proton Transfer Reaction Mass Spectrometry
Washington State University Tri-Cities, Richland, Washington
GM Anderson

DC-1 Molecular and Bio-Imprinting
Pacific Northwest National Laboratory, Richland, Washington
XS Li, B Arey

Silicon Carbide Nanowires and Nanospings: Processing, Self-Assembly, Characterization, and Properties
University of Idaho, Moscow, Idaho
D Zhang, DN McIlroy, AI Alkhateeb, J Wei, YA Kranov, H Mahood
Washington State University, Pullman, Washington
AD Lalonde

Mechanisms of Sulfur Poisoning of NOx Adsorber Materials
Pacific Northwest National Laboratory, Richland, Washington
Y Chin

Two-Dimensional Photonic Crystals Grown by Atomic Layer Deposition for Near-Infrared and Visible-Spectrum Optoelectronics Applications
University of Idaho, Moscow, Idaho
D Zhang, DN McIlroy, AI Alkhateeb, J Wei, YA Kranov, H Mahood
Washington State University, Pullman, Washington
AD Lalonde

Determining Particle Morphology in Ultrasound-Assisted Heterogeneous Catalysis
Pacific Northwest National Laboratory, Richland, Washington
RS Disselkamp

Ion-Solid Interactions in Ceramics
Pacific Northwest National Laboratory, Richland, Washington
WJ Weber, W Jiang
University of Michigan, Ann Arbor, Michigan
L Wang
Lawrence Berkeley National Laboratory, Berkeley, California
DK Shuh, P Nachimuthu

Materials and Methods for Multivariate Chemical Vapor Sensing
University of Oregon, Eugene, Oregon
C Dutton
Pacific Northwest National Laboratory, Richland, Washington
JW Grate, DL Baldwin, NC Anheier

Monolayer-Protected Gold Nanoparticle Investigation and Characterization
Pacific Northwest National Laboratory, Richland, Washington
JW Grate, BP Dockendorff
Southern Oregon University, Ashland, Oregon
LA Hughes

Synthesis and Characterization of Novel Nanocrystalline Oxide Film Structures: Interface Controlled, Self-Assembled Oxide Quantum

Pacific Northwest National Laboratory, Richland, Washington
A El-Azab, CF Windisch, DR Baer, J Szanyi
University of Virginia, Charottesville, Virginia
JF Groves, Y Du, RK Catalano

Transmission Electron Microscopy (TEM) Study of Carbon Nanotube Reinforced Polymer-Derived Ceramic Composites

University of Central Florida, Orlando, Florida
L An, Y Wang

Steam Reforming of Methanol over Highly Active and Selective Pd/ZnO Catalyst

Pacific Northwest National Laboratory, Richland, Washington
RA Dagle

Low-Energy Sputtering Experiments Using Rutherford Backscattering Spectroscopy

NASA Glenn Research Center, Cleveland, Ohio
MR Nakles, MT Domonkos

Proton Transfer Reaction: Mass Spectrometry Characterization of Carbon Nanotube Preconcentrators for Trace Chemical Signature Detection

Pacific Northwest National Laboratory, Richland, Washington
F Zheng

Characterization of Noble Metal Catalysts for Hydrogen Production and Purification in Fuel Cell Applications

University of South Carolina, Columbia, South Carolina
S Chin, MD Amiridis

Characterization of Polymer Thin Films and Arrays

Portland State University, Portland, Oregon
M Yan, J Ren, R Joshi, MB Harnish
Oregon Health Sciences University/Oregon Graduate Institute, Beaverton, Oregon
Y Chen

Field-Effect Studies of CoxTi1-xO_2 Thin Films

Yale University, New Haven, Connecticut
AS Posadas, J Yau, C Ahn

Continuous Iso-Sorbide Production

Pacific Northwest National Laboratory, Richland, Washington
JE Holladay

New Technologies for Reduction of Automobile Exhaust Emissions
Pacific Northwest National Laboratory, Richland, Washington
CH Peden, H Zhao

Elemental Analysis of Bulk Aerosol Samples Collected with Drum Impactor During the Mexico City Metropolitan Area 2003 Field Study
Pacific Northwest National Laboratory, Richland, Washington
RS Disselkamp
Massachusetts Institute of Technology, Cambridge, Massachusetts
MJ Molina, BM Zuberi, KS Johnson
W.R. Wiley Environmental Molecular Sciences Laboratory, Richland, Washington
A Laskin

Bioavailability of Arsenic in Dislodgeable Residue from Pressure-Treated Wood
Battelle Columbus Operations, Columbus, Ohio
BM Sass

Photovoltaic Projects
Pacific Northwest National Laboratory, Richland, Washington
GE Fryxell

X-Ray Photoelectron Spectroscopy (XPS) Characterization of Diesel Soot Materials
Pacific Northwest National Laboratory, Richland, Washington
D Kim

Electrochemical and Atomic Force Microscopy/Scanning Tunneling Microscopy (AFM/STM) Study of TiO_2 (Anatase) Film on $SrTiO_3$ Substrate
J. Heyrovsky Institute of Physical Chemistry, Prague, Czech Republic
L Kavan

Characterization of Regenerable CO_2 Sorbents
Pacific Northwest National Laboratory, Richland, Washington
F Zheng

Chemical Processing of Terpene Emissions from Forests
Argonne National Laboratory, Argonne, Illinois
PV Doskey

Europium Uptake in Various Self-Assembled, Monolayer-Coated Mesoporous Silica
Pacific Northwest National Laboratory, Richland, Washington
RS Addleman, ED Bott
U.S. Military Academy, West Point, New York
JT Bays

Transmission Electron Microscopy (TEM) and X-Ray Photoelectron Spectroscopy (XPS) Analysis of Ligand-Functionalized Semiconductor Quantum Dots Used in Biodetection Studies
Pacific Northwest National Laboratory, Richland, Washington
MG Warner, CJ Bruckner-Lea

Phenotypic Characterization of Trichloroethene (TCE) and Perchloroethylene (PCE) Degrading *Dehalococcoides*
Oregon State University, Corvallis, Oregon
MR Fisk, AR Sabalowsky, LC Semprini, LB Parker, NW Chambers

Hygrogen Adsorption/Release Study of Selected Chemical Hydrides
Pacific Northwest National Laboratory, Richland, Washington
L Li

Investigation of Strain in InGaN Multiquantum Well Structures
Lawrence Berkeley National Laboratory, Berkeley, California
MC Johnson

Transmission Electron Microscopy (TEM) and Scanning Electron Microscopy (SEM) Investigation of Non-Pathogenic Bacterial Cultures
Pacific Northwest National Laboratory, Richland, Washington
A Dohnalkova

Oxidation of Lead Sulfide Surfaces in the Presence of Phosphate: Nanoparticle Formation
University of California, Davis, Davis, California
AG Stack, WH Casey

Observations of *Scytonema*-Colonized and Non-Colonized Fiber Cement Roofing Shingles
Lab/Cor, Inc., Seattle, Washington
RM Fisher, BA Reine

Magnetic and Transport Studies of Coblt-Doped TiO_2 Thin Films
Boise State University, Boise, Idaho
A Punnoose

Composition Characterization of ZnO:Cr and ZnO:Co
University of Washington, Seattle, Washington
BK Roberts, K Krishnan

Molecular Beam Epitaxy (MBE) Growth of Epitaxial Anatase TiO_2(001) on STO(001) on Si(001) and Characterization of TiO_2 films
University of Washington, Seattle, Washington
KA Griffin, K Krishnan

Fabrication and Characterization of Functional Nanostructured Materials
University of California–San Diego, La Jolla, California
S Jin, X Ye

Fabrication and Characterization of Carbon Nanotube-Based Composites
University of California–San Diego, La Jolla, California
S Jin, X Ye

Synthesis and Characterization at Atomic Level of Novel Nanocrystalline Metal Oxide Structures
Nanjing Normal University, Nanjing, China
Z Yu

Surface Analysis of Metal Carbides
Pacific Northwest National Laboratory, Richland, Washington
Y Shin

Analysis of Catalysts and Microchannel Components
Pacific Northwest National Laboratory, Richland, Washington
VS Stenkamp, KP Brooks, DL King, W Tegrotenhuis, CM Fischer

Scanning Tunneling Microscopy (STM) Tip Analysis by Transmission Electron Microscopy (TEM)
Pacific Northwest National Laboratory, Richland, Washington
Z Dohnalek

Template-Based Growth of V_2O_5 Nanorods by Electrodeposition and/or Sol Electrophoresis
University of Washington, Seattle, Washington
SJ Limmer, G Cao

Micro-Dimension Calibration
XL Science and Technology, Richland, Washington
YB Peng

Sulfur Absorbents for Emission Control
Pacific Northwest National Laboratory, Richland, Washington
L Li

X-Ray Diffraction (XRD) Analysis of Mineral Samples
Columbia Gem and Jewelry, Kennewick, Washington
VC Rundhaug

Synthesis of Au Nanoclusters
Washington State University Tri-Cities, Richland, Washington
H Zhang, L Wang

Development of a Soldier-Portable Power System
Pacific Northwest National Laboratory, Richland, Washington
DR Palo

Characterization of Surface and Materials
Pacific Northwest National Laboratory, Richland, Washington
C Lei

Scanning Electron Microscopy (SEM) Characterization of Proposed Hydrogen Storage Materials
Pacific Northwest National Laboratory, Richland, Washington
LE Thomas

X-Ray Photoelectron Spectroscopy (XPS) Analysis of Fuel-Cell Components
Pacific Northwest National Laboratory, Richland, Washington
LR Pederson, GW Coffey, O Marina

Investigation of Elemental Contamination in Solid Oxide Fuel Cell Materials
Pacific Northwest National Laboratory, Richland, Washington
VL Sprenkle

Investigation of the Stability of Secondary Precipitates Incorporated with Contaminants
Pacific Northwest National Laboratory, Richland, Washington
W Um

Analysis of Catalysts
Pacific Northwest National Laboratory, Richland, Washington
DC Elliott

Growth of Vanadium Oxides on Anatase TiO_2(001)
Yale University, New Haven, Connecticut
W Gao, EI Altman

Chalcogenide Surface Science
Pacific Northwest National Laboratory, Richland, Washington
BR Johnson
W.R. Wiley Environmental Molecular Sciences Laboratory, Richland, Washington
MH Engelhard

Hydrogenation of Pyrolysis Oils to Create Value-Added Chemicals
Pacific Northwest National Laboratory, Richland, Washington
TR Hart, DC Elliott

Characterization of Lithium Aluminate Powders
Pacific Northwest National Laboratory, Richland, Washington
BR Johnson, TR Hart

Deposition of Metal-Doped Oxides for Spintronic Applications

Pacific Northwest National Laboratory, Richland, Washington
SA Chambers, TC Droubay
W.R. Wiley Environmental Molecular Sciences Laboratory, Richland, Washington
DE McCready, S Thevuthasan, V Shutthanandan, C Wang, AS Lea
University of Washington, Seattle, Washington
TC Kaspar

Study of Compositional Variations in Combinatorially Sputtered Transparent Conductive Oxides

Pacific Northwest National Laboratory, Richland, Washington
PE Burrows, D Matson

Probing Cation Disordering in $Gd_2Ti_2O_7$ Pyrochlore by X-Ray Photoelectron Spectroscopy (XPS)

University of Michigan, Ann Arbor, Michigan
RC Ewing, J Lian

Routine Manipulation of Transition Metal Salts in an Inert-Atmosphere Glove Box

Pacific Northwest National Laboratory, Richland, Washington
MG Warner, CJ Bruckner-Lea

In Situ X-Ray Photoelectron Spectroscopy (XPS) Measurements of Reforming Catalysts

Pennsylvania State University, University Park, Pennsylvania
EN Fox, C Song
Research Triangle Institute, Research Triangle Park, North Carolina
V Subramani

Studies of Corrosion of Materials by Lead Alloys for Advanced Reactor and Nuclear Waste Amelioration Applications

University of Nevada, Las Vegas, Las Vegas, Nevada
AL Johnson, JW Farley, DJ Koury, DA Parsons, TT Ho, U Younas
Idaho National Laboratory, Idaho Falls, Idaho
EP Loewen

Influence of Gd and Sm Doping on Atomic and Ionic Transport Properties of Novel Nanostructured Ceria-Zirconia Multilayers

University of Central Florida, Orlando, Florida
Y Wang, S Kuchibhatla, S Seal
Pacific Northwest National Laboratory, Richland, Washington
L Saraf, A El-Azab, O Marina, D Matson, J Gilmore, M Dyer
W.R. Wiley Environmental Molecular Sciences Laboratory, Richland, Washington
T Thevuthasan, C Wang, V Shutthanandan
Lawrence Berkeley National Laboratory, Berkeley, California
P Nachimuthu
Nanjing University, Nanjing, China
Z Yu
U.S. Department of Homeland Security, Washington, DC
A Cinson

X-Ray and Transmission Electron Microscopy (TEM) Characterization of Magnetic Thin Films

University of Idaho, Moscow, Idaho
B Pesic

Catalyst Characterization

Pacific Northwest National Laboratory, Richland, Washington
RS Disselkamp

Catalyst and Support Characterization

Pacific Northwest National Laboratory, Richland, Washington
RS Disselkamp, B Arey, J Kwak, J Szanyi
W.R. Wiley Environmental Molecular Sciences Laboratory, Richland, Washington
C Wang

Early Transition Metal Oxides as Catalysts: Crossing Scales from Clusters to Single Crystals to Functioning Materials

Pacific Northwest National Laboratory, Richland, Washington
CHF Peden, Y Wang, Jn Hu, J Herrera

Formation of Silicides by Ion-Beam Synthesis

Lund Instutute of Technology, Lund University, Lund, Sweden
CT Jonsson
University of Jyv skyl, Jyv skyl , Finland
HJ Whitlow

Hydrogen Storage

Pacific Northwest National Laboratory, Richland, Washington
T Autrey
University of Washington, Seattle, Washington
AM Feaver

Fundamental Studies of Oxygen Storage Materials
Pacific Northwest National Laboratory, Richland, Washington
CHF Peden, J Szanyi, E Ozensoy

Fundamental Studies of NOx Adsorber Materials
Pacific Northwest National Laboratory, Richland, Washington
J Kwak, CH Peden, J Szanyi, D Kim, RG Tonkyn, X Wang

Nanotemplated Electrodeposition
University of Washington, Seattle, Washington
DB Allred, DT Schwartz

Temperature-Dependent Adsorption and Reaction of Vapor Molecules on Miniaturized Tin Oxide Sensors
Northwestern University, Evanston, Illinois
M Su, VP Dravid

Conductivity of Functionalized Carbon Nanotube Films
University of Alaska, Fairbanks, Fairbanks, Alaska
R Khairoutdinov

Irradiation-Induced, Three-Dimensional, Ordered Arrays of Nanostructure
University of Michigan, Ann Arbor, Michigan
L Wang, S Zhu, T Ding

Thermogravimetric Mass Spectroscopic Analysis During Annealing of HfO_2 Thin Films in Argon
University of Alabama, Tuscaloosa, Tuscaloosa, Alabama
TM Klein

Studies of the ZnO/$CuIn_{1-x}Ga_xSe_{2-y}S_y$ Junction by X-Ray Photoelectron Spectroscopy (XPS)
Pacific Northwest National Laboratory, Richland, Washington
SN Kundu

Characterization of Nanostructed Gas Sorbents by Temperature-Programmed Desorption/Fourier Transform Infrared (FTIR) Measurements
Pacific Northwest National Laboratory, Richland, Washington
F Zheng

Liquid Chromatography Separation Development
Pacific Northwest National Laboratory, Richland, Washington
Q Luo

Nanoengineered Electrochemical Sensors for Mixed Wastes
Pacific Northwest National Laboratory, Richland, Washington
Y Lin, Z Wang, W Yantasee, X Cui, J Wang, G Liu, JR Bontha

Development of Stable Bipolar Membranes
Pacific Northwest National Laboratory, Richland, Washington
JR Bontha

Studies of Detector Surfaces
Pacific Northwest National Laboratory, Richland, Washington
SA Lehn, CJ Barinaga

OptoMagnetic Flow Cell
Pacific Northwest National Laboratory, Richland, Washington
G Dunham, H Qiao, TY Colgan

Characterization of Sputter-Deposited, Cobalt-Doped TiO_2 Films
University of Washington, Seattle, Washington
KA Griffin, K Krishnan

Crystallization Behavior of Bulk Amorphous Alloy
Washington State University, Pullman, Washington
A Bandyopadhyay, S Bose

Kiln Phosphoric Acid
JDC, Inc, New Cumberland, West Virginia
JA Megy

Auger Electron Microscopy for Use in Classifying the Oxide Content in an Electrospark Deposition Coating of Zirconium
Portland State University, Portland, Oregon
GA Tewksbury, WE Wood

Structural Characterization of Nanoporous Thin Films
Pacific Northwest National Laboratory, Richland, Washington
Z Dohnalek

Passive Film Stability in Alloy 22
University of Central Florida, Orlando, Florida
S Seal, D Bera
Pacific Northwest National Laboratory, Richland, Washington
DR Baer, RH Jones, CF Windisch

Measurements of Aerosol and Aerosol Precursors During the Summer-2004 Northeast Aerosol Experiment
Brookhaven National Laboratory, Upton, New York
PH Daum

Microcharacterization of Engineered Mono-Sodium Titanate
Pacific Northwest National Laboratory, Richland, Washington
EC Buck

Structure of Combined Colloidal/Organic Fouling Layer on a Nanofiltration Membrane

Oregon State University, Corvallis, Oregon
Q Li

Acid Vapor Weathering of Mars Analog Surface Materials

University of Washington, Seattle, Washington
GB Hansen
Planetary Science Institute, Pasadena, California
CA Hibbitts

Characterization of Nanostructured Ceramics

Washington State University, Pullman, Washington
S Bose

X-Ray Photoelectron Spectroscopy (XPS) of Materials for Hydrogen Storage

Pacific Northwest National Laboratory, Richland, Washington
BJ Tarasevich

Synthesis of Cu_2O Under Protein Control

University of Washington, Seattle, Washington
H Dai, DT Schwartz

Deposition of Fuel Cell Materials

Pacific Northwest National Laboratory, Richland, Washington
VL Sprenkle, CA Coyle

Yttrium Phosphate/Gadolinum Phosphate Particles for Cancer Imaging and Treatment

Pacific Northwest National Laboratory, Richland, Washington
A Gutowska

Microstructural Investigations of Novel Magnetic Oxide Semiconductors

Boise State University, Boise, Idaho
A Punnoose, MN Kongara

Imaging Polystyrene Microparticles

Pacific Northwest National Laboratory, Richland, Washington
RM Ozanich

Catalysis Collaborative Access Team
Pacific Northwest National Laboratory, Richland, Washington
CHF Peden
Texas A&M University, College Station, Texas
M Chen, DW Goodman, P Han
University of Washington, Seattle, Washington
RJ Chimentao
University of Texas at Austin, Austin, Texas
JM White

Atmospheric Emissions Collaborative Access Team
Envair, Pasco, Washington
JM Hales

Controlled Defect Generation in Porous Silicon
Pacific Northwest National Laboratory, Richland, Washington
DR Baer
State University of New York at Buffalo, Geneseo, New York
FS Ou

ATM, the Organization for International Standardization (ISO), and Other Standard and Metrology Measurements for Surface Analysis
Pacific Northwest National Laboratory, Richland, Washington
DR Baer

Ion-Channeling Studies of Epitaxial Oxide Films and Gas-Solid Interfaces
Wayne State University, Detroit, Michigan
KR Padmanabhan

Soft Lithography for Optics
Pacific Northwest National Laboratory, Richland, Washington
Gn Dunham, JC Birnbaum, CR Batishko, JA Willett

Nanomaterial Toxicology
Pacific Northwest National Laboratory, Richland, Washington
DR Baer

Surface Area Measurements
Pacific Northwest National Laboratory, Richland, Washington
WJ Shaw

Aging of Lean NOx Traps
Oak Ridge National Laboratory, Knoxville, Tennessee
BG Bunting

Characterization of Cr(III) Solid Phases
Pacific Northwest National Laboratory, Richland, Washington
D Rai

Surface Cleanliness of Silicon Wafers After Laser Treatment
Washington State University, Pullman, Washington
L Scudiero

X-Ray Photoelectron Spectroscopy (XPS) Studies of Cobalt-Phthalocyanine Thin Films
Washington State University, Pullman, Washington
KW Hipps, WA English

Surface Characterization of Calcium Phosphates
Pacific Northwest National Laboratory, Richland, Washington
WJ Shaw

Scanning Electron Microscopy (SEM) of Protein-Assisted Calcium Phosphate Nucleation
Pacific Northwest National Laboratory, Richland, Washington
WJ Shaw

Origin of the Face-Dependent Photocatalytic Activity of TiO_2: Probing Surface Chemistry with Molecular Adsorption
Tulane University, New Orleans, Louisiana
U Diebold, TJ Beck, A Klust
Pacific Northwest National Laboratory, Richland, Washington
MA Henderson

Photochemical Studies of N-doped TiO_2 Single Crystals: Fundamental Investigations of Water-Splitting on Model TiO_2
Pacific Northwest National Laboratory, Richland, Washington
MA Henderson, SA Chambers, S Cheung, Rn Shao
W.R. Wiley Environmental Molecular Sciences Laboratory, Richland, Washington
IV Lyubinetsky, S Thevuthasan
University of Washington, Seattle, Washington
EK Vestergaard
University of Texas at Austin, Austin, Texas
MD Robbins, JM White

Size-Selected, Gas-Phase Soot Aerosol Oxidation
National Institute of Standards and Technology, Gaithersburg, Maryland
SH Kim
University of Maryland, Gaithersburg, Maryland
MR Zachariah

Scanning Electron Microscopy (SEM) Image of Microparticles
Pacific Northwest National Laboratory, Richland, Washington
RM Ozanich

X-Ray Photoelectron Spectroscopy (XPS) Analysis on Tungten Oxide Nanoclusters Supported on MCM41
Pacific Northwest National Laboratory, Richland, Washington
J Herrera

Chrome Volatility
Pacific Northwest National Laboratory, Richland, Washington
GD Maupin
W.R. Wiley Environmental Molecular Sciences Laboratory, Richland, Washington
TW Wietsma

Liquid Product Analysis by Gas Chromatography and Mass Spectrometry
Pacific Northwest National Laboratory, Richland, Washington
J Hu

Tungsten Analysis as a Surrogate for Uranium in Ash
Pacific Northwest National Laboratory, Richland, Washington
TR Hart, AJ Schmidt, MR Elmore

Inductively Coupled Plasma Analysis of Metal Ions
Pacific Northwest National Laboratory, Richland, Washington
W Yantasee

Structure and Property Tailoring of Metal Nanoparticles Dispersed in Dielectrics by High-Energy Ion Implantation
Pacific Northwest National Laboratory, Richland, Washington
L Ream, B Arey
North Carolina State University, Raleigh, North Carolina
G Duscher
W.R. Wiley Environmental Molecular Sciences Laboratory, Richland, Washington
CN Wang, V Shutthanandan, S Thevuthasan

New Materials as Sulfur Absorbents
Pacific Northwest National Laboratory, Richland, Washington
L Li

Surface Analysis of Indoor-Air-Quality Volatile Organic Carbon Sensors
AirAdvice, Inc., Portland, Oregon
M Kleefstra

Structure and Performance of DNA Biosensors
Pacific Northwest National Laboratory, Richland, Washington
CJ Bruckner-Lea, TM Straub
W.R. Wiley Environmental Molecular Sciences Laboratory, Richland, Washington
AS Lea

The Characterization of Aluminum Nitride-Silicon Carbide Alloy Crystals on Silicon Carbide Substrates
Kansas State University, Manhattan, Kansas
JH Edgar, Z Gu

Surface-State Characterization of Pt/Al_2O_3 Catalyst for the CPO Reaction
Kansas State University, Manhattan, Kansas
KL Hohn, C Cao

Gas Cell Metallization
Pacific Northwest National Laboratory, Richland, Washington
KC Antolick, JI McIntyre, GN Dunham

Interposer Profile Measurements
University of Alaska, Fairbanks, Fairbanks, Alaska
LE Bowman

Chemical Analysis of Nanostructures for Toxic Gas Detection
South Dakota State University, Brookings, South Dakota
DW Galipeau

Synthesis and Characterization of Enzyme Nanoparticles
Pacific Northwest National Laboratory, Richland, Washington
G Liu

Mesopore Uniformity and Hydrothermal Stability of Silica Thin Films for High-Permeability Applications
Pacific Northwest National Laboratory, Richland, Washington
S Li, A Qiao, B Arey

Determination of Pore Structure in Highly Porous SiO_2 Powders
Pacific Northwest National Laboratory, Richland, Washington
LS Fifield, RD Champion

Characterization of Corrosion Products on Iron Aluminide Coated Alloys
Pacific Northwest National Laboratory, Richland, Washington
DJ Senor

Salt Cake Waste Fractional Crystallization and Displacement Washing
Pacific Northwest National Laboratory, Richland, Washington
GB Josephson, JG Geeting

Surface Assessment of BxCy Thin Film on Silicon
Pacific Northwest National Laboratory, Richland, Washington
AJ Carman

Electroforming Copper
Pacific Northwest National Laboratory, Richland, Washington
G Dunham

X-Ray Photoelectron Spectroscopy (XPS) Investigations of Transition Metal-Doped Oxide Semiconductors
Boise State University, Boise, Idaho
J Hays, A Punnoose

Effects of Ice-Clearing Chemicals
Pacific Northwest National Laboratory, Richland, Washington
EV Stephens

Testing of Carbon-Based Materials for Hydrogen Storage
University of Washington, Seattle, Washington
AM Feaver, G Cao

Nanoclusters, Nanomaterials, and Nanotechnology (University of Washington/National Science Foundation)
Louisiana State University, Baton Rouge, Louisiana
A Krishna
Portland State University, Beaverton, Oregon
X Cui, J Lee, C Qi
South Dakota School of Mines and Technology, Rapid City, South Dakota
AJ Anderson, WM Cross, T Engstrom, W Douglas, J Reams, W Weyer
University of Idaho, Moscow, Idaho
J Antony, An Sharma
Washington State University, Pullman, Washington
MJ Guinel, AD Lalonde, L Wang, AN Rogan, SR John, E Brown, M Al-khedher, C Dutton, J Hardy, M Pirzada, E Rude, H Singh
Western Washington University, Bellingham, Washington
FS Wilkinson, C Murphy, R Norwood
University of Western Sydney, Nepean Australia, Kingswood, Australia
S Maheswaran
University of Montana, Missoula, Montana
JH Willet
Pacific Northwest National Laboratory, Richland, Washington
A El-Azab, DR Baer
Florida State University, Tallahassee, Florida
Q Liu
McGill University, Montreal, Quebec, Canada
AP Kouprine
South Dakota State University, Brookings, South Dakota

DW Galipeau
Carnegie Mellon University, Pittsburgh, Pennsylvania
PB Kulkarni
Pacific Lutheran University, Tacoma, Washington
ML Cotten, P Davis
University of Washington, Seattle, Washington
DB Allred, SL Tait, LT Ngo, A Tankut, CM Lee, NT Nguyen, JH Wei, MT Zin, JN Randall, R Ostermann, X Zheng, J Zou
Air Force Institute of Technology, Dayton, Ohio
G Seetharaman
Boise State University, Boise, Idaho
J Youngsman
Oregon Health Sciences University/Oregon Graduate Institute, Beaverton, Oregon
V Sarathy, S Sundara Rajan
University of Tulsa, Tulsa, Oklahoma
S Kothari
University of South Florida, Tampa, Florida
J Hickey
University of Alaska Fairbanks, Fairbanks, Alaska
G Cushing, SP Ingole, DP Kulkarni, GP Lee
North Dakota State College of Science, Wahpenton, North Dakota
M Burke, R Hendrickson

Staff

S. Thevuthasan, Staff Scientist, Technical Lead
(509) 376-1375, theva@pnl.gov

Bruce W. Arey, Technologist
(509)376-3363, bruce.arey@pnl.gov

Barbara L. Diehl, Administrator
(509) 376-1518, barb@pnl.gov

Alice Dohnalkova, Senior Research Scientist
(509)376-3908, alice.donalkova@pnl.gov

Mark H. Engelhard, Research Scientist
(509) 376-1664, mark.engelhard@pnl.gov

A. Scott Lea, Senior Research Scientist
(509) 376-9145, scott.lea@pnl.gov

Igor V. Lyubinetsky, Senior Research Scientist
(509) 376-5220, igor.lyubinetsky@pnl.gov

David E. McCready, Research Scientist
(509) 376-9648, david.mccready@pnl.gov

Laxmikant V. Saraf, Senior Research Scientist
(509) 376-2006, laxmikant.saraf@pnl.gov

V. Shutthanandan, Senior Research Scientist
(509) 376-2708, shuttha@pnl.gov

Chongmin Wang, Senior Research Scientist
(509) 376-4292, chongmin.wang@pnl.gov

Yanwen Zhang, Senior Research Scientist
(509)376-3429, yanwen.zhang@pnl.gov

We would also like to acknowledge the contributions from Gregory J. Exarhos, Charles H.F. Peden, Donald R. Baer, Jay W. Grate, Scott A. Chambers, William J. Weber, Michael A. Henderson, Janos Szanyi, Do Heui Kim, Michael L. Alexander, Timothy C. Droubay, Weilin Jiang, Mark E. Gross, Yong Wang, Yuehe Lin, Timothy L. Hubler, Todd R. Hart, Jungbae Kim, Jianli (John) Hu, Ja Hun Kwak and Robert S. Disselkamp.